

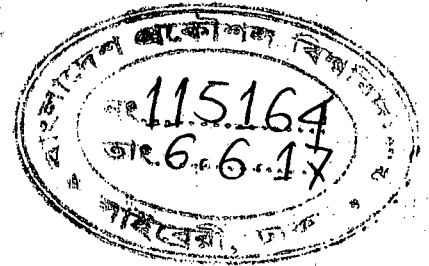
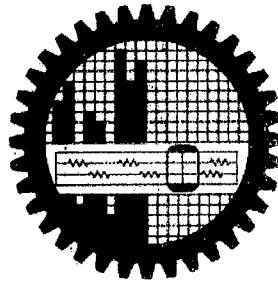
AERODYNAMIC CHARACTERISTICS OF A TRANSONIC AIRFOIL CASCADE

by

Sudarshan Chandra Saha

(0411102057)

Submitted in partial fulfillment of the requirements for the degree of Master of Science in
Mechanical Engineering



Under the supervision of

Dr. A.B.M. Toufique Hasan

Professor

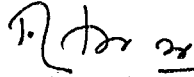
Department of Mechanical Engineering
Bangladesh University of Engineering and Technology (BUET)

BANGLADESH UNIVERSITY OF ENGINEERING AND TECHNOLOGY,
DHAKA-1000, BANGLADESH

December 2016

Certificate of Approval

The thesis titled, "Aerodynamic Characteristics of a Transonic Airfoil Cascade", submitted by Sudarshan Chandra Saha, Roll No: 0411102057, Session: April 2011, has been accepted as satisfactory in partial fulfillment of the degree of Master of Science in Mechanical Engineering on 28th December 2016.



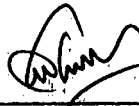
Dr. A.B.M. Toufique Hasan
Professor
Department of Mechanical Engineering
BUET, Dhaka

Chairman
(Supervisor)



Head
Department of Mechanical Engineering
BUET, Dhaka

Member
Ex-Officio



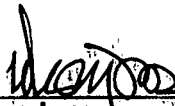
Dr. Mohammad Mamun
Professor
Department of Mechanical Engineering
BUET, Dhaka

Member



Dr. Mohammad Nasim Hasan
Associate Professor
Department of Mechanical Engineering
BUET, Dhaka

Member

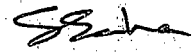


Dr. Dipak Kanti Das
Professor
Department of Mechanical Engineering
Military Institute of Science & Technology (MIST)
Mirpur, Dhaka.

Member
(External)

Candidate's Declaration

This is hereby declared that this thesis or any part of this thesis has not been submitted elsewhere for award of any degree or diploma.



Sudarshan Chandra Saha

Acknowledgements

First of all with limitless gratitude, I would like to thank Almighty God for providing me the strength and ability to complete this research.

It is a great pleasure to acknowledge my deepest thanks and gratitude to my honorable thesis supervisor, Dr. A. B.M. Toufique Hasan, Professor, Department of Mechanical Engineering, BUET, for his unwavering support, mentorship and continuous monitoring throughout this study. Without his thoughtful encouragement, careful supervision and excellent research facilities in laboratory, this thesis would never have taken shape. It is a great honor to work under his supervision.

There are many people whose direction, advice, support and contributions have proved invaluable along the way. I would like to thank all those people who are directly or indirectly involved with this thesis.

I extend my heartiest gratitude to Dr. Mohammad Ali, Head, Department of Mechanical Engineering, BUET as he has given the initial clearance to do this research work.

The present work has been carried out with computational resource support from Higher Education Quality Enhancement Project (HEQEP), AIF (3rd Round)-Sub-Project CP 3111, UGC, MoE, Government of Bangladesh. For this, I also offer my sincere gratitude to Government of Bangladesh.

Abstract

The trend towards higher pressure ratio and compact turbomachines with a reduced number of stages leads to a considerable increase of aerodynamic loading of the airfoil cascades. Thereby the velocities relative to the blades increase to transonic and supersonic speeds and shock-waves occur within the airfoil cascade. These shock waves could interact with the airfoil surface boundary layer and can cause unsteady boundary layer separation. In fact, Shock wave-boundary-layer interactions (SBLIs) occur when a shock wave and a boundary layer converge and since both can be found in almost every supersonic flow, these interactions are commonplace. The most obvious way for them to arise is for an externally generated shock wave to impinge onto a surface on which there is a boundary layer. In the transonic regime, shock waves are formed at the downstream edge of an embedded supersonic region; where these shocks come close to the surface, a SBLI is produced. In any SBLI, the shock imposes an intense adverse pressure gradient on the boundary layer, which causes it to thicken and possibly also to separate. SBLI also causes flow unsteadiness. Shock induced oscillations (SIO), aerodynamic instabilities, high cycle fatigue failure (HCF), non-synchronous vibration (NSV), aeroacoustic noise and so on are the detrimental consequences of this unsteady shock wave boundary layer interaction. On transonic wings, it increases the drag and has the potential to cause flow unsteadiness and buffet. In hypersonic flight, SBLI can be disastrous because at high Mach numbers, it has the potential to cause intense localized heating that can be severe enough to destroy a vehicle. Because of its significance for many practical applications, SBLI is the focus of numerous studies spanning several decades.

Many of the investigations have been dealt considering an isolated airfoil in transonic flows. However, little information is available on the aerodynamics of airfoil cascades. The goal of the present research is to analyze and to understand the transonic flow phenomena in a circular arc airfoil cascade using experiments and numerical computation. Experimental tests were conducted to investigate the behavior of passage shock waves with the shock induced boundary layer separation in a supersonic wind tunnel flow facility. Further, a Reynolds averaged Navier- Stokes (RANS) solver was used to provide airfoil surface pressures, overall performance from wake characteristics and so on. Particular attention is to be paid on the embedded shock wave structure and an accurate simulation of the shock boundary layer interaction. The experiment was performed for unstaggered case and the numerical studies were performed for stagger or setting angle 0° to 20° . The results show that the self-excited shock wave oscillations occur in the cascade passage for a pressure ratio of 0.75 in both unstaggered and staggered case. Fluctuating pressure histories are recorded at different locations in the flow field. PSD from FFT calculation of the data is used to find the principal frequency of the unsteady behaviour. A frequency of 976 Hz is found to be the dominating frequency. It is observed that for all the cases, the flow field remains undisturbed from leading edge to $x/c=0.50$, as in that portion no shock wave is observed on the airfoil surfaces. For different stagger angle, peak RMS of pressure oscillation (p_{rms}/q_0) is calculated and its location is identified. Flow separation occurs at a distance after the shock wave. Separation points and separation lengths are also calculated. Wave drags contribution is much higher than viscous drag at high speed compressible flow. Wave drag coefficients are also calculated for different flow conditions.

List of symbols

c	chord length of the airfoil, mm
M	Mach number
PR	pressure ratio
RMS	root mean square
T	time period of shock wave oscillation, s
t	instantaneous time, s
x	stream wise coordinate, mm
y	normal coordinate, mm
p	static pressure, Pa
X_s	shock location, mm
α	angle of attack, °
θ	stagger angle, °
ρ	density, kg/m ³
c_d	coefficient of drag
f	frequency, Hz
g	Gravitational acceleration, m/s ²
u	Velocity in x-direction, m/s
v	Velocity in y-direction, m/s
V	Velocity vector, m/s
μ	Dynamic viscosity, Ns/m ²
μ_t	Turbulent viscosity, Ns/m ²
τ	Shear stress, N/m ²
U	Conservative flux vector
F	Inviscid flux vector
Q	Energy flux vector (transfer of energy per unit cross-sectional area per unit time)
S	Surface area, m ²
K	Thermal conductivity, (W/m.K)
k	Reduced Frequency

Subscripts

∞	free stream condition
b	back condition
s	shock wave
i, j	coordinate index

Abbreviations

SIO	Shock Induced Oscillations
HCF	High Cycle Fatigue
NSV	Non-Synchronous Vibration
PSD	Power Spectral Density
FFT	Fast Fourier Transform
SBLIs	Shock Wave-Boundary-Layer Interactions
LE	Leading Edge
TE	Trailing Edge

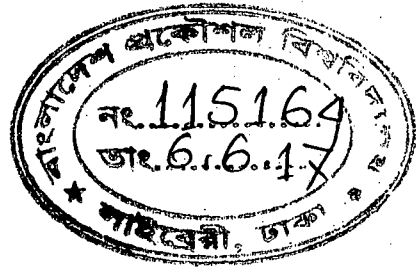
TABLE OF CONTENTS

ABSTRACT	(iv)
CHAPTER 1: INTRODUCTION	
1.1 Background	1
1.2 Shock wave	2
1.3 Flow field development in compressor cascade	3
1.4 Self-sustained shock wave oscillation mechanism	6
1.5 Types of shock oscillation	7
1.6 Cascade geometry	8
1.7 Objectives	9
CHAPTER 2: LITERATURE REVIEW	10
CHAPTER 3: COMPUTATIONAL METHOD	
3.1 Basics of CFD	25
3.2 Applications of CFD	25
3.3 Governing Equations	26
3.4 Strategy of CFD	27
3.5 Discretization Using Finite Volume Method	28
3.6 Solver Setting	30
3.6.1 Discretization Scheme	30
3.6.2 The Density Based Algorithm	31
3.7 Turbulence Modeling	32
3.7.1 $k-\omega$ two equations Turbulence Model	33
3.7.1.1 Standard $k-\omega$ Model	33
3.8 Turbulence Intensity	34
3.9 Operating Condition	34
3.10 Boundary Condition	35
3.11 Courant Number	36
3.11.1 Courant Numbers for The Density-Based Implicit Formulation	36
3.12 Material Selection	36
3.12.1 Sutherland's Law	37
3.13 Steady Analysis	37
3.14 Unsteady Analysis	37
3.15 Discretization Of The Domain	38
CHAPTER 4: COMPUTATIONAL RESULTS	
4.1 Validation of Numerical Model	39
4.2 Flow Field Contour Behavior	41
4.3 c_p Distribution	50
4.4 Unsteady Shock Position	55
4.5 Shock Strength	57
4.6 Unsteady Pressure Distribution	59
4.7 FFT	88

4.8	p_{rms}/q_0	100
4.9	Boundary Layer Separation Characteristics	102
4.10	Drag Characteristics	109
CHAPTER 5: EXPERIMENTAL STUDY		
5.1	Supersonic Wind Tunnel Facility	111
5.2	Flow Field Around Cascade	112
5.3	Schlieren Image (EXPERIMENTAL)	114
CHAPTER 6: SUMMARY AND RECOMMENDATION		
6.1	Summary of the Study	117
6.2	Recommendation	119
REFERENCES		120

CHAPTER 1

INTRODUCTION



1.1 BACKGROUND

Aerodynamic problems may be classified into two categories by the flow environment - external flow and internal flow. An external flow is a flow over the outside surface of an object. In case of external flow boundary layers develop freely, without constraints imposed by adjacent surfaces. Accordingly, there will always exist a region of the flow outside the boundary layer in which velocity, temperature gradients are negligible. Common examples are the flow over a flat plate, flow around curved surfaces such as a sphere, cylinder, airfoil, or turbine blade, air flowing around an airplane and water flowing around the submarines.

Internal flow is a kind of flow in which the fluid is confined by a surface. For many fluid devices of engineering importance, internal flow plays a vital role. Hence, the boundary layer is unable to develop without eventually being constrained. Examples include jet engines or other propulsion systems, fluid machinery such as compressors, turbines and pumps, duct flows, flow passing through nozzles, diffusers, and combustors. Laminar flow through a circular pipe is the simplest example of internal flow, whereas turbulent flow in and between the blade rows of turbines and compressors is probably the most complex form of internal flows. By their very nature, the stator and rotor blades are of complex shape- both curved and twisted, so their main flow field may be fully three dimensional. They are hard to analyze even without the added complexity of turbulence. Furthermore, turbomachines flow nature is periodically unsteady. This periodic unsteadiness is the essential mechanism for high efficiency energy exchange between a rotor and a continuously flowing fluid stream. Only in recent years the instruments and techniques have been developed so that turbulence may be properly studied in turbomachines flows. Internal flow exhibits a rich array of fluid dynamic behavior not encountered in external flow. Further, during the last few decades many research works have been completed on external flow and a little information is available about internal flow. For the good understanding of flow behavior between the blades of the turbomachines it is very important to study the internal flow.

Gas turbine engines are a major part of propulsion systems of different aircrafts. For high mass flow rate and high pressure ratio multi-stage axial-flow compressor is used in gas turbine engine. Since airfoils are employed in accelerating and diffusing the air in a compressor, much of the theory and research concerning the flow in axial compressors are based on studies of isolated airfoils. The nomenclature and methods of describing compressor blade shapes are almost identical to that of aircraft wings. Research in axial compressors involves the mutual effect of one blade on the other.

Thus, several blades are placed in a row to simulate a compressor rotor or stator. Such a row is called a cascade.

In modern high speed turbo-machineries and aeronautical applications such as transonic airfoil cascades, propulsion nozzles both subsonic and supersonic conditions are present. As a result, shock wave emerges in the flow field and flow separation occurs on the airfoil cascade surfaces. Interaction of the shock wave with the boundary layer makes the flow field unsteady and complex. The boundary layer is subjected to an intense adverse pressure gradient that is imposed by the shock which increases the thickness of the boundary layer. The shock must propagate through a multilayered viscous and inviscid flow structure. When the flow is not laminar, the production of turbulence is enhanced, which amplifies the viscous dissipation and leads to a substantial rise in the drag of cascade and increase the internal flow losses. The adverse pressure gradient distorts the boundary-layer velocity profile, causing it to become less full. This produces an increase in the displacement effect that influences the neighbouring inviscid flow. The interaction, experienced through a viscous-inviscid coupling, can greatly affect the flow past a transonic airfoil cascade. These consequences are exacerbated when the shock is strong enough to separate the boundary layer, which can lead to dramatic changes in the entire flow field structure. Shock-induced separation may trigger large-scale unsteadiness, leading to buffeting on wings, buzz for air-intakes, or unsteady side loads in nozzles. All of these conditions are likely to limit a machine's performance and, if they are strong enough, can cause structural damage. Since the underlying mechanism of this phenomenon is not fully revealed, understanding and controlling this shock boundary layer separation is necessary.

1.2 SHOCK WAVE

In transonic flow occurrence of shock wave is one of the prime concern. Shock wave is literally a thin layer having a drastic pressure difference in the two opposite sides. Shock wave generation is an isentropic process which incorporates a sudden rise in pressure at the downstream. When the Mach number approaches to a higher value, air is no longer considered as incompressible. Due to this compressibility effect of the air, there is a variation of density as well as pressure. This pressure rise leads to the formation of shock wave.

The type of shock wave generated in a transonic airfoil cascade depends on some parameters such as free stream Mach number, geometry of the solid body, angle of attack, gap to chord ratio etc. The generated shock wave may be normal, oblique, λ -shock or bow shock etc. The flow field becomes unstable with shock wave generation and a wave drag is added with the viscous drag.

1.3 FLOW FIELD DEVELOPMENT IN COMPRESSOR CASCADE

Compressor is one of the most important components of a jet engine. Cascade refers to a series of blades which are arranged in certain repetitive fashion. Cascade is basically, a series of stationary or rotary blades. One might wonder why should we bother about a set of stationary and rotary blades and how does it help us in our analysis of compressor which primarily comprises of rotor (figure. 1.1) and stator. How can we gain any beneficial information from a series or set of blades? In fact, cascade plays a very significant role in our understanding of compressor and the performance behavior of a series of blades.

Usually in a compressor, the blades are arranged along on a disc or a drum, where as in a linear cascade blades are arranged in a straight line in one plane. In a rotor or stator, the blades are not really arranged in a linear fashion but are arranged on a rotary frame. That is one of the differences between cascade and the actual blades.

Cascade gives us some better understanding of a set of blades which are used in a similar fashion to that of compressors but in a much more simplistic way.

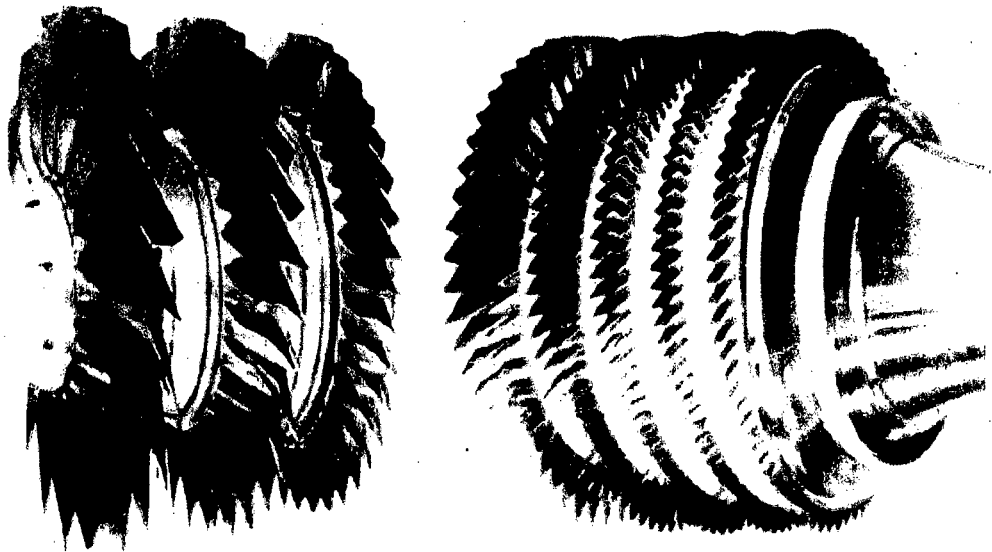


Figure. 1.1 Low pressure and high pressure compressor of a jet engine
(Eurofighter-Typhoon-engine-EJ200)

The idea of using cascades was developed long ago. In the early days when compressors were actually being developed and designed in the initial stages 60-70 years ago. During 1930s to 1940s cascades came to be of use for very simple testing and analyzing of compressor. Cascades are used even in turbine. But here we are focusing on compressor cascades. It was long back that these test methods were developed and they have been used ever since. It's still being used very popularly in today.

But the difference between the significance of cascade today and what it was 40-50 years ago is different. In today's technology a lot of significance is given to numerical analysis or computational analysis with the development and use of computational tools like CFD. So, the significance of cascade probably has slightly lower than what it was many years ago. But it does have a lot of significance because there is lot of uncertainty even till date, on some of the jet one get from computational analysis. So cascade is still used for validation of some of these computational tools. Cascade consist an array of blades which are arranged in a certain fashion. These blades are representative of the blades which would be used in an actual compressor. The difference is that usually cascades have blades which are 2D, which means that they usually are like airfoils sections which are extruded. Unlike an axial compressor where the blades are not necessarily 2D where the blades may have a twist and the blades can take 3D shapes, which is not true for a cascade.

Cascade basically relates or tries to gives us some information in fact a lot of information on how does a given set of blades behave in terms of the pressure rise on the blade surfaces. The c_p distribution on the blade surface as well as the losses that are encountered in total pressure rise because of frictional effects and so on, that is at the trailing edge of these blades. And how do these parameters change for a given turning of the blades.

For example, if we need to design a new series of blades which are to be used in an actual compressor. One of the ways to do that is to design the blades, fabricate the blades as it is and then test them in an actual test facility. The amount of time, effort and money that is required for testing actual compressor blades in an actual geometry is substantial. Therefore, we would like to first take a look at simplistic analysis which can tell us whether the blade is likely to perform well when it is actually implemented in a compressor. So cascade is one such way wherein we can get very quick results, very quick turn around from the simple experiments and at the same time they give a lot of insight in to the performance of these blades.

Cascade analysis can give us how the blades are going to perform as we keep changing the inflow angle that is known as incidence angle and what is the total pressure loss at this kind of blade geometry. These are the informations cascade analysis can provide us. That plays a very significant role in detailed design and analysis of compressor blades. So it is necessary that we first have a simplistic and a quicker experiment which can give us a lot of details and that can help us a lot in our understanding of the performance behavior of these blades. That is one of the aspect or beauty of cascade analysis. Cascade blades are usually mounted on a turn table which means whole set of blades can be rotated about a given axis. As we rotate these set of blades we are basically changing the incidence or the angle at which the flow is actually entering the cascade.

On the blade surface what we basically measure are the static pressures on both the suction surface and pressure surface. When these cascade blades are fabricated or manufactured they usually have these pressure tabs embedded on the blade surface. This will help us in giving some idea about the static pressure distribution on these blades and c_p distribution give us information about the loading

of the blade, how much force or how much work can this blade do on the flow. That is an indication of pressure rise which cascade can give us.

Internal flow through airfoil cascade (series of airfoil arranged together) is similar to the flow passing through the converging diverging nozzle as in both of the cases shock wave boundary layer interactions (SBLIs) occurs in the regions of supersonic and subsonic flows. Typically, such interactions are characterized by supersonic flow ahead of the shock wave and subsonic flow downstream of it [1].

When transonic flow occurs past an airfoil cascade a local supersonic flow region is formed known as supersonic bubble. Often this supersonic bubble is terminated by creating a shock wave. This shock wave adds an additional drag. This additional drag which is called a wave drag increases the required power input to operate turbo-machines. At some particular conditions this shock wave starts to oscillate over the airfoil surface. While oscillating the shock absorbs energy from the flowing fluid to maintain its oscillation. So this shock oscillation introduces another additional power loss. Not only the shock oscillation increases the required input power but also it causes pressure fluctuation over the airfoil surface which is the source of noise, vibration, fatigue and so on. For turbo-machines where high speed internal flow over airfoil cascade occurs (such as turbine, compressor etc.) the self sustained shock oscillation limits the performance of the machinery. Thus researchers are always concerned about the mechanism and control of this self sustained shock oscillation.

1.4 SELF SUSTAINED SHOCK WAVE OSCILLATION MECHANISM

Hendrik Tijdeman and B.H.K. Lee have proposed different mechanism of self sustained shock oscillation. These are based on the propagation of downstream moving pressure wave and the upstream moving waves created due to the disturbances at the trailing edge (TE). Tijdeman [2] presented the concept of the disturbance wave and concluded that these waves are created to satisfy the "Kutta condition" at the trailing edge. He referred this upstream moving wave as "Kutta wave". In his review paper Lee[17] described that there is a significant deviation between the time required to propagate the kutta wave from TE to the shock and the time period of the shock oscillation. Then he concluded Tijdeman's model as incomplete and proposed a close loop mechanism form the shock oscillation.

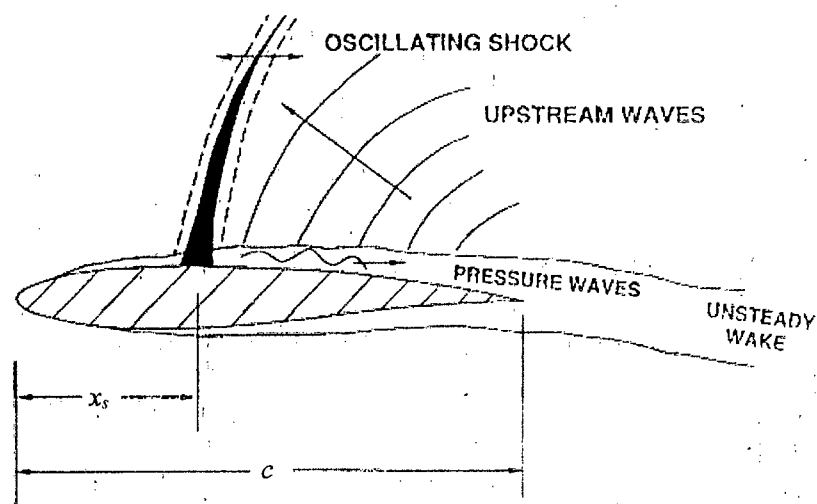


Figure. 1.2 Close loop mechanism of self sustained shock oscillation [17]

The loop starts as the shock oscillation creates the unsteady pressure fluctuation and that causes the generation of pressure wave at the shock foot. This pressure wave moves towards the TE through the separated flow region and interact with the disturbances created at the TE as shown in figure. 1.2. This interaction creates the upstream waves which propagate through the outside of the separated region. This upstream wave carries the required energy to the shock wave to maintain its oscillation and then the loop is completed. This type of shock oscillation is called self sustained shock oscillation as the shock oscillates without external energy input. The mechanism proposed by Lee is called as feedback mechanism. The mechanism assumes the flow past the airfoil is fully separated. Calculation of time period show that time required for the pressure wave and the upstream waves to complete one cycle is in good agreement with the oscillation time period.

1.5 TYPES OF SHOCK OSCILLATION

There are three types of shock oscillation (figure. 1.3). They are Tijdeman type A, Tijdeman type B and Tijdeman type C shock oscillation. Among these three categories type A shock oscillation is continuous but type B and type C are discontinuous oscillation.

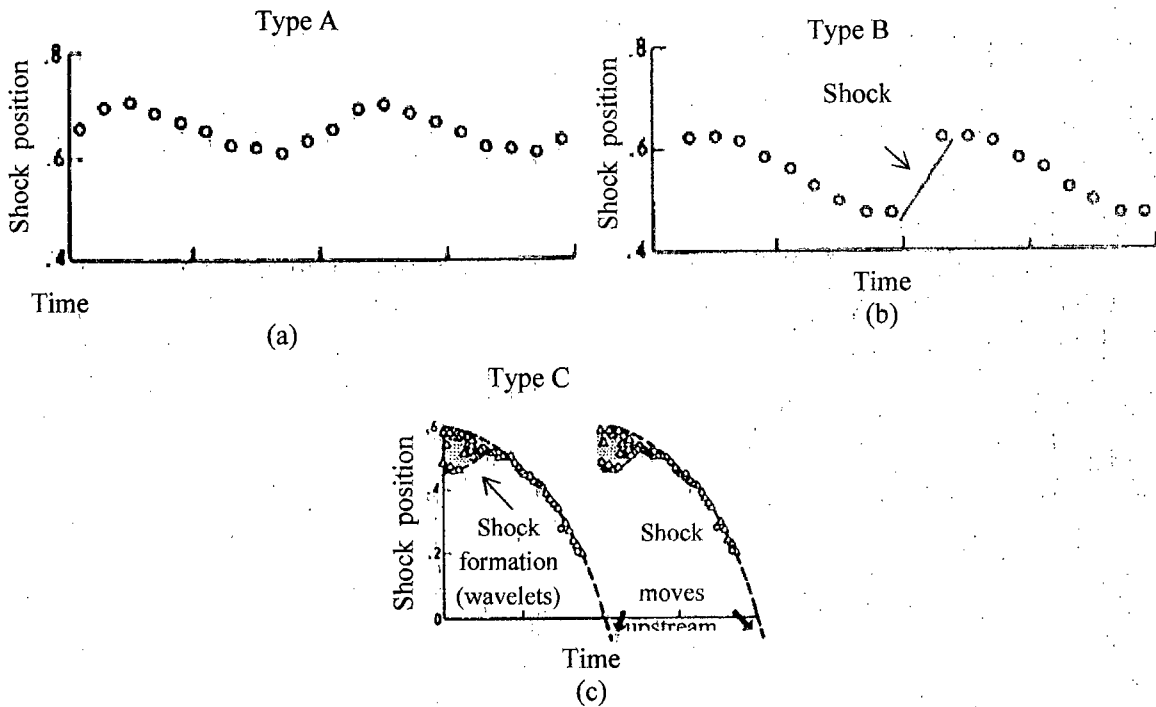


Figure. 1.3 Shock location with time for all three types of shock oscillation [17]

When the shock movement has continuous oscillation both on upper and lower surface (for symmetrical airfoil) with about 180° in phase is called type A shock oscillation. If the shock oscillates in a manner that the upper shock moves forward and eventually vanishes at about half of the total oscillation time period and the lower surface shock starts to move at about half of the cycle and then vanishes at about the end of the cycle is known as the type B shock oscillation. In case of type B shock oscillation, the shock on both surfaces travel about half of its path as a shock wave and then returns to its initial position as a compression wave. For the type C shock oscillation, the shock moves from trailing edge to leading edge direction as a shock wave and then turns into compression wave and that compression wave continues to move forward. Finally, the compression wave passes the leading edge and then the cycle starts again.

1.6 CASCADE GEOMETRY

A biconvex circular arc airfoil with chord length (c) of 48mm, maximum thickness of 12% of the chord length has been used in this research. This airfoil is considered as mid-airfoil with upper and lower surfaces. Besides, one upper airfoil lower surface and one lower airfoil upper surface are used to form the cascade geometry. Blade spacing is taken as $0.5c$. Airfoil cascade with different stagger angle (θ) 0° to 20° have shown here (figure. 1.4).

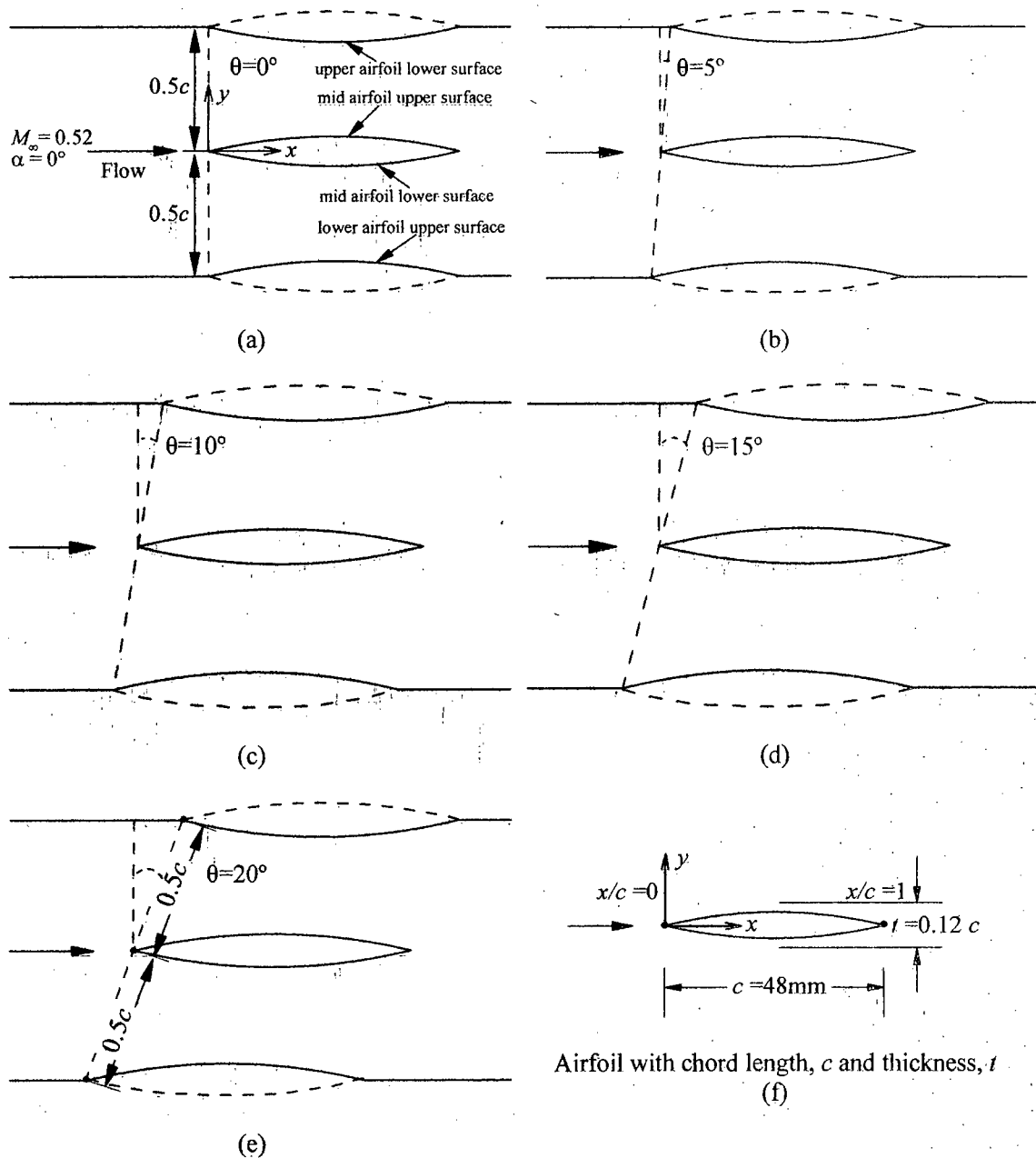


Figure.1.4 Base line airfoil geometry for different stagger angle(θ)
(a) $\theta=0^\circ$ (b) $\theta=5^\circ$ (c) $\theta=10^\circ$ (d) $\theta=15^\circ$ (e) $\theta=20^\circ$

1.7 OBJECTIVES

The objectives of this present study are:

- To develop a computational model to capture the unsteady shock wave dynamics around the airfoil cascade in transonic internal flow.
- To investigate the flow field in a transonic circular arc airfoil cascade at different stagger angle. Stagger angle will be varied from 0° to 20° in steps of 5° .
- To experimentally investigate the flow field in a transonic circular arc airfoil cascade for three different approach angles (0° , 5° and 10°).

CHAPTER 2

LITERATURE REVIEW

McDevitt et al. [1], studied the transonic flow over an 18% thick airfoil both experimentally and numerically. The study includes investigation of parameters like surface pressures, streamline, flow separation patterns and shadowgraphs. Test results are presented for Reynolds number 1 million to 17 million, covering laminar to fully developed turbulent flows. With the variation of the airfoil peak local Mach number from about 1 to 1.4, both weak and strong shock boundary-layer interactions are observed. For a limited range of free stream Mach number, the airfoil flow fields are found to be unsteady which can be investigated by the instantaneous pressure measurements and high-speed shadowgraph movies. The study also provides comparison of experimentally determined and numerically simulated results using a new viscous-turbulent code. The comparisons show the importance of including an accurate turbulence model. When the shock-boundary-layer interaction is weak the turbulence model employed appears adequate, but when the interaction is strong, and extensive regions of separation are present, the model is inadequate and needs further development. The results suggest that the shock-boundary-layer interaction phenomena are strongly dependent on Mach number and Reynolds number.

A detailed overview of the behaviors of the transonic flow around an oscillating airfoil has been discussed by Tijdeman [2]. The study includes experimental analysis with the exploratory wind-tunnel at high-subsonic and transonic flow on a conventional airfoil with oscillating flap and a supercritical airfoil oscillating in pitch. In the analysis of the experimental results the study emphasized upon the typical aspects of transonic flow, namely the interaction between the steady and unsteady flow fields, the periodical motion of the shock waves and their contribution to the overall unsteady air-loads. Special attention is paid to the behavior of the supercritical airfoil in its "shock-free" design condition. Moreover, it is discussed to what extent linearization of the unsteady transonic flow problem is allowed if the unsteady field is considered as a small perturbation superimposed upon a given mean steady-flow field. Finally, the current status of unsteady transonic flow theory is reviewed and the present test data are used to evaluate some of the recently developed calculation methods.

Levy Jr. [3] had described an experimental and computational investigation of the steady and unsteady transonic flow fields about a thick airfoil. An operational computer code for solving the two dimensional, compressible Navier-Stokes equations for flow over airfoils was modified to include solid-wall, slip-flow boundary conditions. Steady and unsteady flow-fields about an 18% thick circular arc airfoil at Mach numbers of 0.720, 0.754 and 0.783 and a chord Reynolds number of 11×10^6 are predicted and compared with experimental results. From the comparisons it is observed that the pressure and skin-friction distributions show improved agreement when test-

section wall boundaries are included in the computations. Steady-flow results were good in quantitative agreement with experimental data for flow conditions which result in relatively small regions of separated flow. For flows with larger regions of separated flow, improvements in turbulence modeling are required. The results suggest use of computer codes with proper boundary conditions, an improved tool with proper turbulence models. It can be seen that Navier-Stokes type computer codes are capable of reproducing the time-dependent aspects of unsteady turbulent flows involving weak and strong shockwave boundary-layer interactions. These results had inspired confidence that once turbulence models are developed with which the improved computer codes can predict experimental steady-flow results, the codes can then be used to study the time-dependent aspects of unsteady flows and hence provide insight into unsteady aerodynamic phenomena such as buffeting, inlet buzz, and rotating helicopter blades.

Tijdeman and Seebass [4] had added different information to understand the transonic flow past oscillating airfoils. By that time, the recent studies have provided results essential for the design of transonic aircraft. The main limitations of these experiments were their failure, for the most part, to duplicate full scale Reynolds numbers and an inability to duplicate free flight conditions due to wind tunnel wall interference. Experimental studies, both in progress and planned for the future, would be more nearly at full-scale Reynolds number, and eventually these Reynolds numbers would be obtained with minimum wall interference in new facilities now under development.

Paralleling this progress had been a rapid development of reliable, and in the small perturbation approximation, efficient numerical algorithms for the computation of inviscid flows. Numerical results from these methods were in qualitative agreement with the experimental observations, with the main discrepancies in quantitative prediction as a consequence of the inviscid approximation. For steady flows coupled inviscid-boundary layer calculations of unseparated flows had obtained quantitative agreement with experimental measurements. He had expected this to be true for unsteady flows in the near future. The numerical simulation of unsteady separated flows was demonstrably possible, but the two orders of magnitude improvement in computer speed that was projected for a special-purpose aerodynamic computer would be essential for this simulation to have practical consequences. It was the authors' opinion that the satisfactory prediction of unsteady airloads for aeroelastic applications was within reach. This could be accomplished by "tuning" inviscid boundary conditions to model an experimentally determined steady flow and then computing its unsteady response using an inviscid small-perturbation algorithm. Thus, the time was ripe to start with the incorporation of the new methods in aero elastic practice as recently demonstrated by Ashley (1979). Of course, the use of two-dimensional methods is justified only for large aspect-ratio wings. To treat the low aspect-ratio configuration the next, and not difficult, step had to be made, namely, the development of prediction methods for three-dimensional flows.

Gronland et al. [5] discussed the accuracy one can obtain in predictions of unsteady transonic flows by a modern CFD method using a time accurate Reynolds-averaged Navier-Stokes solver. The test case used in the study is an 18% thick biconvex, two dimensional airfoil. Experiments have revealed that this geometry had showed a strong oscillatory flow in a certain regimes, often referred to as buffet. Sensitivity to numerical and physical modeling was assessed through repeated computations with various spatial and temporal discretization, numerical schemes and different types of turbulence models. The correlation between the airfoil in a free flight and in a wind tunnel environment was also investigated. It had shown that modern CFD methods can indeed predict the complex buffet phenomena with reasonable accuracy. This work highlights some of the most critical aspects of physical and numerical modeling of buffet. It was also shown that lift and drag on the airfoil differs considerably between the free flight and wind tunnel environments.

McDevitt et al. [6] continued the early study and extends the original test program to include effects of angle of attack, effects of leading and trailing-edge splitter plates, additional unsteady pressure fluctuation (buffeting) measurements and flow-field shadowgraphs, and application of an oil-film technique to display separated-wake streamlines. Detailed comparisons of computed and measured pressure distribution for steady and unsteady flows, using a recent computer code representative of current methodology, are included. It was found that the numerical solutions are often fundamentally incorrect in that only "strong" (Shock-polar terminology) shocks are captured, whereas experimentally, both strong and weak shock waves appear.

Li et al. [7], experimentally investigated the effects of divergent trailing edges and Gurney flaps on a supercritical airfoil at a Mach number $M = 0.7$ and a Reynolds number $Re = 3.15 \times 10^5$ based on the airfoil chord length. The effects of Gurney flaps with height $h = 0.5\%$, 1.0% , and 2.0% chord length, respectively. The results revealed that, in comparison with the divergent trailing edge, the gurney flaps had significant effects on improving the aerodynamics characteristics of the tested supercritical airfoil, and even on the airfoil with divergent trailing edge. When the Gurney flaps were utilized, the lift coefficient, maximum lift coefficient and the maximum lift-to-drag ratio of both supercritical and divergent trailing edge airfoils were greatly increased. The lift-enhancing effects on Gurney flaps under high-speed circumstances mainly came from its ability of shifting backward the shock on the upper surface. Moreover, the installation of Gurney flaps will increase wave drag and base-pressure drag, but at the same time, the pressure on the lower surface of the airfoils was increased which lead to an increased rear-body loading, and the position of the shock of pressure on the upper surface was greatly shifted backward, the supersonic region is thus enlarged, which led to an increased suction. Both the increments of pressure on the lower surface and suction on the upper surface resulted in a total lift increase. As the lift did not increase with the drag linearity, the lift-to-drag ratio increase and aerodynamics characteristics improvement were obtained under some circumstances.

Alfano et al. [8] had worked with external or internal transonic flows using a standard $k-\epsilon$ turbulence model relying on the Boussinesq assumption. The study states a linear dependence of the turbulent

stresses on the mean shear stress, does not allow the successful prediction of unsteady flow phenomena such as self-sustained shock oscillations, because of an excessive production of turbulent kinetic energy. A weak non-linear correction that makes the eddy viscosity coefficient dynamical and a so-called PANS approach that modifies the dissipation rate equation allow to improve the standard model so as to predict the appearance of self-sustained shock oscillations over an airfoil and in a diffuser. The computed cases and the results obtained regarding both external and internal aerodynamics, highlight the need for a true research effort for the efficient and adapted simulation of low-frequency self-induced transonic flow oscillations. A clear limitation of this work is the assessment of the PANS approach on bi-dimensional grids only. Hybrid turbulence modeling may strongly depend on the chosen turbulence model. Clearly, the evolutions of the work will be strongly dependent of the currently intense research effort in hybrid turbulence modeling. Due to the low main frequencies and high Reynolds numbers involved, which prohibit any affordable Large Eddy Simulations attempts, hybrid turbulence modeling however appears as a real future need for the transonic flows.

Raghunathan et al. [9] had reviewed the understanding of periodic transonic flow briefly. The effects of boundary-layer Transition, non-adiabatic wall conditions and modifications to the airfoils surface geometry at the shock interactions on periodic transonic flow are discussed. Through the methods presented, it is proposed that the frequency of the periodic motion can be predicted with reasonable accuracy, but there are limitations on the prediction of the buffet boundaries associated with periodic transonic flows. Several methods have been proposed by which the periodic motion may be virtually eliminated, most relevantly by altering the position of transition fix, contouring the airfoils surface or adding a perforated surface and a cavity in the region of shock interaction. In addition, it has been shown that heat transfer can have a significant effect on buffet. The paper has reviewed the current understanding of periodic transonic flow over circular, NACA0012 and supercritical airfoils and the use of devices to control the periodic motion.

In the numerical investigation of Chen et al. [10] various fundamental mechanisms dictating the intricate flow phenomena, including moving shock wave behaviors, turbulent boundary layer characteristics, kinematics of coherent structures and dynamical processes in flow evolution, have been studied systematically. A feedback model is developed to predict the self-sustained shock wave motions repeated alternately along the upper and lower surfaces of the airfoil, which is a key issue, associated with the complex flow phenomena. Based on the moving shock wave characteristics, three typical flow regimes are classified as attached boundary layer, moving shock wave, turbulent boundary layer interaction and intermittent boundary layer separation. The turbulent statistical quantities have been analyzed in detail, and different behaviors are found in the three flow regimes. Some quantities e.g. pressure-dilatation correlation and dilatational dissipation, have exhibited that the compressibility effect is enhanced because of the shock wave boundary layer interaction. Further, the kinematics of coherent vertical structures and the dynamical processes in flow evolution

are analyzed. The speed of downstream-propagating pressure waves in the separated boundary layer is consistent with the convection speed of the coherent vertical structures. The multi-layer structures of the separated shear layer and the moving shock wave are reasonably captured using instantaneous Lamb vector divergence and curl, and the underlying dynamical processes are clarified. In addition, the proper orthogonal decomposition analysis of the fluctuating pressure and the separated shear layers in the trailing-edge region. The results obtained in this study provide physical insight into the understanding of the mechanisms relevant to this complex flow.

Catalano and Tognaccini [11] analyzed the incompressible flow at Reynolds number 6.0×10^4 around the Selig-Donovan 7003 airfoil. The airfoil performances have been computed by the Reynolds averaged Navier-Stokes equations and large eddy simulations. The airfoil stall and preliminary post-stall have been obtained by the both methods. Some limitations of RANS turbulence models for low-Reynolds number flows have been overcome by the $k-\omega$ SST-LR model, a recent modification of the well-known SST model. Large-eddy simulations have also been performed for a more detail analysis of the results. The relevance in the stall mechanism of the laminar separation bubble arising on the airfoil is highlighted. The stall occurs when the laminar bubble present in the leading edge zone and a separated region forming on the central part of the airfoil join together. The $k-\omega$ SST-LR model returns the same stall mechanism as the large eddy simulation. Flows at low-Reynolds numbers can be simulated by the RANS methods, but the choice of the turbulence model is crucial. The $k-\omega$ SST-LR model has provided results in good agreement with the large eddy simulation and the available experimental data. Time accurate URANS simulations are performed at high angles of attack in order to achieve converged steady-state results. The main conclusion of this paper is that flows at low-Reynolds number and the peculiar phenomenon of the laminar separation bubbles can be simulated by the RANS approach. As the angle of attack increases and a converged solution is not easily recovered, time-accurate URANS simulations need to be performed. The choices of the turbulence model and of a proper transition location in the model itself resulted crucial. The $k-\omega$ SST-LR model and an empirical criterion for the transition location have provided satisfactory results at least for the test-case presented in this paper.

Hasan et al. [12] had discussed the shock induced oscillation around an airfoil in transonic internal flow fields are often observed due to complex shock wave boundary layer interaction. However, in actual flow where finite amount of water vapor is present in the air, the rapid expansion of the flow may give rise to non-equilibrium condensation. Effects of condensing moist air on unsteady shock induced oscillation were numerically studied for total back pressure to reservoir pressure ratios of 0.73-0.65. Results showed that in case with condensing moist air flows, the root mean square of the shock induced pressure oscillation and the oscillation frequency were reduced significantly compare with those without the non-equilibrium condensation. However, there was an increase of total pressure loss for condensing moist air flows.

In the paper of Xiong et al. [13], the performance of four different turbulence models in addressing shock wave-boundary layer instabilities is investigated. The problem chosen for this goal is a transonic flow over a 10% thick circular arc airfoil in a channel. The self-excited shock motion over the circular arc airfoil has been investigated before experimentally and those results are used as a benchmark for the current study. Unsteady RANS and DES methods in combination with different turbulence models are used. All the method can successfully predict the overall shock oscillatory behavior. Yet there are minor differences in frequency prediction. Another reason for choosing this problem is to better understand the physics governing the problem. It is found that the shock oscillation frequency strongly depends on mean shock wave location. All the turbulence models successfully capture the oscillatory behavior of the flow in a certain pressure range, even though the pressure does not completely match the experiments. S-A model seems to be under-predicting the oscillation frequency in comparison to the other methods. Also perfect match between shock wave location and frequency was observed. It seems that to have the numerical solution match the experiments, special attention must be paid to predict the shock wave location precisely on the airfoil. This in turn signifies the inlet profile boundary condition as a potent field for future studies. At the current stage the models are capable of predicting trends observed in experiment correctly. It is also shown that $k-\omega$ SST unlike S-A turbulence model can achieve results as accurate as DES model. Also three dimensional computation of this problem can be very important since all the two dimensional computations predict oscillation frequencies which are 50 to 100 percent higher than the experimental results. This means that there might be three dimensional mechanisms that govern the oscillation frequency.

Bendiksen [14] reviewed unsteady transonic flow theory and classical results from the non-linear asymptotic theory are combined with new results from computational fluid dynamics. The emphasis is on application to the field of aeroelasticity and on clarifying the limitations of linearized theories in problems involving mixed subsonic-supersonic flows. The inherent differences between non-linear transonic aerodynamics and linear subsonic and supersonic aerodynamics are considered from theoretical and computational standpoint, and the practical implications of these differences in formulating suitable aerodynamics models for aeroelastic stability calculations are discussed. Transonic similarity principles are reviewed and their relevance in understanding flutter, divergence, and control reversal phenomena of transonic aircraft is illustrated through practical example. Transonic flutter is rich in non-linear dynamic phenomena that cannot simply be modeled with ideas based on linear aerodynamics. Superficially, the dynamics may appear to the non-linear behaviors of classical mechanical systems, but there are important mathematical and physical differences. First, aero-elastic systems are essentially non-conservative involving circulatory forces and cannot be modeled simply as dissipative mechanical spring-mass-damper systems, with a damping that becomes negative as the flutter boundary are crossed. Second, in the transonic case entropy production at the moving shocks introduces a type of irreversibility that is not found in the

corresponding mechanical system, and which results in entropy and vorticity waves being convected downstream, affecting the global aerodynamics solution and possibly also the stability of the fluid structure system. In transonic flutter, non-uniformities on the time scale affect stability by destroying time invariance.

Yagiz et al. [15] had discussed the predictability of weakening the shock wave and hereby reducing the wave drag in transonic flight regime using flow control devices such as two-dimensional contour bump, individual jet actuator, and also the hybrid control which control devices together, and thereby to gain the desired improvements in aerodynamic performance of air-vehicle. To validate the numerical study, an efficient gradient based numerical study, a natural laminar flow airfoil, Rae5243, is chosen and then comparisons with experimental data have been made before the optimization technique is used to optimize 2D bump parameters including the length, the maximum height, the bump position via shock location, and the crest position via bump and also the jet actuation parameters such as mass flow coefficient. Suction/blowing angle, actuation location over the upper surface of the airfoil. The process generally consists of using the simulation code to obtain a flow solution for given parameters and then search the optimum parameters to reduce the total drag of the airfoil via the optimizer. Most importantly, it is shown that, the optimization yields 3.94% decrease in the total drag and 5.03% increase in lift, varying the design parameters of active and passive control devices.

Eleni et al. [16] had done the analysis of the two dimensional subsonic flow over a National Advisory Committee for Aeronautics (NACA) 0012 airfoil at various angles of attack and operating at a Reynolds number of 3×10^6 is presented. The flow was obtained by solving the steady-state governing equations of continuity and momentum conservation combined with one of three turbulence models (Spalart-Allmaras, Realizable k- ϵ and k- ω shear stress transport (SST)) aiming to the validation of these models through the comparison of the predictions and the free field experimental measurements for the selected airfoil. The aim of the work was to show the behavior of the airfoil at these conditions and to establish a verified solution method. The computational domain was composed of 80000 cells emerged in a structured way taking care of the refinement of the grid near the airfoil in order to enclose the boundary layer approach. Calculations were done for constant air velocity altering only the angle of attack for every turbulence model tested. This work highlighted two areas in computational fluid dynamics (CFD) that require further investigation: transition point prediction and turbulence modeling. The laminar to turbulent transition point was modeled in order to get accurate results for the drag coefficient at various Reynolds numbers. In addition, calculations showed that the turbulence models used in commercial CFD codes does not give yet accurate results at high angles of attack.

Eventually Lee [17] suggested a physical mechanism of the periodic shock motion based on the study of Tijdeman [2]. The mechanism is explained considering the flow downstream of the shock is fully separated. The mechanism suggested in this study is described in section 1.2. The complete

understanding of the mechanisms responsible for self-sustained oscillations of the shock waves under wide ranges of conditions, such as Mach number, incidence angle, Reynolds number, and airfoil geometry has not yet been achieved. A detailed investigation of flow field is carried out for both symmetrical airfoils at zero incidence and supercritical airfoil at incidence. The results show that there are narrow ranges of Mach numbers where shock oscillations can occur on the upper and lower surfaces of the airfoil.

Alshabu and Olivier [18] experimentally investigated the wave phenomena around a supercritical BAC3-11 airfoil in Mach numbers 0.65 to 0.8 at zero incidence angle. Time-resolved shadowgraphs and Schlieren pictures showed pressure waves initiated near the trailing edge and propagating upstream, where they become apparently weaker near the leading edge. These wave processes were accompanied by wake fluctuations and vortex generation in the boundary layer. The observed waves were also captured by pressure transducers mounted in the airfoil model. The dominant frequencies ranged between approximately 0.7 and 1.5 kHz. Using statistical analysis of the pressure histories, wave propagation direction and wave speed were determined. For higher flow Mach numbers, a strong wave shock interaction was also observed in which the shock, depending on the shock strength, was attenuated and degenerated into compression waves.

Zhao et al. [19] performed an experimental study on shock wave oscillations over SC (2)-0714 supercritical airfoil. The experiment was executed in the NPU NF-6 transonic wind tunnel at free stream Mach number from 0.72 to 0.82. Reynolds number based on the airfoil chord was changed from approximating 3.0 million to 5.0 million with transition strip fixed at 28% chord length. The result included spectrogram result at different x/c position under several angles of attack. Results showed that reduced frequency had increased from 0.44 to 0.63 when the angle of attack had increased. The spectrum graph had some low frequency oscillation appeared. It might be caused by background turbulence and unsmoothness of the model surface. The cross-correlation coefficients of pressure fluctuations of several Kulite transducers on the upper surface were used to calculate the pressure wave's propagation upstream within the separation region between the shock wave and the airfoil trailing edge.

Very recently, the interaction between the shock wave and the turbulent boundary layer was investigated over OAT15A supercritical airfoil Srator et al. [20]. In agreement with previous results, it was found that the buffet phenomenon was driven by an unstable global mode of the linearized Navier-Stokes equations. Analysis of the adjoint global mode revealed that the flow was most receptive to harmonic forcing on the suction side of the profile, within the boundary layer upstream of the shock foot. An Eigen value sensitivity analysis showed that a steady stream wise force applied either in the boundary layer or in the recirculation region, a steady cooling of the boundary layer, or a steady source of eddy viscosity (a mechanical vortex generator for example) all led to stabilization of the buffet mode. Finally, pseudo resonance phenomena have been analyzed by performing a singular-value decomposition of the global resolvent, which revealed that, besides the low-

frequency shock unsteadiness, the flow also underwent medium-frequency unsteadiness, linked to Kelvin-Helmholtz type instability. Such results were reminiscent of the medium-frequency perturbations observed in more traditional shock wave boundary layer interactions.

Qin et al. [21] numerically demonstrated the effectiveness of some active shock control mechanism such as suction and injection. A brief description of the flow model and the numerical method is presented including, in particular, the boundary condition modelling and the numerical treatment for surface mass transfer. The effects of surface suction, blowing, and local modification of the surface contour (bump) on aerofoil aerodynamic performance have been studied extensively regarding the control location, the mass flow strength and the bump height.

Stanewski [22] investigated various conventional and novel means of boundary layer and flow control applied to moderate-to-large aspect ratio wings, delta wings and bodies with the specific objectives of drag reduction, lift enhancement, separation suppression and the improvement of air-vehicle control effectiveness. In addition, adaptive wing concepts of varying complexity and corresponding aerodynamic performance gains were discussed, also giving some examples of possible structural realizations. Numerous devices for lift enhancement and separation suppression had been successfully investigated among them trailing-edge devices, such as Gurney flaps, divergent trailing edges, reversed-flow flaps and taps, conventional and sub-boundary-layer and air-jet vortex generators, and mass-less jets. For shock control the contour bump and discrete slot suction upstream of the shock-in that order-were found to be most effective when drag reduction is the main objective. Effectiveness in reducing drag was found similar to the much more complex wing upper-surface adaptation.

Li et al. [23] proposed micro-blowing as another flow control technique. The interaction of cross flows over micro-porous walls composed of micro-channels with the flows through the channels was simulated by solving the Navier-Stokes equations, and $k-\omega$ SST closure model was employed for the turbulent cross flows. Preliminary results had demonstrated that the effects of micro-blowing on the flow field were limited within the viscous sublayer of the cross flows, and the influential zone was confined in a small region surrounding the porous zone. The study confirmed that promising features on frictional drag reduction could be realized by micro-blowing technique. The capacity of drag reduction was found to be proportional to the blowing fraction. The reduction of frictional drag could even be achieved with zero blowing, implying that the micro-holes gave little effect to the surface roughness of the wall, but were capable of steepening the velocity profiles, i.e., lessening the normal velocity gradients near the wall.

Among passive control techniques, micro-ramps, bumps and cavities were demonstrated as promising control mechanisms [24, 25, 26].

Ashill et al. [26] proposed to control the flow in the region of shock wave by locally altering the aerofoil or wing boundary conditions. He proposed to deploy bumps or ramps as variable-geometry devices. It was found that shock control bump offered significant benefits in controlling flows over highly swept wings suitable for combat aircraft, providing a reduction in lift dependant drag of up to 16%. The use of bumps or ramps in the region of the shock, either as fixtures or as active devices, provided significant reductions in drag typically about 12%. A buffet bump placed downstream of the shock could provide significant increases in lift coefficient for buffet onset, while not increasing drag at cruise conditions.

The optimum size, shape and location of the shock control bump have been investigated in References [27, 28]. Patzold et al. analyzed 2d-optimized shock control bumps for the unswept and swept wing. The finite span SCBs consisted of three regions, a luff side step region, a linear part, and a leeward step region. Stream wise SCB contours were either determined in a 2d optimization or individually optimized for the various finite span SCBs. While these SCB contours showed rather good performance in the unswept case, only around 25% efficiency was achieved with wing sweep. For the oblique flow case SCB contours were individually optimized at two span wise locations for finite SCBs with varying span wise extensions. The SCB-efficiency was significantly increased by adapting the span wise contours. Unlike the unswept case no increased aerodynamic efficiency was observed for span wise small SCBs. The finite span SCB with a width of $b_{SCB} = 0.5 c$ had around 50 to 55 % efficiency. For these span wise small SCBs the efficiency could be increased by reducing, or if so optimizing, the sizes of the luff and leeward step regions. Tian et al. studied the effect of shock control bump on supercritical airfoil RAE2822. Based on improving the airfoil's lift-drag ratio, the study showed that, (1) the best bump crest position was at the position close to 50% of bump chord, which was almost independent of free stream or pre-shock Mach numbers, but the bump height was highly coupled with the crest position, which meant that the higher the bump was, the more obviously the crest position affected the airfoil lift-drag ratio, and it became more evident with the increase of free stream or pre-shock Mach numbers; (2) in case that the lift-drag ratio of airfoil with bump was higher than basic airfoil, almost all the optimum distances between bump crest and shock wave were close to 30% of bump chord; (3) almost all the lift-drag ratios of airfoil with bump increased as bump chord length increased, of which this trend became more evident as bump height increased; (4) with the increase of the bump height, almost all the lift-drag ratios of airfoil with bump decreased at low free stream or pre-shock Mach numbers.

Mazaheri et al. [29] investigated two different strategies for bump optimization. One with constant angle of attack and the other with constant lift coefficient. They found that the former design provides an optimum aerodynamic performance while the latter one provides optimum level flight. The survey was conducted for three airfoils through detailed SCB shape optimization processes employing differential evolution algorithm (DE). All optimization and analysis were mainly presented for airfoil RAE2822, but two other airfoils (i.e. NACA 64A010 and RAE 5243) were also

studied to show that results are extendable to most transonic airfoils. SWBLI was analyzed thoroughly for clean and bumped airfoils and it is shown how the modified wave structure originating from upstream of SCB reduces the wave drag while simultaneously improving the boundary layer velocity profiles downstream of the shock wave. It was shown that how the shock wave interacts with the boundary layer on the SCB and how the isentropic wave pattern generated by the SCB weakened the shock wave and energizes the boundary layer in the recovery region. This prohibited boundary layer growth, and delayed separation. A detailed analysis of the velocity profiles in the boundary layer was used to compare clean airfoil with constant angle of attack and constant CL optimized bumped airfoils. The analysis was extended to the structure of the wake region, to show how the optimized shape, especially the constant CL case, produced more symmetric and uniform velocity.

The capability of shock control bump in controlling shock wave oscillation has also been reported by Hasan and Alam [30]. Self-excited shock induced oscillation (SIO) around an airfoil was observed in transonic flows at certain conditions of free stream Mach number and angle of attack. At these conditions, the interaction of unsteady shock wave with airfoil boundary layer became complex and caused several detrimental effects such as the fluctuating lift and drag coefficients, aero acoustic noise and vibration, high cycle fatigue failure (HCF), buffeting and so on. In the study, Reynolds Averaged Navier-Stokes equations had been used to predict the aerodynamics behavior over a NASA SC(2) 0714 supercritical airfoil in transonic flow conditions. To suppress the unsteady aerodynamic behavior, a shock control bump was introduced at the mean shock position. Computations had been performed at free stream Mach number of 0.77 while the angle of attack was varied from 2° to 7° . The results obtained from the numerical computation had been validated with the experimental results. Mach contour, lift and drag coefficient, and pressure history over the airfoil surface had been analyzed for the cases of baseline airfoil and airfoil with bump. It is found that, the bump could control the unsteady SIO in the flow field.

Another promising shock control technique is the shock control cavity which is not well explored until now. McComick [31] described an experimental comparison of two passive approaches for controlling the shock interaction with a turbulent boundary layer: low-profile vortex generators and a passive cavity (porous wall with a shallow cavity underneath). The experiments were conducted with a normal shock wave in an axi-symmetric wind tunnel. The shock strength ($M = 1.56-1.65$) was of sufficient magnitude to induce a large separation bubble, thus causing substantial boundary-layer losses. The low-profile vortex generators were found to significantly suppress the shock-induced separation and improve the boundary-layer characteristics downstream of the shock. However, the suppression of the separation bubble decreased the extent of the low total pressure loss region associated with the lambda foot shock system which results in a lower mass-averaged total pressure downstream of the shock. The passive cavity substantially reduced the total pressure loss through the shock system (and thus wave drag) by causing a more isentropic compression over a larger

lateral extent. However, the boundary-layer losses downstream of the shock were significantly increased. The two methods offered different advantages and disadvantages. For example, if wave drag reduction of an isolated airfoil was required, then the passive cavity approach was favoured. However, if a supersonic diffuser was the application then the vortex generator approach was probably favoured because the shock-induced separation, which usually limits diffuser performance, was suppressed allowing more subsonic pressure recovery to be obtained.

Smith et al. [32] performed the Reynolds Averaged Navier-Stokes computations of groove controlled and uncontrolled shock wave boundary layer at a Mach number of 1.29, and the results validated against experiment. Features of the uncontrolled interaction were accurately captured, including the upstream influence, static pressure rise, and the effect of shock structure on downstream total pressure losses. The main features of the groove controlled interaction were also predicted by the RANS solver and the interaction featured a large lambda type structure with an oblique leading leg and a curved rear leg separated by a region of expansion. These expansion waves were a result of boundary layer relaxation over the groove. The expansion waves were responsible for the curved, nearly normal rear leg of the shock structure, which increased total pressure losses downstream of the interaction and reduced the beneficial effects of control. Two pairs of counter rotating vortices were detected in the interaction. The origins of one pair of vortices was found to be at the leading edge of the grooves and was formed due to a roll up fluid blown from the groove. The second pair of counter rotating vortices was also a result of transpiration from the groove. Blowing from the groove produced a flow separation, leading to the formation of a vortex pair. These vortices were found to move over the groove at a stream wise location which corresponded to reduced transpiration from the control. This reduced transpiration was responsible for the relaxation of the boundary layer.

Rowley and Williams [33] reviewed the significant progress in understanding and controlling cavity flow oscillations that was made in the past few decades. Early experiments used passive techniques, open-loop forcing, or closed-loop forcing with only the broadest heuristics to guide the control design. In the review closed-loop control had demonstrated the potential for reduction in oscillations with an order of magnitude less power required, and adaptive controllers had demonstrated control over a range of flow conditions. They suggested that the development of better control-oriented models, and the validation of these models with careful experiments and simulations, can help to fill these gaps in our understanding, and enable the benefits experienced in the laboratory to be achieved at full scale.

Olsman and Colonius [34] performed two-dimensional direct numerical simulation of the flow over a NACA 0018 airfoil with a cavity. The low Reynolds number simulations were validated by means of flow visualizations carried out in a water channel. From the simulations, it followed that there were two main regimes of flow inside the cavity. Depending on the angle of attack, the first or the second shear-layer mode (Rossiter tone) was present. The global effect of the cavity on the flow

around the airfoil was the generation of vortices that reduced flow separation downstream of the cavity. At high positive angles of attack, the flow separates in front of the cavity, and the separated flow interacted with the cavity, causing the generation of smaller-scale structures and a narrower wake compared with the case when no cavity was present. At certain angles of attack, the numerical results suggested the possibility of a higher lift-to-drag ratio for the airfoil with cavity compared with the airfoil without cavity. The simulations have revealed interesting flow physics associated with the interaction of no less than three different types of instabilities. These are the first- and second-cavity shear-layer modes and separation bubble behavior, which is forced by a shear-layer oscillation.

Very recently, an investigation for self-excited shock oscillation around a biconvex circular arc airfoil in transonic internal flows has been performed by Rahman et al. [35]. The upstream Mach number is kept at 0.61 while the airfoil was at zero angle of attack. The computational results are validated with available experimental data. In case of base line airfoil, the self-excited shock oscillation is observed for all the cases of pressure ratio 0.71 to 0.75. The self-excited shock oscillation disappears and shock wave remains steady with the introduction of cavity in the airfoil surfaces for pressure ratio 0.71. Amplitude of pressure oscillation in the flow field is reduced in case of airfoil with cavity at pressure ratio 0.72 to 0.75. The RMS of pressure oscillation significantly reduced throughout the flow field in case of airfoil with cavity. However, frequency of shock oscillation increases for the case of airfoil compared to baseline airfoil.

The passive control by surface modification was demonstrated experimentally by Bahi et al. [38]. This study includes experimentation of a porous surface and a cavity or plenum underneath. The control device is installed in the region of shock boundary layer interaction. It is suggested that the pressure rise across the shock wave will result in flow through the cavity from downstream to the upstream of the shock. This is equivalent to a combination of suction of downstream and blowing of upstream. The cavity could also increase the communication of signals across the shock wave. These effects could lead to a rapid thickening of boundary layer just ahead of the shock which produces a system of weaker shock with an extended interaction zone.

Then many researchers studied the effect of surface modification of airfoil to control the shock oscillations, high speed impulsive (HIS) noise etc. Nagamatsu et al. [39] experimentally studied the transonic flow over airfoil and investigated the effect of perforated cavity on drag minimization. The same results were obtained by Raghunathan et al. [40], suggesting a secondary reverse flow through the cavity. This study shows that perforated cavity can be used effectively only for strong shock wave.

Doerffer et al. [41] investigated the effect of perforated cavity on high speed noise reduction for a high speed helicopter rotor. This study concluded that the perforated cavity can lower the pressure fluctuation on the airfoil surface and thus the high speed noise is reduced. Yamamoto et al. [42] investigated a self excited oscillation of transonic flow in a simplified cascade model. The study

includes experimental, numerical and theoretical analysis. The results predicted a close loop mechanism of self sustained oscillation as proposed by Lee [17]. The conclusion of this study include that the flow field is more stable acoustically when the shock wave stands near the trailing edge because for this case generation of much larger pressure wave is necessary for shock oscillation.

Hamid et al. [44] studied the internal flow over a 12% thick airfoil and showed that the variation of flow characteristics and shock oscillation is dependent on the downstream pressure of the airfoil. The study shows that a clean biconvex circular arc airfoil (with no control technique) operating at pressure ratio (ratio of back pressure to upstream total pressure) 0.70 results a discontinuous shock oscillation which is known as Tijdeman type B shock oscillation.

Schreiber and Starke [45] performed experiments in a supersonic cascade facility to elucidate the fluid dynamic phenomena and loss mechanism of a strong shock-wave turbulent boundary layer interaction in a compressor cascade. The cascade geometry is typical for a transonic fan tip section that operates with a relative inlet Mach number of 1.5, a flow turning of about 3° and a static pressure ratio of 2.15. The strong oblique and partly normal blade passage shock-wave with a pre-shock Mach number level of 1.42 to 1.52 induces a turbulent boundary layer separation on the blade suction surface. Free stream Reynolds number based on chord length was about 2.7×10^6 . Cascade overall performance, blade surface pressure distributions, Schlieren photographs, and surface visualisations are presented. Detailed Mach number and flow direction profiles of the interaction region (lambda shock) and the corresponding boundary layer have been determined using a Laser-2-Focus anemometer. The obtained results indicated that the axial blade passage stream sheet contraction (axial velocity density ratio) has a significant influence on the mechanism of strong interaction and the resulting total pressure losses.

Kusters and Schreiber [46] studied the internal flow through supersonic compressor cascade numerically. They applied a 2D multi-block Navier-Stokes solver to a supersonic compressor cascade flow with strong shock-wave/boundary-layer interaction. Numerical calculations have been performed on a very fine grid to guarantee sufficient resolution of the supersonic/transonic flow field with a complex wave pattern and shock induced boundary layer separation. Investigations are performed for inlet Mach numbers from 1.28 to 1.53 and a Reynolds number of 2.6×10^6 . The results are compared with those of previous experiments in a supersonic cascade wind tunnel that provide profile Mach number distributions, wake traverse data and measured suction surface boundary-layer profiles throughout the strong interaction region. Furthermore, calculated discontinuities of Mach number and flow direction across the shock system at blade passage entrance are compared with laser anemometer data. Finally, the influence of inlet Mach number and axial stream tube thickness variation on the shock-wave/boundary-layer interaction mechanism and blade performance is presented.

Shiratori et al. [47] experimentally studied the two-dimensional transonic cascade flows to investigate the behavior of passage shock waves with the shock induced boundary layer separation. The experiments are performed for an unstaggered case and a staggered case with 30° stagger angle. The time dependent stream wise shock wave positions are measured by a specially designed measuring system, of shock wave position. The results show that the self-excited shock wave oscillations occur in a range of back pressures in unstaggered and staggered cascades. The fundamental frequencies of the shock oscillation are around 400Hz 900Hz in the tested conditions. An approximately linear relation between the frequency and the mean shock wave position is observed in the unstaggered case, but is not clearly seen in the staggered case.

CHAPTER 3

COMPUTATIONAL METHOD

3.1 BASICS OF CFD

Computational fluid dynamics constitutes a new third approach in the philosophical study and development of the whole discipline of fluid dynamics. The advent of the high speed digital computer combined with the development of accurate numerical algorithms for solving physical problems on these computers has revolutionized the way we practice fluid dynamics today. Computational fluid dynamics is today an equal partner with pure theory and pure experiment in the analysis and solution of fluid dynamics problems. There is no doubt that computational fluid dynamics will continue to play this role indefinitely.

Applying the fundamental laws of mechanics to a fluid gives the governing equations for a fluid. The conservation of mass equation is

$$\rho \frac{\partial \vec{V}}{\partial t} + \nabla \cdot (\rho \vec{V}) = 0 \quad (3.1)$$

And the conservation of momentum equation is

$$\rho \frac{\partial \vec{V}}{\partial t} + \rho (\vec{V} \cdot \nabla) \vec{V} = -\nabla p + \rho \vec{g} + \nabla \cdot \tau_{ij} \quad (3.2)$$

Where, \vec{V} is the velocity vector.

These equations along with the conservation of energy equation form a set of coupled, non-linear partial differential equations. It is not possible to solve these equations analytically for most engineering problems. However, it is possible to obtain approximate computer-based solutions to the governing equations for a variety of engineering problems. This is the subject matter of Computational Fluid Dynamics (CFD).

3.2 APPLICATIONS OF CFD

CFD is useful in a wide variety of applications and here we note a few to give an idea of its use in industry.

1. CFD can be used to simulate the flow over a vehicle. For instance, it can be used to study the interaction of propellers or rotors with the aircraft fuselage.
2. The CFD analysis showed the effectiveness of a simpler manifold design without the need for field testing.
3. Bio-medical engineering is a rapidly growing field and uses CFD to study the circulatory and respiratory systems.
4. CFD is attractive to industry since it is more cost-effective than physical testing. However, one must note that complex flow simulations are challenging and error-prone and it takes a lot of engineering expertise to obtain validated solutions.

3.3 GOVERNING EQUATIONS

The flow in this study is considered to be compressible, viscous, turbulent, and unsteady. Governing equations for the present numerical simulations are the conservation of mass, conservation of momentum and the energy equations written in 2-D coordinate system (x, y). Two additional transport equations of standard k - ω turbulence model are included to model the turbulence in the flow field. The governing equation can be written in the following vector form:

$$\frac{\partial \mathbf{U}}{\partial t} + \frac{\partial \mathbf{E}}{\partial x} + \frac{\partial \mathbf{F}}{\partial y} = \frac{\partial \mathbf{R}}{\partial x} + \frac{\partial \mathbf{S}}{\partial y} + \mathbf{H} \quad (3.3)$$

Here \mathbf{U} is the conservative flux vector. \mathbf{E} and \mathbf{F} are the inviscid flux vectors and \mathbf{R} and \mathbf{S} are the viscous flux vectors in the x and y directions, respectively. \mathbf{H} is the source term corresponding to turbulence. The flux vector and the inviscid flux terms are defined by:

$$\mathbf{U} = \begin{bmatrix} \rho \\ \rho u \\ \rho v \\ E_t \\ \rho k \\ \rho \omega \end{bmatrix}, \quad \mathbf{E} = \begin{bmatrix} \rho u \\ \rho u^2 + p \\ \rho uv \\ u(E_t + p) \\ \rho uk \\ \rho u \omega \end{bmatrix}, \quad \mathbf{F} = \begin{bmatrix} \rho v \\ \rho uv \\ \rho v^2 + p \\ v(E_t + p) \\ \rho vk \\ \rho v \omega \end{bmatrix}, \quad (3.4)$$

$$\mathbf{R} = \begin{bmatrix} 0 \\ \tau_{xx} \\ \tau_{xy} \\ u\tau_{xx} + v\tau_{xy} - \left(-k \frac{\partial T}{\partial x}\right) \\ \left(\mu + \frac{\mu_t}{\sigma_k}\right) \frac{\partial k}{\partial x} \\ \left(\mu + \frac{\mu_t}{\sigma_\omega}\right) \frac{\partial \omega}{\partial x} \end{bmatrix}, \quad \mathbf{S} = \begin{bmatrix} 0 \\ \tau_{xy} \\ \tau_{yy} \\ u\tau_{xy} - v\tau_{yy} - \left(-K \frac{\partial T}{\partial y}\right) \\ \left(\mu + \frac{\mu_t}{\sigma_k}\right) \frac{\partial k}{\partial y} \\ \left(\mu + \frac{\mu_t}{\sigma_\omega}\right) \frac{\partial \omega}{\partial y} \end{bmatrix} \quad (3.5)$$

$$\mathbf{H} = \begin{bmatrix} 0 \\ 0 \\ 0 \\ 0 \\ G_k - Y_k + S_k \\ G_\omega - Y_\omega + S_\omega \end{bmatrix} \quad (3.6)$$

$$\text{Ideal gas law: } p = \rho RT \quad (3.7)$$

Here, E_t is the total energy, and it can be expressed as:

$$E_t = \rho c_p T + \frac{1}{2} \rho (u^2 + v^2) \quad (3.8)$$

In above equations, ρ is the fluid density, c_p is the specific heat, T is the temperature, u and v are the velocity components in x - and y -direction respectively. p is the pressure in the flow field. τ is the stress component and K is the thermal conductivity of the fluid. μ_t is the turbulent viscosity. Moreover, G_k is the generation of turbulence kinetic energy due to mean velocity gradients, Y_k is the dissipation of turbulence kinetic energy due to turbulence, and G_ω is the generation of ω . Y_ω is the dissipation of ω . S_k and S_ω are user defined source terms respectively. The calculation of these above terms can be found in Ref. [48].

3.4 STRATEGY OF CFD

The strategy of CFD is to replace the continuous problem domain with a discrete domain using a grid. In the continuous domain, each flow variable is defined at every point in the domain. For instance, the pressure p in the continuous 1D domain shown in the figure below would be given as

$$p = p(x), 0 \leq x < 1 \quad (3.9)$$

In the discrete domain, each flow variable is defined only at the grid points. So, in the discrete domain shown below, the pressure would be defined only at the N grid points.

$$P_i = p(x_i), i = 1, 2, \dots, N \quad (3.10)$$

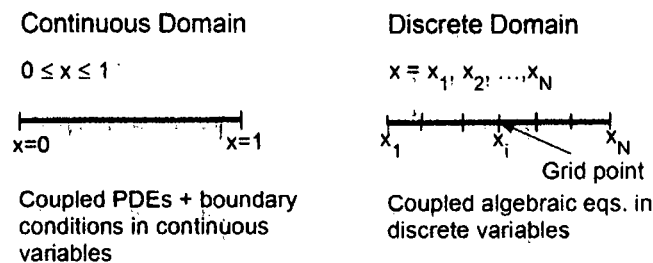


Fig. 3.1 Discretization of domain

In a CFD solution, one would directly solve for the relevant flow variables only at the grid points. The values at other locations are determined by interpolating the values at the grid points.

The governing partial differential equations and boundary conditions are defined in terms of the continuous variables such as p , V etc. One can approximate these in the discrete domain in terms of the discrete variables p_i , V_i etc. The discrete system is a large set of coupled, algebraic equations in

the discrete variables. Setting up the discrete system and solving it (which is a matrix inversion problem) involves a very large number of repetitive calculations, a task we humans palm over to the digital computer.

This method of deriving the discrete equation using Taylor's series expansions is called the finite-difference method. However, most commercial CFD codes use the finite-volume or finite-element methods which are better suited for Modeling flow past complex geometries.

3.5 DISCRETIZATION USING FINITE VOLUME METHOD

The finite volume method is a method for representing and evaluating partial differential equations in the form of algebraic equations. Similar to the finite difference method or finite element method, values are calculated at discrete places on a meshed geometry. "Finite volume" refers to the small volume surrounding each node point on a mesh. In the finite volume method, volume integrals in a partial differential equation that contain a divergence term are converted to surface integrals, using the divergence theorem. These terms are then evaluated as fluxes at the surfaces of each finite volume. Because the flux entering a given volume is identical to that leaving the adjacent volume, these methods are conservative. Another advantage of the finite volume method is that it is easily formulated to allow for unstructured meshes. The method is used in many computational fluid dynamics packages.

The integral conservation equation are written for a discrete volume,

$$\frac{\partial}{\partial x} \iiint U d\Omega + \oint_S F \cdot dS = \iiint Q d\Omega \quad (3.11)$$

and applied to control volume Ω_j , when the discretized equation associated with U_j is to be defined. This equation can be replaced by the discrete form,

$$\frac{\partial}{\partial x} (U_j \Omega_j) + \sum_{sides} (F \cdot S) = Q_j \Omega_j \quad (3.12)$$

Where, the sum of the flux terms refers to all the external sides of the control cell Ω_j . This is the general formulation of the finite volume method, and the user has to define, for a selected Ω_j , how to estimate the volume and cell face areas of the control volume Ω_j and how to approximate the fluxes at the faces.

The following constraints on the choice of the choice of the Ω_j volumes for a conservative finite volume method have to be satisfied:

1. The sum should cover the whole domain Ω ;
2. Adjacent Ω_j may overlap if each internal surface is common to two volumes;

3. Fluxes along a cell surface have to be computed by formulas independent of the cell in which they are considered.

The first term of equation (3.9) represents the time rate of change of the averaged flow variable over the selected finite volume. In absence of source terms, the finite volume formulation expresses that the variation of the average value U over the time interval Δt is equal to the sum of the fluxes exchanged between neighbouring cells. For stationary flows the numerical solution is obtained as a result of balance of all the fluxes entering the control volume. That is,

$$\sum_{sides} (F.S) = 0 \quad (3.13)$$

Physically, this equation means that the net volume flow into the control volume is zero. Here is a rectangular cell shown below.

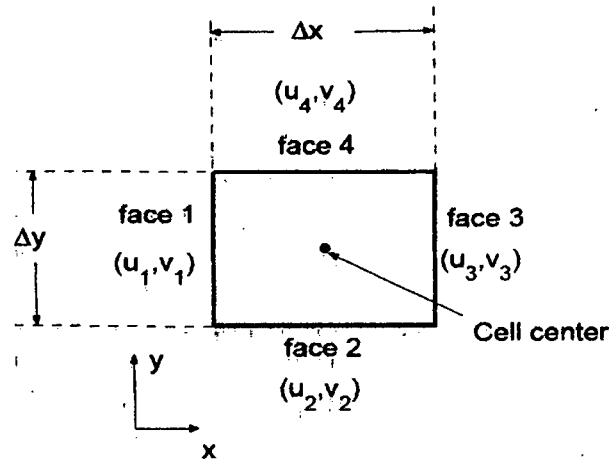


Fig. 3.2 Rectangular control volume

The velocity at face is taken to be $V_i = u_i i + v_i j$. Applying the mass conservation equation to the control volume defined by the cell gives,

$$-u_1 \Delta y - v_2 \Delta x + u_3 \Delta y + v_4 \Delta x = 0 \quad (3.14)$$

This is the discrete form of the continuity equation for the cell. It is equivalent to summing up the net mass flow into the control volume and setting it to zero. So it ensures that the net mass flow into the cell is zero i.e. that mass is conserved for the cell. Usually, though not always, the values at the cell centres are solved for directly by inverting the discrete system.

The face values u_1, v_2 , etc. are obtained by suitably interpolating the cell-center values at adjacent cells. Similarly, one can obtain discrete equations for the conservation of momentum and energy for the cell. One can readily extend these ideas to any general cell shape in 2D or 3D and any conservation equation.

The code finds solution such that mass, momentum, energy and other relevant quantities are being conserved for each cell. Also, the code directly solves for values of the flow variables at the cell centres; values at other locations are obtained by suitable interpolation.

3.6 SOLVER SETTING

CFD allows to choose one of the two numerical methods:

- a) Pressure-based solver
- b) Density-based solver

The pressure-based approach was developed for low-speed incompressible flows, while the density-based approach was mainly used for high-speed compressible flows. However, recently both methods have been extended and reformulated to solve and operate for a wide range of flow conditions beyond their traditional or original intent.

In both methods the velocity field is obtained from the momentum equations. In the density based approach, the continuity equation is used to obtain the density field while the pressure field is determined from the equation of state. On the other hand, in the pressure-based approach, the pressure field is extracted by solving a pressure or pressure correction equation which is obtained by manipulating continuity and momentum equations. Using either method, the present CFD tool will solve the governing integral equations for the conservation of mass and momentum, and for energy and other scalars such as turbulence and chemical species. In present numerical analysis density based solver is used. Detailed solver settings are shown below:

Table 3.1 Viscous model and Solver used

Viscous Model		Solver Setting	
Model	$k-\omega$ (2 equation)	Solver	Density Based
$k-\omega$ model	Standard	Space	2D
$k-\omega$ option	N/A	Gradient Option	Cell-based
Turbulent viscosity	none	Formulation	Implicit
Viscous Heating	N/A	Time	Unsteady

3.6.1 DISCRETIZATION SCHEME

For Density, Momentum, Turbulent Kinetic Energy, Specific Dissipation Rate, Energy equations have First Order Upwind, Second Order Upwind, QUICK and Third-Order MUSCL. schemes. For all cases Second Order Upwind schemes were selected. When the flow is aligned with the grid (e.g., laminar flow in a rectangular duct modelled with a quadrilateral or hexahedral grid) the first-order upwind discretization is acceptable. When the flow is not aligned with the grid (i.e., when it crosses

the grid line obliquely), however, first order convective discretization increases the numerical discretization error (numerical diffusion). For triangular and tetrahedral grids, since the flow is never aligned with the grid, generally more accurate results are obtained by using second-order discretization. For quad/hex grids, better results using the second-order discretization is obtained, especially for complex flows.

3.6.2 THE DENSITY BASED ALGORITHM

Density based solver solves the governing equations of continuity, momentum, energy and species transport simultaneously (coupled together). Governing equations for turbulence and other scalar quantities are solved afterward and sequentially. The steps for density based solver are given below:

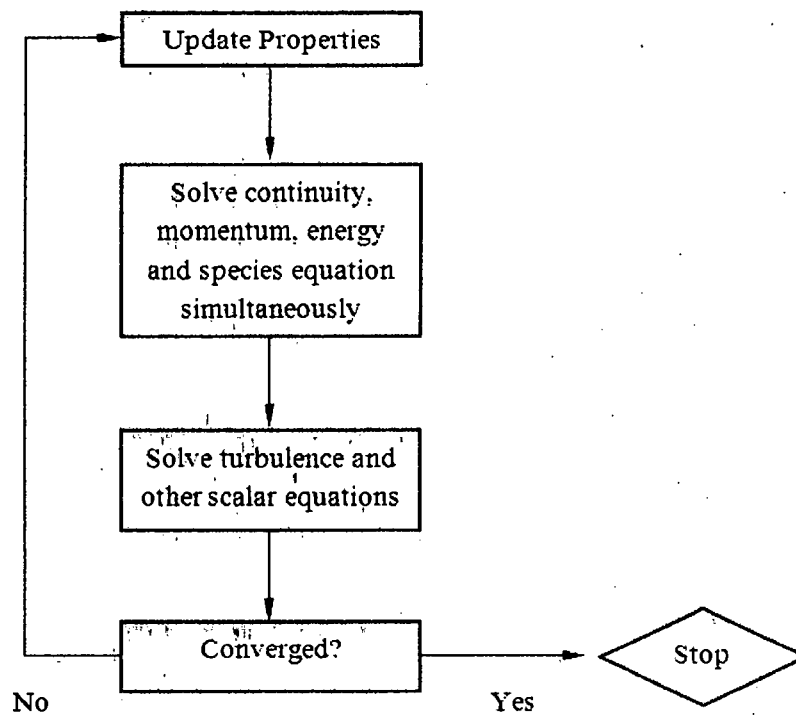


Fig 3.3 Solution procedure of density based solver

The density based coupled solver solves the turbulence equation sequentially after solving the set of equations of continuity, momentum and energy equations for each node. This density based solver can be used along with either implicit or explicit scheme. The implicit scheme forms a set of linear equations containing all the unknown parameters in all equations for every node. Here each equation consists of both unknown and existing variables. Meanwhile explicit scheme forms a set of linear equations consisting only existing variables. In the present study density based coupled solver has been implied with implicit scheme.

3.7 TURBULENCE MODELING

Turbulent flows are characterized by fluctuating velocity fields. These fluctuations mix transported quantities such as momentum, energy and species concentration and cause the transported quantities to fluctuate as well. This approach is referred to as Direct Numerical Simulation (DNS). Another approach is large eddy simulation (LES), where large scale structure in the flow is directly simulated where as small scales are filtered out. Due to large computational time and computational research requirements for DNS and to some extent, for LES, these techniques are more or less for research-oriented applications. Since these fluctuations can be of small scale and high frequency, they are too computationally expensive to simulate directly in practical engineering calculations. So, over the last several decades approximate procedures have been developed which allows us to solve turbulent flow fields. The scheme is based on averaging of the fluid properties whereby the high frequency (small scale) fluctuations are removed. These fluctuating terms are then related to the mean flow properties by relations, which are known as turbulence models.

Instead, the instantaneous (exact) governing equations can be time-averaged, ensemble-averaged, or otherwise manipulated to remove the small scales, resulting in a modified set of equations that are computationally less expensive to solve. However, the modified equations contain additional unknown variables and turbulence models are needed to determine these variables in terms of known quantities.

A turbulence model is a semi-empirical equation relating the fluctuating correlation to mean flow variables with various constants provided from experimental investigations. These models are developed based on experimental data obtained from relatively simple flows under controlled environment. That in turn limits the range of applicability of turbulence models. When this equation is expressed as an algebraic equation, it is referred to as the zero-equation model. When partial differential equations are used, they are referred to as one-equation or two equation models, depending on the number of PDEs used. Some models employ ordinary differential equations, in which case they are referred to as half-equation models. Finally, it is possible to write a partial differential equation directly for each of the turbulence correlations in which case they compose a system of PDEs known as the Reynolds stress equations.

A number of turbulence models are there to match the conditions like

1. Spalart-Allmaras model
2. k - ϵ model
3. k - ω model
4. v^2 - f model
5. Reynolds Stress model (RSM)

6. Detached Eddy Simulation (DES) model

7. Large Eddy Simulation (LES) model

3.7.1 k - ω two equations Turbulence Model

Convection of turbulence is not modelled in zero-equation models. Therefore the physical effect of past history of the flow is not included in simple algebraic models. In order to account for this physical effect, a transport equation based on Navier-Stokes equation may be derived. When one such equation is employed, it is referred to as a one-equation model. When two transport equations are used, it is known as a two-equation model.

Two different models are there for k - ω model. They are

1. Standard

2. Shear Stress Transport (SST)

3.7.1.1 Standard k - ω Model

This two equation model includes one equation for the turbulent kinetic energy (k), as developed previously and a second equation for the specific turbulent dissipation rate (ω). The standard k - ω model is an empirical model based on model transport equations for the turbulence kinetic energy (k) and the specific dissipation rate (ω), which can also be thought of as the ratio of ϵ to k .

As the k - ω model has been modified over the years, production terms have been added to both the k and ω equations, which have improved the accuracy of the model for predicting free shear flows.

The turbulence kinetic energy, k , and the specific dissipation rate, ω , are obtained from the following transport equations:

$$\frac{\partial}{\partial t}(\rho k) + \frac{\partial}{\partial x_i}(\rho k u_i) = \frac{\partial}{\partial x_j}(\Gamma_k \frac{\partial k}{\partial x_j}) + G_k - Y_k + S_k \quad (3.15)$$

$$\frac{\partial}{\partial t}(\rho \omega) + \frac{\partial}{\partial x_i}(\rho \omega u_i) = \frac{\partial}{\partial x_j}(\Gamma_\omega \frac{\partial \omega}{\partial x_j}) + G_\omega - Y_\omega + S_\omega \quad (3.16)$$

In these equations, G_k represents the generation of turbulence kinetic energy due to mean velocity gradients. G_ω represents the generation of ω . Γ_k and Γ_ω represent the effective diffusivity of k and ω , respectively. Y_k and Y_ω represent the dissipation of k and ω due to turbulence. All of the above terms are calculated as described below. S_k and S_ω are user-defined source terms.

3.8 TURBULENCE INTENSITY

The turbulence intensity, also referred as turbulence level, is defined as:

$$I \equiv \frac{u'}{U} \quad (3.17)$$

Where u' is the root-mean-square of the turbulent velocity fluctuations and U is the mean velocity (Reynolds averaged).

If the turbulent energy (k) is known u' can be computed as:

$$u' \equiv \sqrt{\frac{1}{3}(u_x'^2 + u_y'^2 + u_z'^2)} \quad (3.18)$$

U can be computed from the three mean velocity components U_x, U_y and U_z as:

$$U \equiv \sqrt{(U_x^2 + U_y^2 + U_z^2)} \quad (3.19)$$

When setting boundary conditions for a CFD simulation it is often necessary to estimate the turbulence intensity at the inlet. To do this accurately it is good to have some form of measurements or previous experience to estimate. Here are a few examples of common estimations of the incoming turbulence intensity:

(a) High-turbulence cases: These cases include high-speed flow inside complex geometries like heat-exchangers and flow inside rotating Machinery (Turbines and Compressors). Typically the turbulence intensity is between 5% and 20%.

(b) Medium-turbulence case: These cases include flow in not-so-complex devices like large pipes, ventilation flows or low speed flows (low Reynolds number). Typically the turbulence intensity is in between 1% to 5%.

(c) Low-turbulence case: These cases include flow originating from a fluid that stands still, like external flow across cars, submarines and aircrafts. Very high-quality wind-tunnels can also reach really low turbulence levels. Typically the turbulence intensity is very low, well below 1%.

3.9 OPERATING CONDITION

Operating pressure is significant for incompressible ideal gas flows because it directly determines the density. Operating pressure is less significant for compressible flows. The pressure changes in

such flows are much larger than those in incompressible flows, so there is no real problem with round off error and there is therefore no real need to use gauge pressure. In fact, it is common convention to use absolute pressures in such calculations. Operating pressure has been set to zero making gauge and absolute pressures equivalent.

3.10 BOUNDARY CONDITION

Gauge pressure of 101325Pa has been selected which is recommended for reasonable accuracy. The temperature has been set at 300k. The back pressure has been set at 75993.75 Pa. Stagger angle has been varied as an indication for different flow cases. The whole study has been done for zero angle of attack.

A detailed overview of boundary condition is given below:

Table 3.2 Boundary conditions

Type	Inlet	Outlet	Wall
Gauge Pressure(Pa)	101325	75993.75	No slip condition
Temperature(K)	300	300	
Initial Gauge Pressure (Pa)	100000	---	
Direction Specification Method	Normal to Boundary	Normal to Boundary	
Turbulence Specification Method	Intensity and Viscosity Ratio	Intensity and Viscosity Ratio	
Turbulence intensity	5%	5%	
Turbulence Viscosity Ratio	5	5	

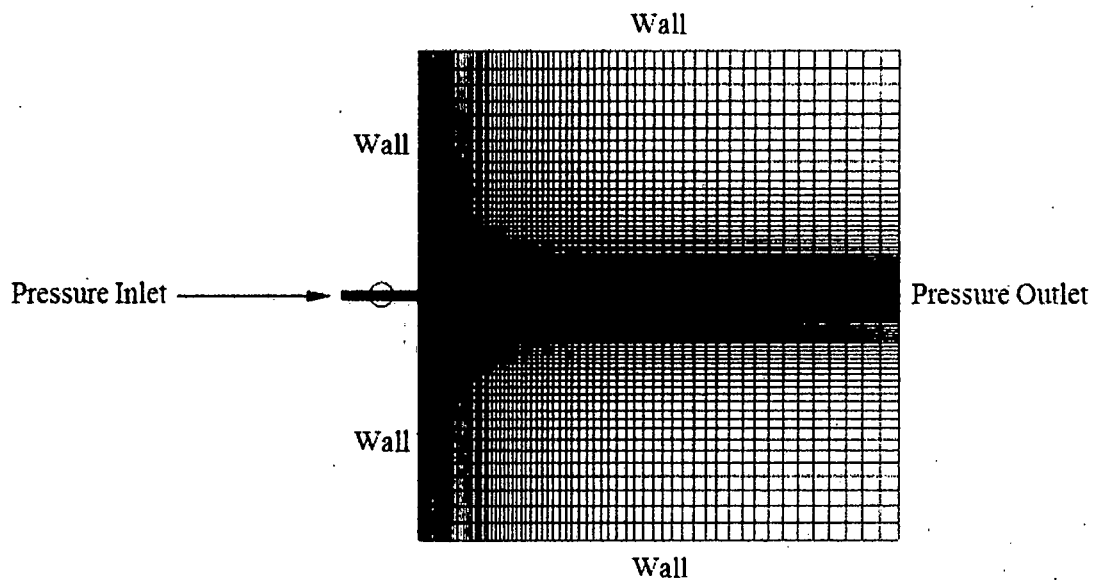


Figure. 3.4 Domain Boundaries

3.11 Courant Number

For ANSYS Fluent's density-based solver, the main control over the time-stepping scheme is the Courant number (CFL). The time step is proportional to the CFL number by the equation,

$$\Delta t = \frac{2CFLV}{\sum_f \lambda_f^{max} A_f} \quad (3.20)$$

Where, V is the cell volume, A_f is the face cell, and λ_f^{max} is the maximum of some local eigenvalues. Linear stability theory determines a range of permissible values for the CFL (that is, the range of values for which a given numerical scheme will remain stable). When one specifies a permissible CFL value, ANSYS Fluent computes an appropriate time step using the equation. In general, taking larger time steps leads to faster convergence, so it is advantageous to set the CFL as large as possible (within the permissible range). The stability limits of the density-based implicit and explicit formulations are significantly different. The explicit formulation has a more limited range and requires lower CFL settings than does the density based implicit formulation. Appropriate choices of CFL for only the density base solver are discussed below.

3.11.1 Courant Numbers for the Density-Based Implicit Formulation

Linear stability theory shows that the density-based implicit formulation is unconditionally stable. However, as with the explicit formulation, nonlinearities in the governing equations will often limit stability. The default CFL for the density-based implicit formulation is 5.0. It is often possible to increase the CFL to 10, 20, 100, or even higher, depending on the complexity of the problem. One may find that a lower CFL is required during start up (when changes in the solution are highly nonlinear), but it can be increased as the solution progresses. The coupled AMG solver has the capability to detect divergence of the multi-grid cycles within a given iteration. If this happens, it will automatically reduce the CFL and perform the iteration again, and a message will be printed to the screen. CFL value 0.9 has been used in this study.

3.12 Material Selection

Fluid material is air, which is the working fluid in this problem. Here compressibility and variations of the thermo physical properties have been made dependent on temperature. Ideal gas law and intermolecular-force potential Sutherland's law have been set for density and viscosity. While Density and Viscosity have been made temperature dependent, specific heat (c_p) and Thermal Conductivity have been left constant. For compressible flows, thermal dependency of the physical properties is generally recommended. For simplicity, Thermal Conductivity and specific heat (c_p) are assumed to be constant.

3.12.1 Sutherland's Law

In 1893 William Sutherland, an Australian physicist, published a relationship between the dynamic viscosity, μ , and the absolute temperature, T , of an ideal gas. This formula, often called Sutherland's law, is based on kinetic theory of ideal gases and an idealized intermolecular-force potential. Sutherland's law is still commonly used and most often gives fairly accurate results with an error less than a few percent over a wide range of temperatures.

Sutherland's three coefficient law has the form:

$$\mu = \mu_0 \left(\frac{T}{T_0} \right)^{3/2} \frac{T_0 + S}{T + S} \quad (3.21)$$

Where,

μ is the viscosity in kg/m-s

T is the static temperature in K

T_0 is a reference temperature in K

μ_0 is the viscosity at the reference temperature in kg/m-s

S is the effective temperature in K (Sutherland constant)

Table 3.3 Constants in Sutherland's law

Gas	$\mu_0 \left(\frac{kg}{ms} \right)$	$T_0 (K)$	$S (K)$
Air	1.716×10^{-5}	273.11	110.56

3.13 STEADY ANALYSIS

First a steady computation has been performed using steady solver. The steady computation has been done to develop the flow field for further unsteady study. The steady computation was performed until the flow field was fully developed. This computation is done as steady solver requires less time than the unsteady solver.

3.14 Unsteady Analysis

The solution obtained from steady solver is used for unsteady case as a reference. Second order implicit formulation has been used for unsteady cases with fixed time stepping method. Time step size has been chosen 10^{-6} sec with 20 iterations per time step.

During the computation the local pressure on the airfoil surface was documented. Total 61 points were monitored to gather the pressure history. Eighteen points were chosen on the mid-airfoil upper surface, eighteen points on the mid-airfoil lower surface, ten points on the upper airfoil lower surface, ten points on the lower airfoil upper surface and five points on the wake.

3.15 DISCRETIZATION OF THE DOMAIN

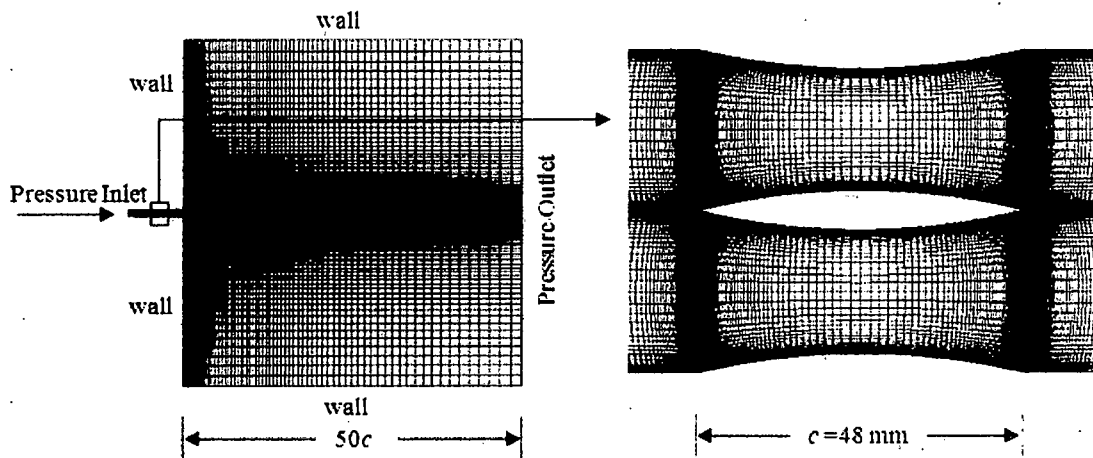


Figure. 3.5 Computational Domain

1. Three airfoils have been used in this study to form the airfoil cascade. For simplicity only four surfaces have been considered. The airfoils are Bi-convex circular arc with 12% thickness. Length of the chord c is 0.048 m. Leading Edge (LE) is at $(0,0)$ and Trailing Edge (TE) is at $(c,0)$ in the coordinate system.
2. The inlet is at $5c$ distance left from leading edge. The tunnel dimension is equal to the chord length (c). The tunnel is extended up to $2c$ distance right from the trailing edge. The outlet is at $50c$ distance beyond the end of the tunnel. The outlet tunnel dimension is $51c$ and spread evenly on the both side of the airfoil axis.
3. The matter of grid generation is a significant consideration in CFD. The generation of an appropriate grid or mesh is one thing, the solution of the governing flow equations over such a grid is quite another thing. Quadrilateral cells were used for this simple geometry because they can be stretched easily to account for different flow gradients in different directions. 200 points have been taken on each surface of the airfoil. Consequently, the cells near the surface have high aspect ratios. For viscous flow over the airfoil, finely spaced grid was constructed to calculate the details of the flow near the airfoil.

CHAPTER 4

COMPUTATIONAL RESULTS

4.1 VALIDATION OF NUMERICAL MODEL

The numerical code is validated with the experimental results. At the beginning of this thesis work, supersonic wind tunnel facility was not available in our Lab. So we used the available experimental flow structures for 15% thick circular arc isolated airfoil [12]. A numerical model is made, simulation is first carried out with the same airfoil (15% thick) for verification of numerical schemes. Figure. 4.1(a) shows the Schlieren image obtained from the experiments of Hasan et al. [12] for $PR = 0.70$. The same flow case corresponds to $PR = 0.69$ where PR is the pressure ratio i.e., ratio of the outlet pressure to inlet pressure in the present study.

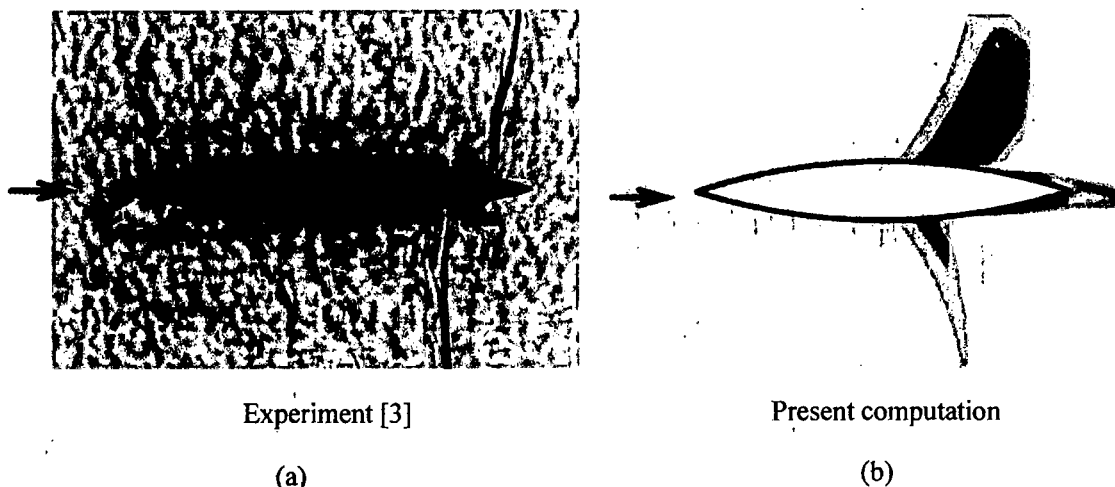


Figure. 4.1 Instantaneous flow field with shock waves. (a) Experimental Schlieren photograph [12] for $PR = 0.70$ and (b) Mach contour from present computation for $PR = 0.69$ (15% thick airfoil).

Figure. 4.1 shows the qualitative comparison of the numerical code used. The numerically obtained flow field with shock waves is shown in figure. 4.1(b). It is found that the flow structures are almost similar with two shock waves, one on the upper and another on the lower surfaces of the airfoil. The shock on upper surface is closer to trailing edge than the shock on the lower surface. So the computed flow field is almost identical with the experimental results except the locations of the shock waves. Later the same numerical model is used for 12% thick circular arc airfoil cascade.

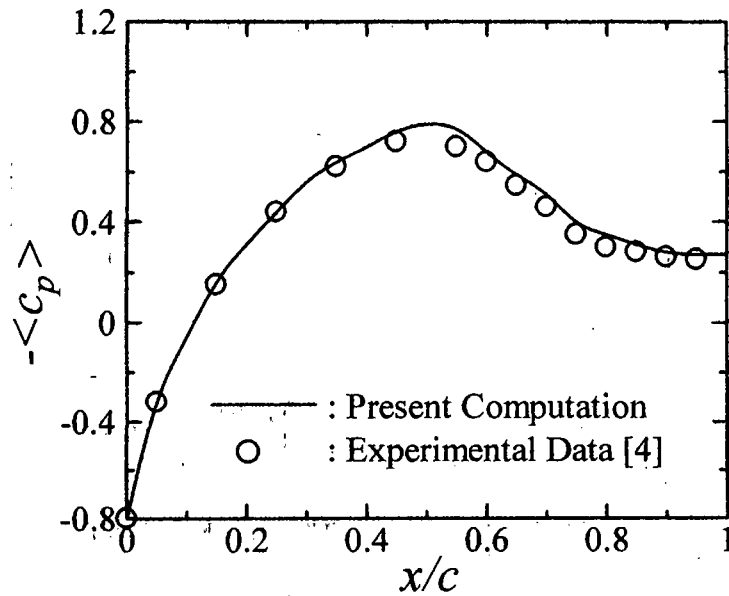
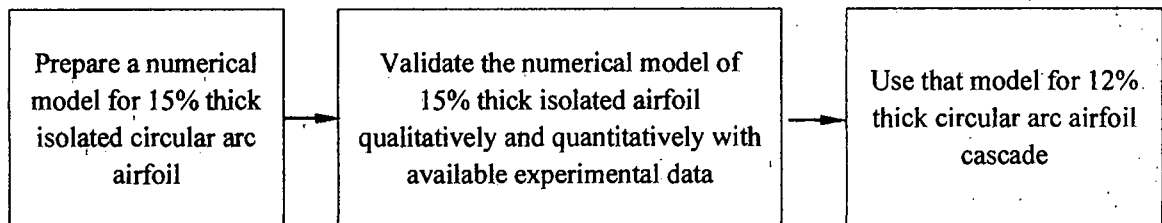


Figure. 4.2 Distribution of time averaged pressure coefficient; Experimental data from [1]

For quantitative comparison time averaged pressure coefficient is considered and shown in figure. 4.2. In figure. 4.2 the solid line represents the computational results for 15% thick isolated circular arc airfoil and open circle symbol represents experimental results of McDevitt et al. [1]. The figure shows that for most of the flow field the computational results are almost same with the experimental data. The computational results slightly over predict the value of c_p in the shock position and the region of the intense shock boundary layer interaction.

The differences in shock structure and pressure coefficient are obviously due to the complexities in real flows, the main flow non-uniformity and the sidewall boundary layers, which are never taken into account in present 2D numerical computation.

Validation steps:



4.2 Flow field contour behavior

Internal flow passing through an airfoil cascade is studied numerically for different stagger angle. The stagger angle is defined as the angle between the cascade axial line and chord line (the line connecting the leading and trailing edges of the blade). Bi-convex circular airfoil cascade consisting of three blades is used in this study. Blade thickness is 12% of the chord length. Blades are placed at $0.5c$ distance apart from each other. Angle of attack is 0° . Cascade inlet and exit pressure are kept at 101325Pa and 75993.75Pa to maintain a Pressure Ratio (PR) of 0.75. The Mach number at c distance ahead of the leading edge of the mid-airfoil is considered as the free stream Mach number (M_∞). For any fixed stagger angle, as the air moves forward ($-5c$ to $-c$) free stream Mach number slightly increases. With the increase in stagger angle, Mach number is slightly decreased along the chord line of the mid-airfoil from $-5c$ to $-c$ as shown in the figure. 4.3.

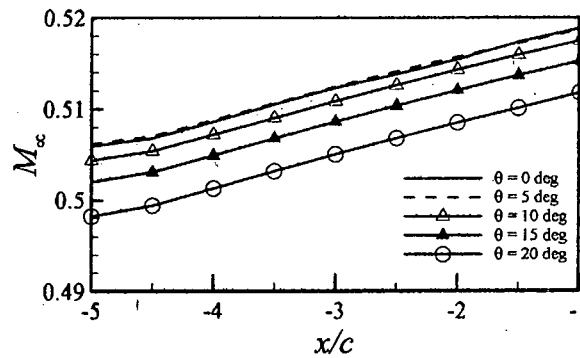


Figure. 4.3 Variation of free stream Mach number along the chord line of the mid-airfoil from $-5c$ to $-c$ for different stagger angle

To understand the transonic flow phenomena in the cascade a Reynolds Averaged Navier-Stokes (RANS) solver is used. Pressure data is collected on the four different surfaces and at the wake. Four surfaces are mid-airfoil upper surface, mid-airfoil lower surface, upper airfoil lower surface and lower airfoil upper surface. Fig. 4.4 shows pressure variation with respect to time at $x/c=0.71$ on the mid-airfoil upper surface for $\theta=0^\circ$. It is observed that the pressure distribution is uniform unsteady. Pressure fluctuates in a cyclic fashion. The frequency of the cycle f is 976Hz and the time period T is 1.024ms. The enlarged view of the pressure distribution is shown for two cycles on the right side figure. To analyze the flow, one complete cycle is divided into 8 equal divisions. In these 8 divisions there are nine time steps as shown in the figure with the letters a, b, c, d, e, f, g, h and i. In numerical solution time step size is $1\mu s$ and here cycle time period is 1.024ms. So, 1024 iterations are required to collect data of the one whole cycle. Since the cycle is divided into 8 equal divisions, therefore to collect data at each time steps data files were saved after 128 iterations.

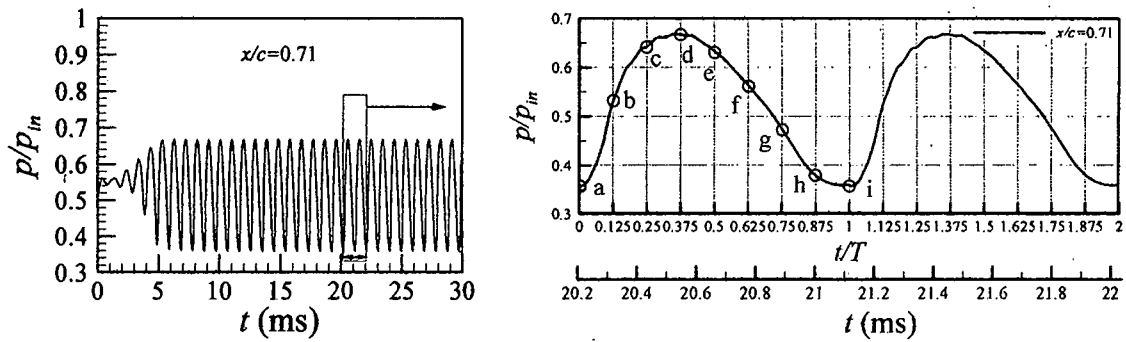


Figure. 4.4 Pressure vs. time distribution ($\theta=0^\circ$)

To understand the transonic flow phenomena in the cascade a Reynolds Averaged Navier-Stokes (RANS) solver is used. Pressure data is collected on the four different surfaces and at the wake. Four surfaces are mid-airfoil upper surface, mid-airfoil lower surface, upper airfoil lower surface and lower airfoil upper surface. Figure. 4.4 shows pressure variation with respect to time at $x/c=0.71$ on the mid-airfoil upper surface for $\theta=0^\circ$. It is observed that the pressure distribution is uniform unsteady. Cyclic pressure fluctuation is seen on the airfoil surface. The frequency of the cycle f is 976Hz and the time period T is 1.024ms. The enlarged view of the pressure distribution is shown for two cycles on the right side figure. To analyze the flow, one complete cycle is divided into 8 equal divisions. In these 8 divisions there are nine time steps as shown in the figure with the letters a, b, c, d, e, f, g, h and i. In numerical solution time step size is $1\mu\text{s}$ and here cycle time period is 1.024ms. So, 1024 iterations are required to collect data of the one whole cycle. Since the cycle is divided into 8 equal divisions, therefore to collect data at each time steps, data files were saved after 128 iterations.

Figures 4.3 to 4.7 represent the numerically obtained Mach contours with shock waves in the flow field. From figures it is observed that in the flow field there are two shock waves, one on the mid-airfoil upper surface and the other on the mid-airfoil lower surface. The images clearly reveal the presence of normal shock wave over the airfoil surfaces and their oscillation with time.

In figure. 4.5 Mach contour is shown for $\theta=0^\circ$. Shock wave is present here and shock wave oscillates with time. At $t/T=0$, shock wave is seen on the mid-airfoil upper surface at $x/c=0.73$ (nearest to TE) and on the mid-airfoil lower surface at $x/c=0.56$ (distant from TE). In the next time step, at $t/T=1/8$ on the mid-airfoil upper surface the shock wave moves upstream ($x/c=0.69$) and gain strength. On the mid-airfoil lower surface shock wave is disappeared. At $t/T=2/8$ on the mid-airfoil upper surface shock wave is seen at $x/c=0.65$ and its strength gradually decreases. On the mid-airfoil lower surface there is no shock. At $t/T=3/8$ shock wave is found at $x/c=0.58$ on the mid-airfoil upper surface (still moving upstream) and with lower strength. On the mid-airfoil lower surface still there

is no shock. At $t/T=4/8$ on the mid-airfoil upper surface shock is present at $x/c=0.56$ (distant from TE) and on the mid-airfoil lower surface shock wave is again observed at $x/c=0.73$ (nearest to TE) with moderate strength. So, at this time step the shock wave is present both on the mid-airfoil upper surface and lower surface. After that at $t/T=5/8$ shock wave disappears from the mid-airfoil upper surface. On the mid-airfoil lower surface shock wave is found at $x/c=0.69$ with maximum strength. In the next step, at $t/T=6/8$ shock wave is not found on the mid-airfoil upper surface. On mid-airfoil lower surface shock wave moves upstream ($x/c=0.65$) and its strength gradually decreases. At $t/T=7/8$ there is no shock on the mid-airfoil upper surface. On the mid-airfoil lower surface shock wave is seen at $x/c=0.58$ (still moves upstream). After this time step, the cycle starts again and repeats in the similar way.

This type of shock oscillation is known as Type-B shock (interrupted shock wave motion). It is characterized by the disappearance of the shock wave in the dynamic case during a part of its backward motion. On its way in upstream direction the shock wave reaches its maximum strength as can be noticed clearly from size of the shock waves in the successive pictures of figure 4.3. Figure 4.4, 4.5, 4.6 and 4.7 represents the flow field mach contour for stagger angle $\theta=5^\circ, 10^\circ, 15^\circ$ and 20° respectively. In each case, Type-B shock wave oscillation is observed.

In case of $\theta=0^\circ$, on the mid-airfoil upper surface shock moves from $x/c=0.73$ to 0.56 and on the mid-airfoil lower surface shock moves from $x/c=0.73$ to 0.56 (same as mid-airfoil upper surface). When the shock is at $x/c=0.73$ on the mid-airfoil upper surface, shock on the mid-airfoil lower surface is at $x/c=0.56$. As the shock on the mid-airfoil upper surface starts to move upstream, on the lower surface shock disappears. After that when on the mid-airfoil upper surface shock reaches at $x/c=0.56$, shock again appears on the mid-airfoil lower surface at $x/c=0.73$. Similarly, as on the mid-airfoil lower surface shock starts to move upstream, on the mid-airfoil lower surface shock disappears.

For $\theta=5^\circ$, on the mid-airfoil upper surface shock moves from $x/c=0.742$ to 0.53 and on the mid-airfoil lower surface the shock moves from $x/c=0.709$ to 0.53 as shown in figure. 4.6. In this case shock movement increases both on the mid-airfoil upper and mid-airfoil lower surface as compared with $\theta=0^\circ$. At $t/T=0$, shock is present both on the mid-airfoil upper ($x/c=0.742$) and mid-airfoil lower surface ($x/c=0.56$). In the next time step, both on the mid-airfoil upper and lower surface shock wave moves upstream. Then the shock vanishes on the mid-airfoil lower surface but on the mid-airfoil upper surface shock still moves upstream which reaches to $x/c=0.53$ at $t/T=0.50$. On the mid-airfoil upper surface there is no shock at $t/T=0.625$ at that time shock is seen on the mid-airfoil lower surface at $x/c=0.709$. On mid-airfoil lower surface up to $t/T=1$ shock wave moves towards upstream. At $t/T=1$ shock re-arises on the mid-airfoil upper surface.

For $\theta=10^\circ$ at $t/T=0$, shock is located at $x/c=0.742$ and 0.556 respectively on the mid-airfoil upper and mid-airfoil lower surface (figure. 4.7). In the next time step, shock moves down stream ($x/c=0.784$) on the mid-airfoil upper surface and shock moves upstream ($x/c=0.53$) on the mid-

airfoil lower surface. Then, the shock on both the mid-airfoil upper and mid-airfoil lower surface moves upstream. On mid-airfoil lower surface shock vanishes after $t/T=0.25$, while shock on the mid-airfoil upper surface still maintain its upstream movement. Shock on the mid-airfoil upper surface gradually moves upstream and at $t/T=0.625$ it reaches $x/c=0.582$. At this time shock is again seen on the mid-airfoil lower surface at $x/c=0.69$ and it gradually moves upstream. At $\theta=10^\circ$, shock movement on the mid-airfoil upper surface is observed from $x/c=0.784$ to 0.582 and on the mid-airfoil lower surface the shock moves from $x/c=0.69$ to 0.50 .

For $\theta=15^\circ$, at the beginning of the cycle shock wave is seen at $x/c=0.771$ on the mid-airfoil upper surface and at $x/c=0.53$ on the mid-airfoil lower surface (figure. 4.8). In the next time steps, on the mid-airfoil upper surface shock wave gradually moves towards upstream and vanishes after $t/T=0.5$ ($x/c=0.629$). On the mid-airfoil lower surface shock wave moves from $x/c=0.53$ to 0.50 , after that shock vanishes. At $t/T=0.625$ shock is reappeared on the mid-airfoil lower surface ($x/c=0.651$) and gradually moves upstream.

For $\theta=20^\circ$, $t/T=0$ to 0.125 shock moves down stream ($x/c=0.771$ to 0.784) on mid-airfoil upper surface and on mid-airfoil lower surface shock is found at the same location ($x/c=0.50$) as shown in figure. 4.9. Then shock on the mid-airfoil upper surface gradually moves upstream and vanishes after $t/T=0.5$ ($x/c=0.651$). On the mid-airfoil lower surface shock vanishes after $t/T=0.125$ ($x/c=0.5$) and again seen at $t/T=0.625$ at $x/c=0.629$. From $x/c=0.629$ shock on mid-airfoil lower surface gradually moves upstream.

At $\theta=0^\circ$, shock movement on the mid-airfoil upper surface is $0.17c$. Shock movement on the mid-airfoil upper surface increases from $0.17c$ to $0.212c$ with the increase in stagger angle (θ) from 0 to 5 , further increase in stagger angle results a decrease in shock wave movement on this surface. At stagger angle 10° , 15° , 20° shock movement on mid-airfoil upper surface is $0.202c$, $0.142c$, $0.133c$ respectively.

At 0° shock movement on the mid-airfoil lower surface is equal to upper surface. With the increase in stagger angle shock movement initially increases and further increase in stagger angle shock movement decreases. At 5° and 10° shock movement on the mid-airfoil lower surface is $0.179c$ and $0.19c$ respectively. At 15° and 20° on the mid-airfoil lower surface shock movement is $0.151c$ and $0.129c$ respectively.

So, with the increase in stagger angle on the mid-airfoil upper surface shock wave start and end point moves down stream and on the mid-airfoil lower surface shock wave start and end point moves up stream.

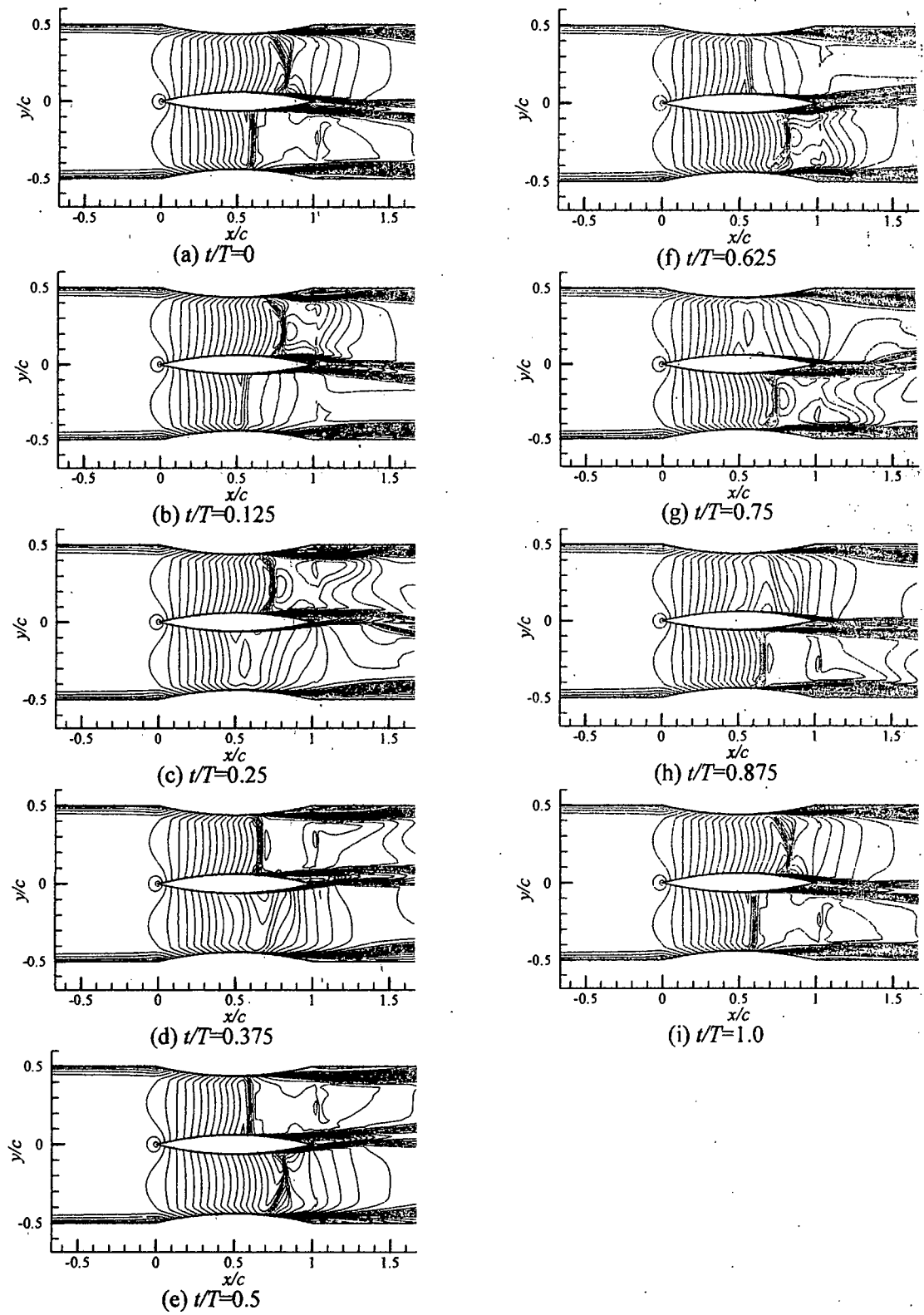


Figure. 4.5 Mach Contour for stagger angle $\theta=0^\circ$

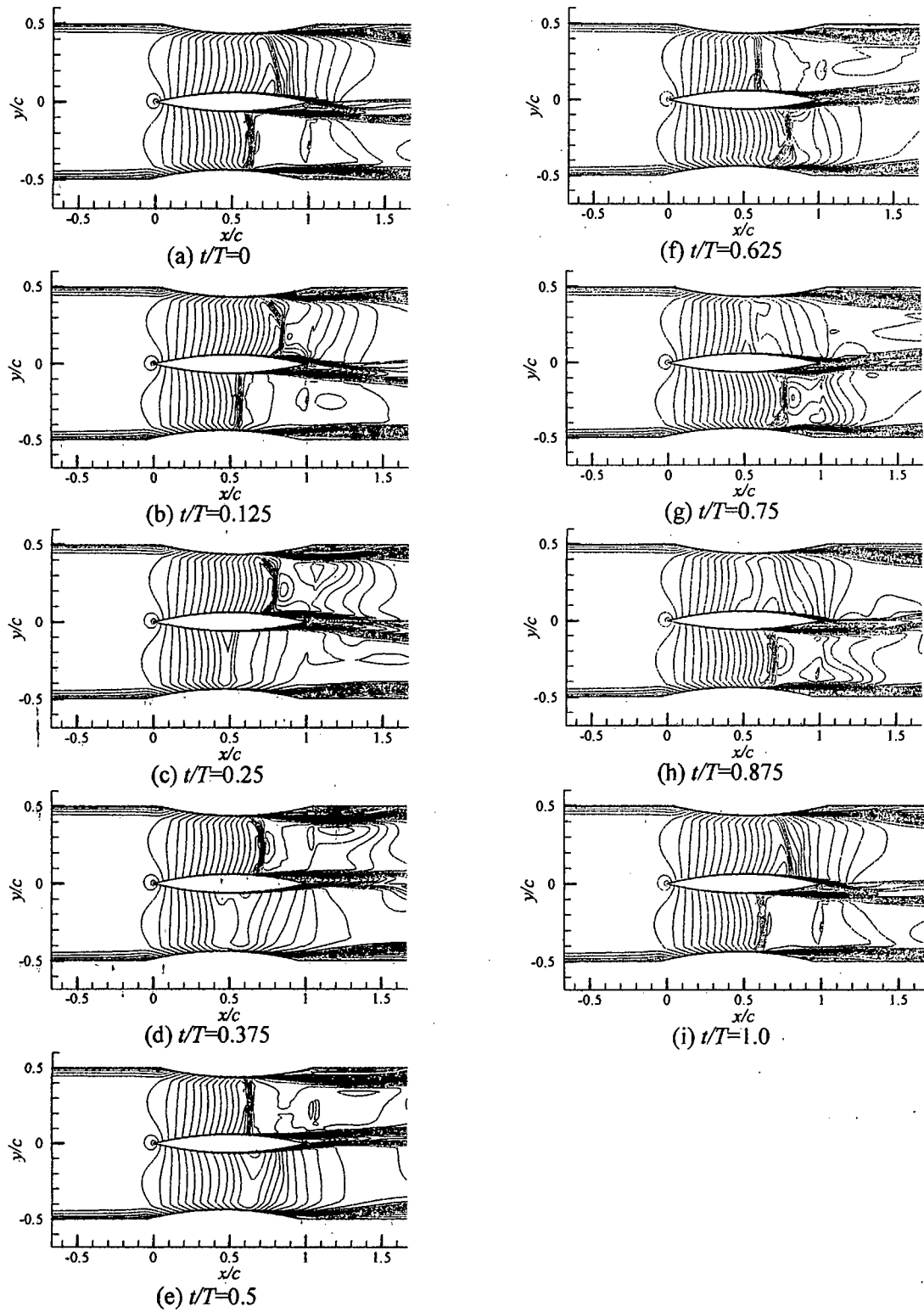


Figure 4.6 Mach contour for stagger angle $\theta=5^\circ$

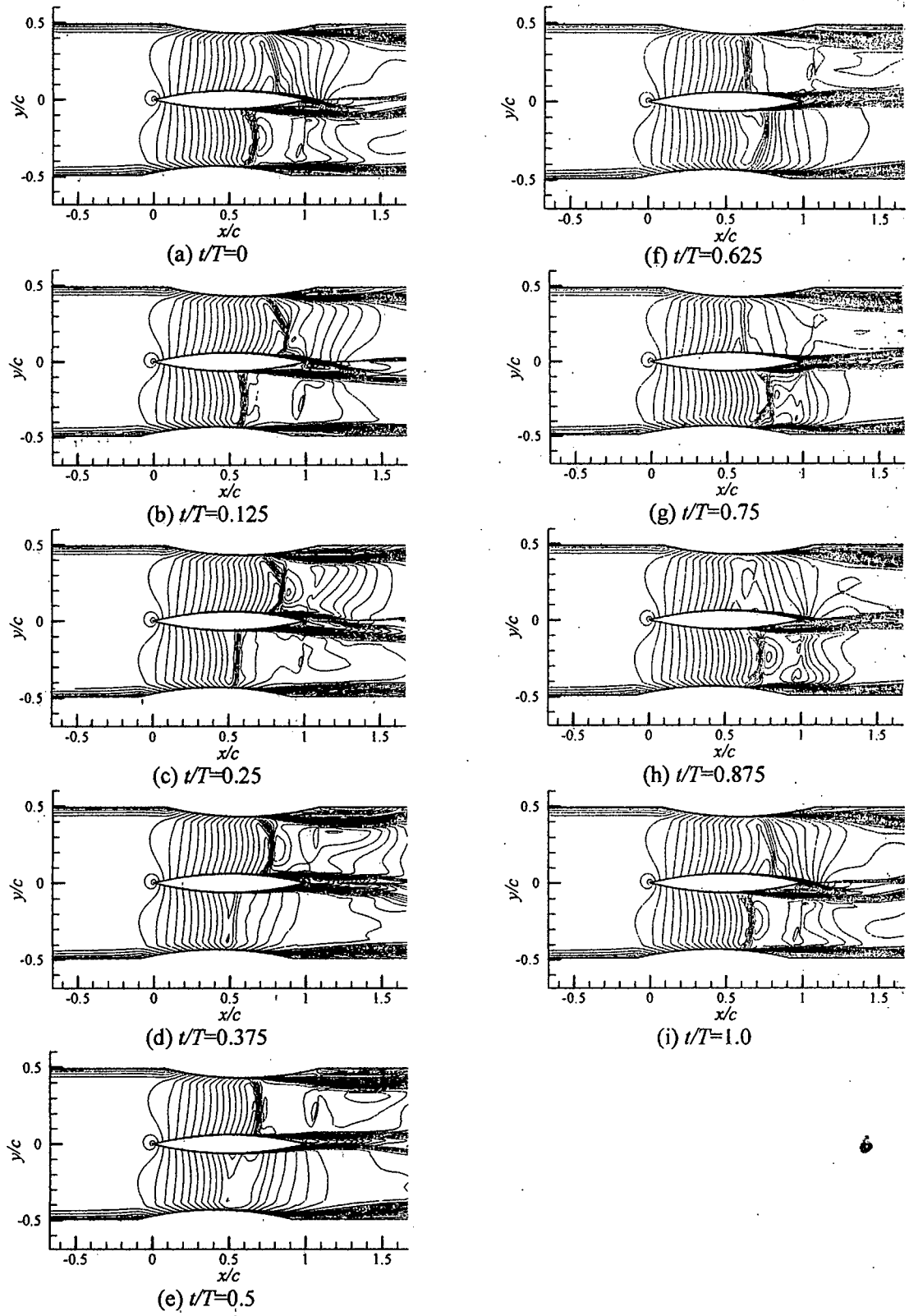


Figure 4.7 Mach contour for stagger angle $\theta=10^\circ$

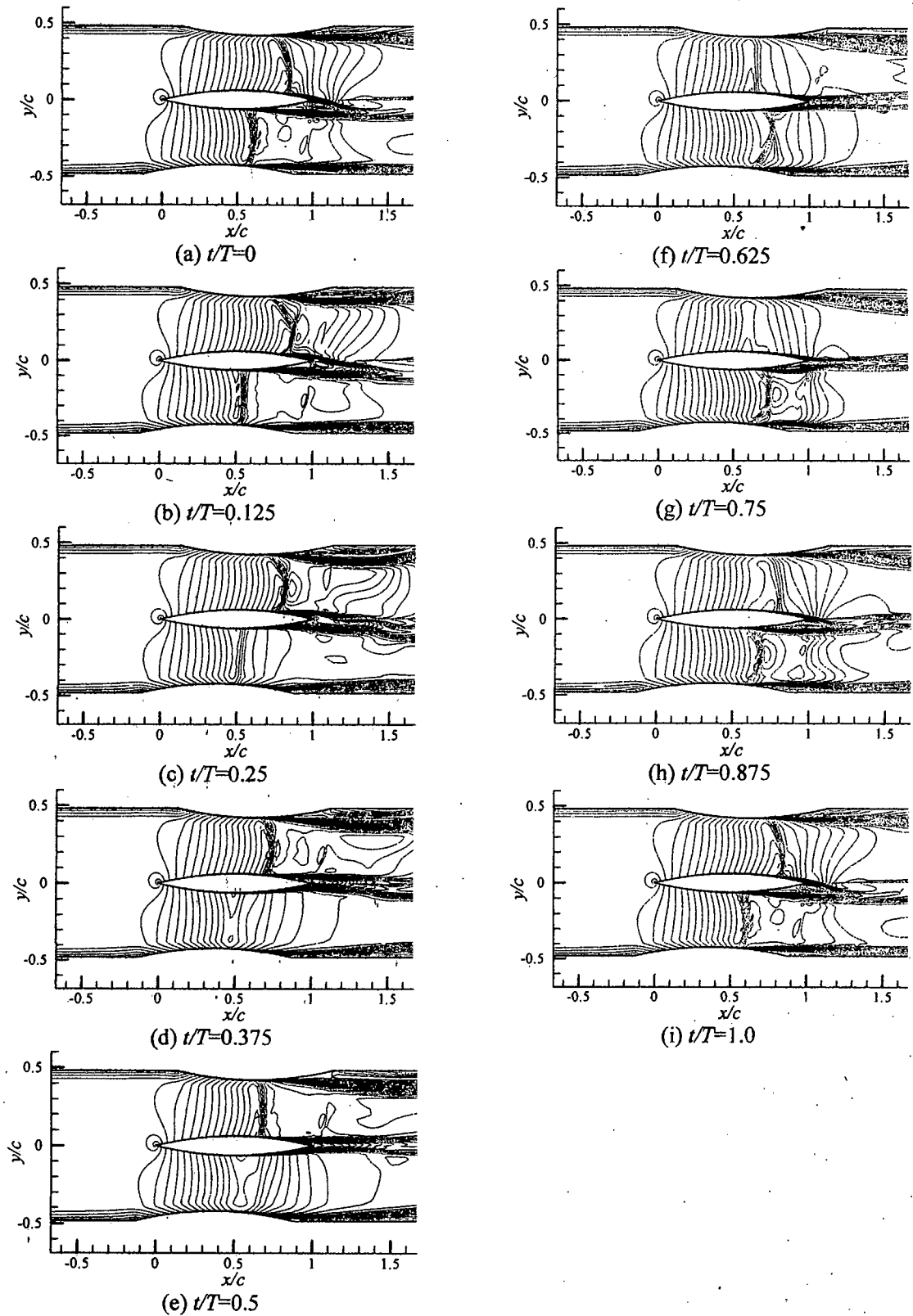


Figure 4.8 Mach contour for stagger angle $\theta=15^\circ$

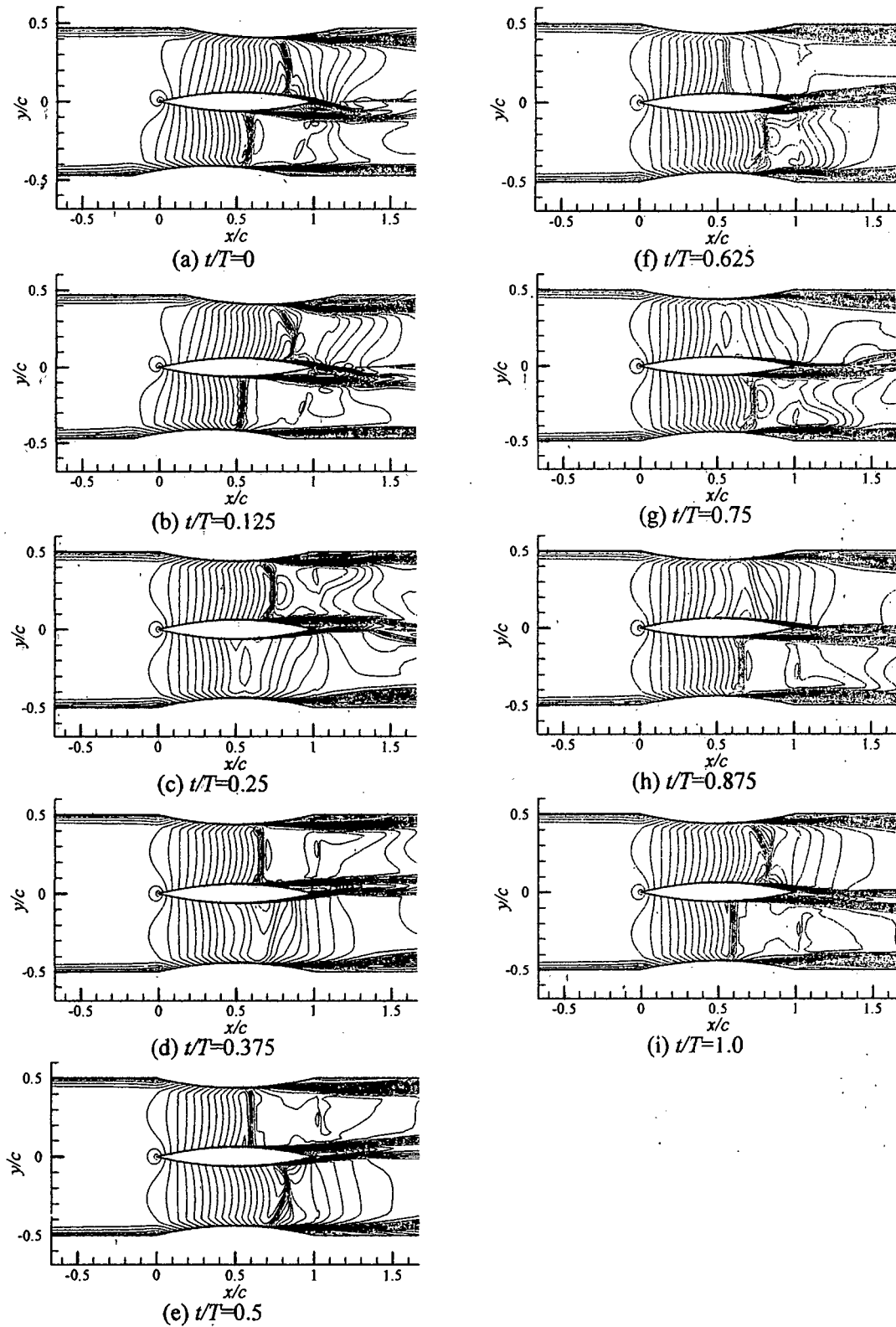


Figure. 4.9 Mach contour for stagger angle $\theta=20^\circ$

4.3 c_p distribution

The aerodynamic performance of airfoil cascade can be studied by reference to the distribution of pressure over the airfoil. This distribution is usually expressed in terms of the pressure coefficient (c_p).

$$c_p = \frac{p(x) - p_\infty}{\left(\frac{1}{2}\right)\rho_\infty v_\infty^2} \quad (4.1)$$

c_p by definition states the difference between local static pressure and free stream static pressure, non-dimensionalized by the free stream dynamic pressure. The shock wave oscillation and its interaction with boundary layer results this difference in pressure in the airfoil surface. In figure. 4.10 c_p distributions have been shown with respect to x/c , where x/c varies from 0 at the leading edge to 1.0 at the trailing edge. Here, c_p distribution has been depicted at nine different time steps in a cycle at two different surfaces (mid-airfoil upper and mid-airfoil lower) for different stagger angle.

From figure. 4.10 it is observed that in each case from $x/c=0$ to 0.50 the value of c_p gradually decreases. From equation 4.1 it is clear that only $p(x)$ is variable here other parameters are constant. So, a decrease in c_p value indicates that the local static pressure is also decreasing. From $x/c=0$ to 0.50, the pressure is gradually decreasing and pressure variation is not much which indicates that in this region on airfoil surface there is no such disturbance and no shock wave is present. But from $x/c=0.50$ to 1.0 pressure variation is present (either small or significant) which is described here in nine different time steps from t_1 to t_9 for different stagger angle.

In figure. 4.10(a) left side, c_p decreases linearly from $x/c=0$ to $x/c=0.5$ which implies that at $\theta=0^\circ$ on the mid-airfoil upper surface from leading edge (LE) to half of the airfoil length pressure falls gradually throughout the cycle. After $x/c=0.5$ the variation is noticeable, c_p decreases to the lowest value where unsteady pressure fluctuation is maximum and where the shock wave exists and after the shock wave there is sudden rise of local static pressure and thus c_p value increases again. Here, solid line with white circle shows that at time step $t_1=t/T=0$ shock wave is present at location $x/c=0.73$ where c_p is at its minimum value, also from figure 4.5(a) we can verify it. In the next time step at $t_2=t/T=1/8$ shock wave moves upstream at $x/c=0.69$, solid line with black circle has its minimum value also at the same value of x/c . Similarly, for the rest of the time steps of the cycle shock wave position moves upstream to $x/c=0.56$ as shown by solid line with white triangle, solid line with black triangle and solid line with white diamond. After these time steps the pressure fluctuations on the mid-airfoil upper surface is not significant as shown by solid line with black diamond, dashed line, dash-dot line. So, in these cases shock wave is also not present on the airfoil surface. At time steps $t_6=5/8$, $t_7=6/8$, $t_8=7/8$ there is no shock wave, where unsteady pressure fluctuation is not sufficient to cause the shock wave. The cycle repeats at t_9 as shown by the solid line with cross which is merged with solid line with white circle.

After this, c_p distribution for mid-airfoil lower surface at $\theta=0^\circ$ is shown in figure. 4.10(a) right side, where up to $x/c=0.5$ variation is similar i.e. c_p decreases gradually as we go along x-direction. After $x/c=0.5$, c_p decreases to a lowest value and again it increases. The difference between mid-airfoil upper and lower surface c_p distribution is that on the upper surface lowest value of c_p is found where shock is at a distant location from leading edge (at $x/c=0.73$) and time step $t1=t/T=0$ but on the lower surface the corresponding shock location is same where as time step is $t5=t/T=4/8$ (solid line with white diamond). At next time step $t6=t/T=5/8$ minimum value of c_p is found at $x/c=0.69$ as shown by solid line with black diamond where the shock wave occurs. Similarly, at $t7, t8, t9(=t)$ time steps shock wave location moves to upstream as the minimum values of c_p lines moves to left side in the figure 4.10 (a) right side, and during $t2, t3, t4$ no shock wave is seen.

Figure 4.10 (b), (c) and 4.10 (d), (e) represents c_p distribution on the mid-airfoil upper and lower surface respectively for stagger angle $5^\circ, 10^\circ, 15^\circ$ and 20° . In every cases we observe the similar scenario as described for $\theta=0^\circ$. As we have seen in Mach contour with the increase in stagger angle on the mid-airfoil upper surface shock wave start and end point moves towards downstream and on the mid-airfoil lower surface shock wave start and end point moves upstream, similarly with the increase in stagger angle for different time steps the minimum value of c_p shifts to right side for upper surface and left side for lower surface.

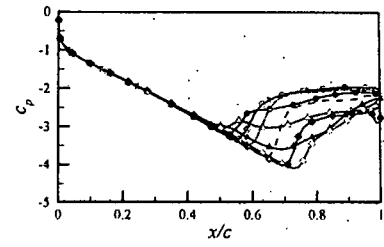
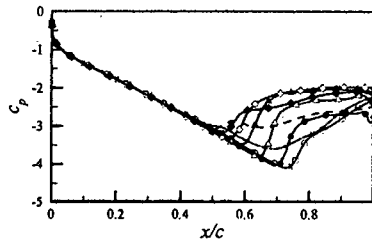
In figure. 4.10 c_p distribution have been shown separately on mid-airfoil upper surface and mid-airfoil lower surface for different stagger angles. Figure. 4.11 and 4.12 shows the Δc_p distribution along the chord length for stagger angle $0^\circ, 5^\circ, 10^\circ, 15^\circ$ and 20° respectively. Δc_p has been calculated by subtracting the c_p value on the mid-airfoil upper surface from the c_p value on the mid-airfoil lower surface in a cycle. To compare the difference in pressure distribution on the mid-airfoil upper and mid-airfoil lower surface Δc_p distributions have been plotted.

Figure. 4.11(a) shows the Δc_p distribution for stagger angle 0° for nine different time steps. From this figure, it can be said that even at approach angle 0° and stagger angle 0° upto $x/c=0.50$ there no noticeable difference in c_p . After $x/c=0.50$, there is significant difference in c_p . At time $t1$, as shown by solid line with white circle, shock occurs at $x/c=0.73$ where Δc_p has higher positive value i.e. c_p is higher on the mid-airfoil upper surface than the mid-airfoil lower surface. At time $t2$, as shown by the solid line with black circle, shock occurs at $x/c=0.69$. In this case, a small decrease in Δc_p is noticed. During $t3, t4, t5$ shock wave occurs at $x/c=0.65, 0.58$ and 0.56 and the Δc_p distributions have been shown by solid line white triangle, solid line with black triangle and solid line with white diamond respectively. During this time Δc_p gradually decreases but still it has certain positive value which indicates c_p has higher value on the mid-airfoil upper surface and shock occurs on this surface. In the next time steps $t6, t7$ and $t8$ Δc_p has negative values which indicates that c_p is higher on the mid-airfoil lower surface and the shock occurs on the mid-airfoil lower surface.

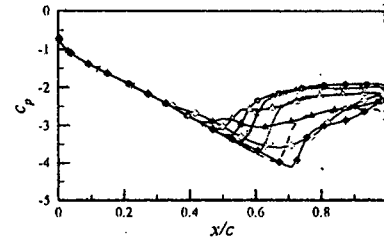
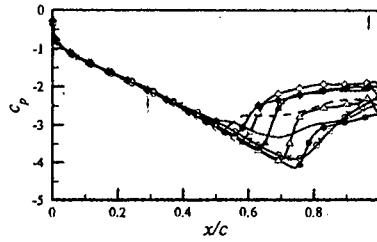
From figure. 4.11(a), (b), (c) and 4.12 (d), (e) with the increase in stagger angle from 0° to 20° , the maximum and minimum values of Δc_p varies significantly. Initially, at 0° , Δc_p has a maximum value of 2.0 and minimum value of -2.0 i.e. difference in pressure fluctuations are same in both the surfaces but at different time (180° phase difference). With the increase in stagger angle, maximum value of Δc_p gradually decreases and absolute minimum value gradually increases. Therefore, on the mid-airfoil upper surface pressure fluctuation decreases and on the mid-airfoil lower surface pressure fluctuation slightly increases.

Mid-airfoil upper surface

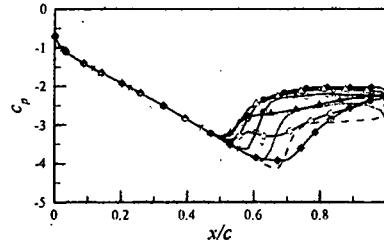
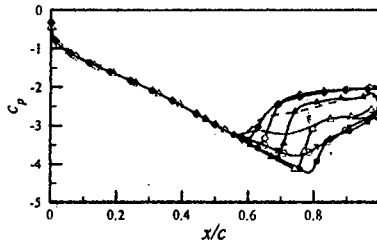
Mid-airfoil lower surface



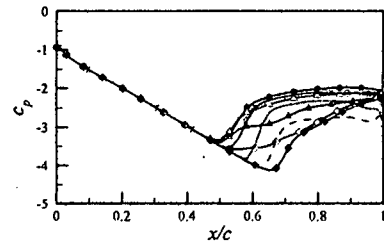
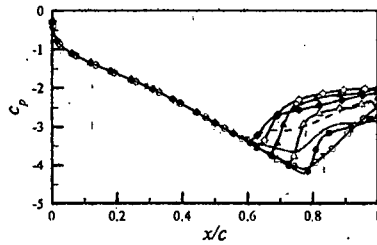
(a) $\theta=0^\circ$



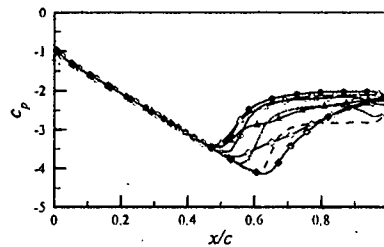
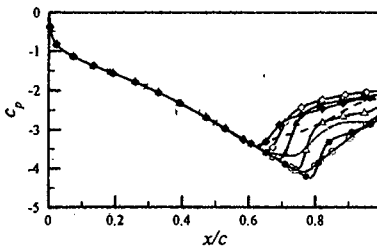
(b) $\theta=5^\circ$



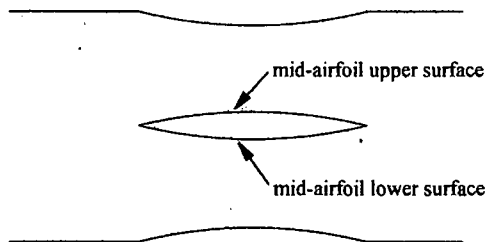
(c) $\theta=10^\circ$



(d) $\theta=15^\circ$



(e) $\theta=20^\circ$



- t1
- t2
- t3
- t4
- t5
- t6
- t7
- t8
- t9

Figure 4.10 c_p distribution ($\theta=0^\circ, 5^\circ, 10^\circ, 15^\circ, 20^\circ$).

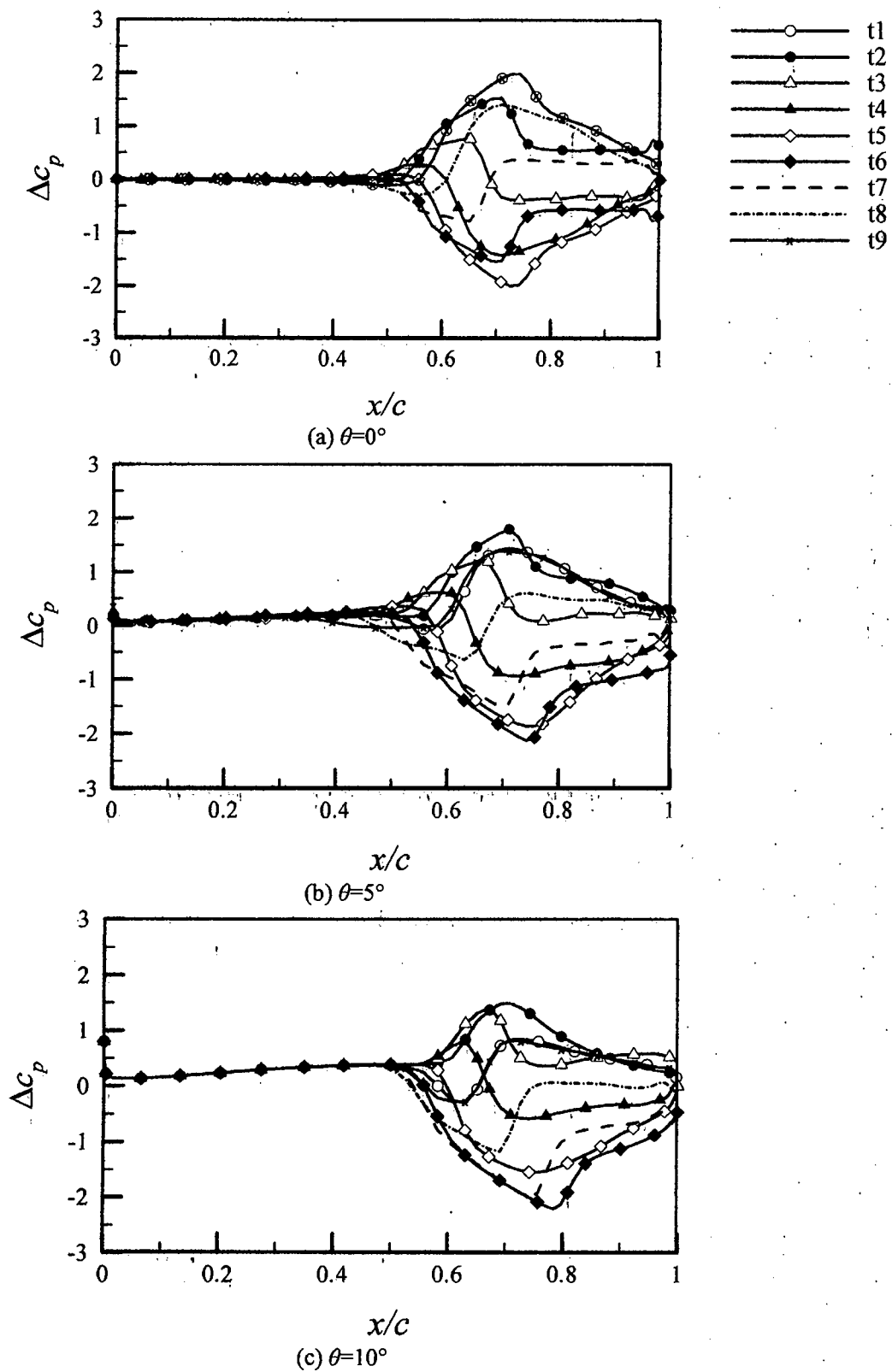


Figure. 4.11 Δc_p vs x/c for stagger angle (a) $\theta=0^\circ$ (b) $\theta=5^\circ$ (c) $\theta=10^\circ$

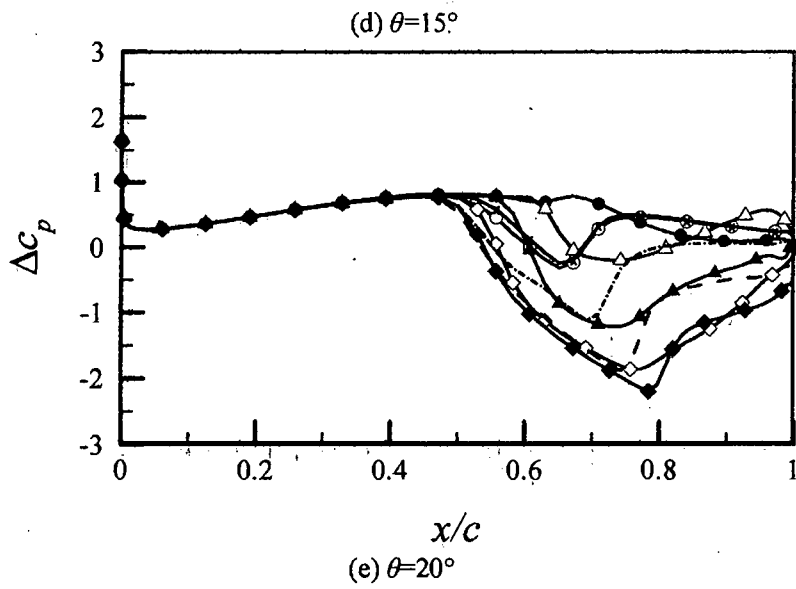
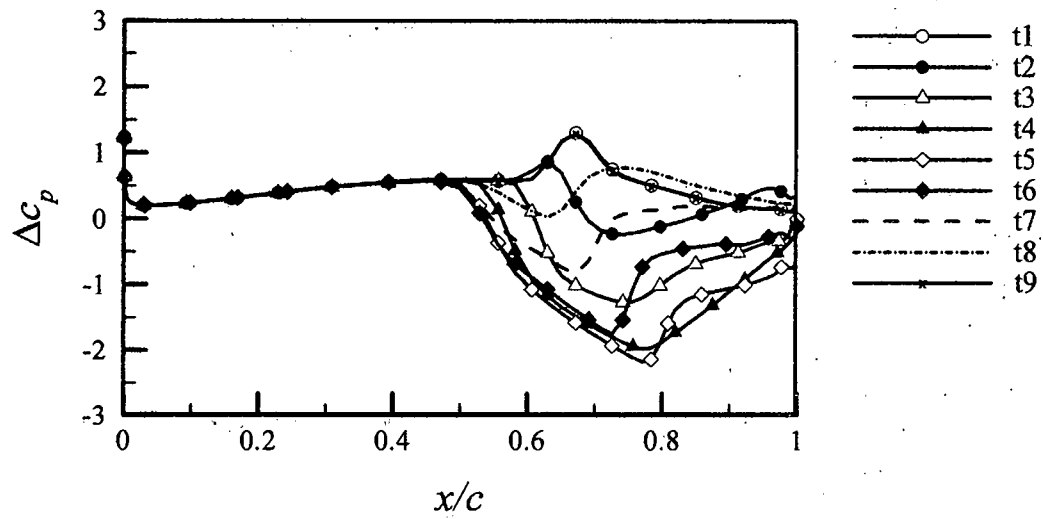


Figure. 4.12 ΔC_p vs x/c for stagger angle (d) $\theta = 15^\circ$ (e) $\theta = 20^\circ$

4.4 UNSTEADY SHOCK POSITION

Shock wave characteristics are studied by analyzing the unsteady shock locations on the mid-airfoil upper and mid-airfoil lower surface for stagger angle 0° to 20° at different time steps as shown in figure. 4.13 When the unsteady pressure wave got uniform unsteady, we selected two cycles from them and one cycle was divided into eight divisions. The shock wave position was selected from the unsteady pressure data points, when the pressure was at its minimum value the corresponding x/c value was selected as shock location x/c for that time step.

In figure. 4.13 shock wave location was shown against time for mid-airfoil upper surface (solid line with white circle) and mid-airfoil lower surface (solid line with black circle). From the plot it's evident that the shock wave oscillation is discontinuous. In figure 4.13 (a) for $\theta=0^\circ$, on mid-airfoil upper surface the cycle starts at $t/T=0$ for which the shock location is at $x/c=0.73$ (most distant point from leading edge), as t/T increases to 0.125 the shock occurs at $x/c=0.69$. In the same way for $t/T=0.25, 0.375$ and 0.5 shock occurs at $x/c=0.65, 0.58, 0.56$ locations respectively. After that the shock vanishes and again starts at $t/T=1$. From $t/T=0$ to 0.5 the solid line indicates that shock wave continuously moving upstream and from $t/T=0.5$ to 1 the dotted line indicates that no shock wave is present in this region. So, we can see shock is oscillating from trailing edge to leading edge from $x/c=0.73$ to $x/c=0.56$ and then vanishes. In the mid-airfoil lower surface same type of oscillation is observed. At $t/T=0$ shock wave is seen at 0.56 and after that shock wave vanishes. Then the shock wave re-appears at $t/T=0.5$ when the shock on the mid-airfoil upper surface is at its last state. At $t/T=0.5$ on the mid-airfoil lower surface shock wave is seen at $x/c=0.73$ and in the next steps the shock gradually moves upstream. As the stagger angle is increased from 0° to 20° the shock wave type do not change but on the mid-airfoil upper surface shock start position moves downstream (from $0.73c$ to $0.784c$) and shock end position also moves downstream (from $0.56c$ to $0.651c$). In case of mid-airfoil lower surface shock start position moves upstream (from $0.73c$ to $0.629c$) and shock end position also moves upstream (from $0.56c$ to $0.5c$) as shown in figure. 4.13.

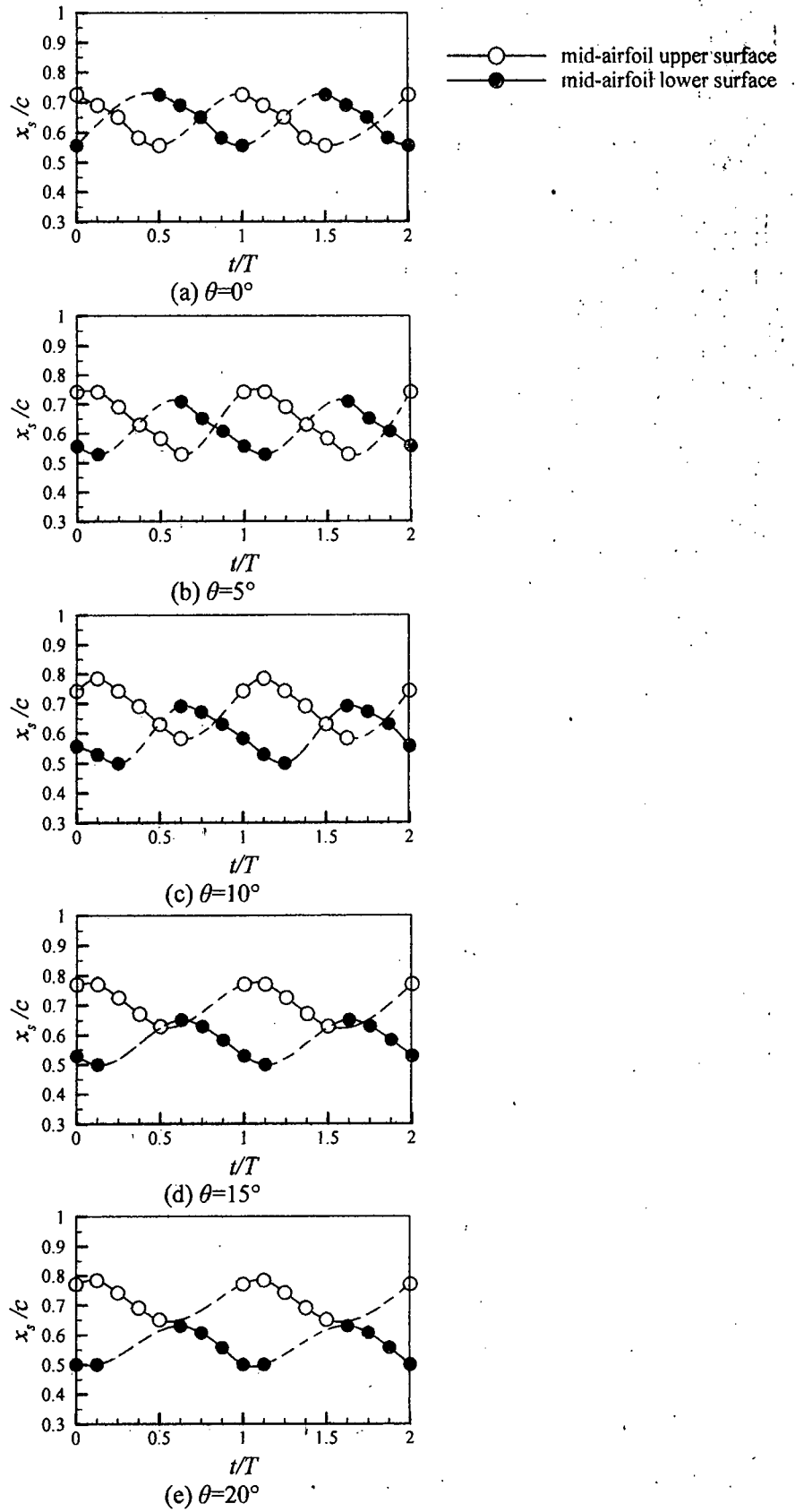


Figure. 4.13 Shock position for different stagger angle

4.5 Shock strength

In the present study pressure rise across the shock is taken as the indicator of shock strength. Pressure rise across shock wave is $(\Delta p/p_1)$. These data are collected along two lines parallel to x-axis (Line-1 and Line-2) passing through $y/c=0.1, y/c=-0.1$. The pressure rise across shock wave $(\Delta p/p_1)$ is measured by reading the minimum static pressure just ahead of the shock and the maximum sudden pressure rise across the shock as shown in figure. 4.14, right side. Figure. 4.15 represents the pressure rise across the shock in two cycles. The figure indicates the initial strength gain of the shock and then reduction of shock strength with time for all cases.

From figure 4.15 (a) it can be noticed that for $\theta=0^\circ$ when the upper shock vanishes ($t/T>0.5$) the value of $\Delta p/p_1$ for upper shock falls below 0.30. That means the shock wave becomes a compression wave when the total pressure rise across it falls below 0.30. The same value is taken for all cases. $\Delta p/p_1=0.30$ is a threshold value for shock to transform into a compression wave. This threshold value can vary depending on the type of flow (internal/external), upstream Mach number, airfoil thickness, incidence angle, operating condition etc. [37].

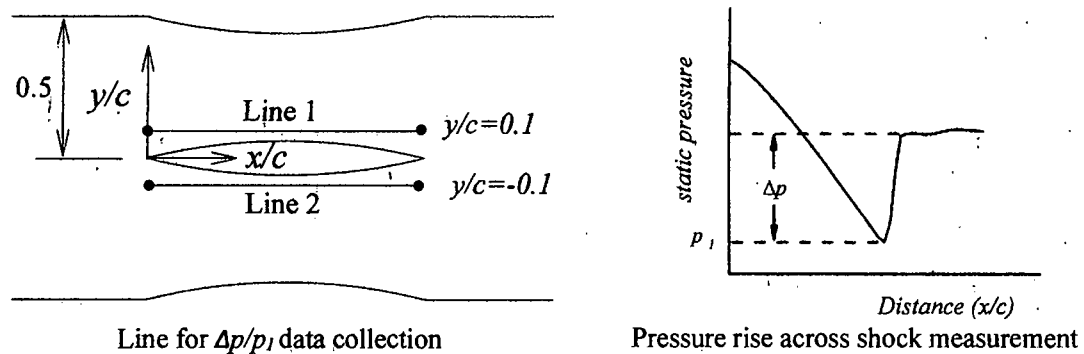


Figure. 4.14 $(\Delta p/p_1)$ data collection line and pressure rise across shock wave measurement

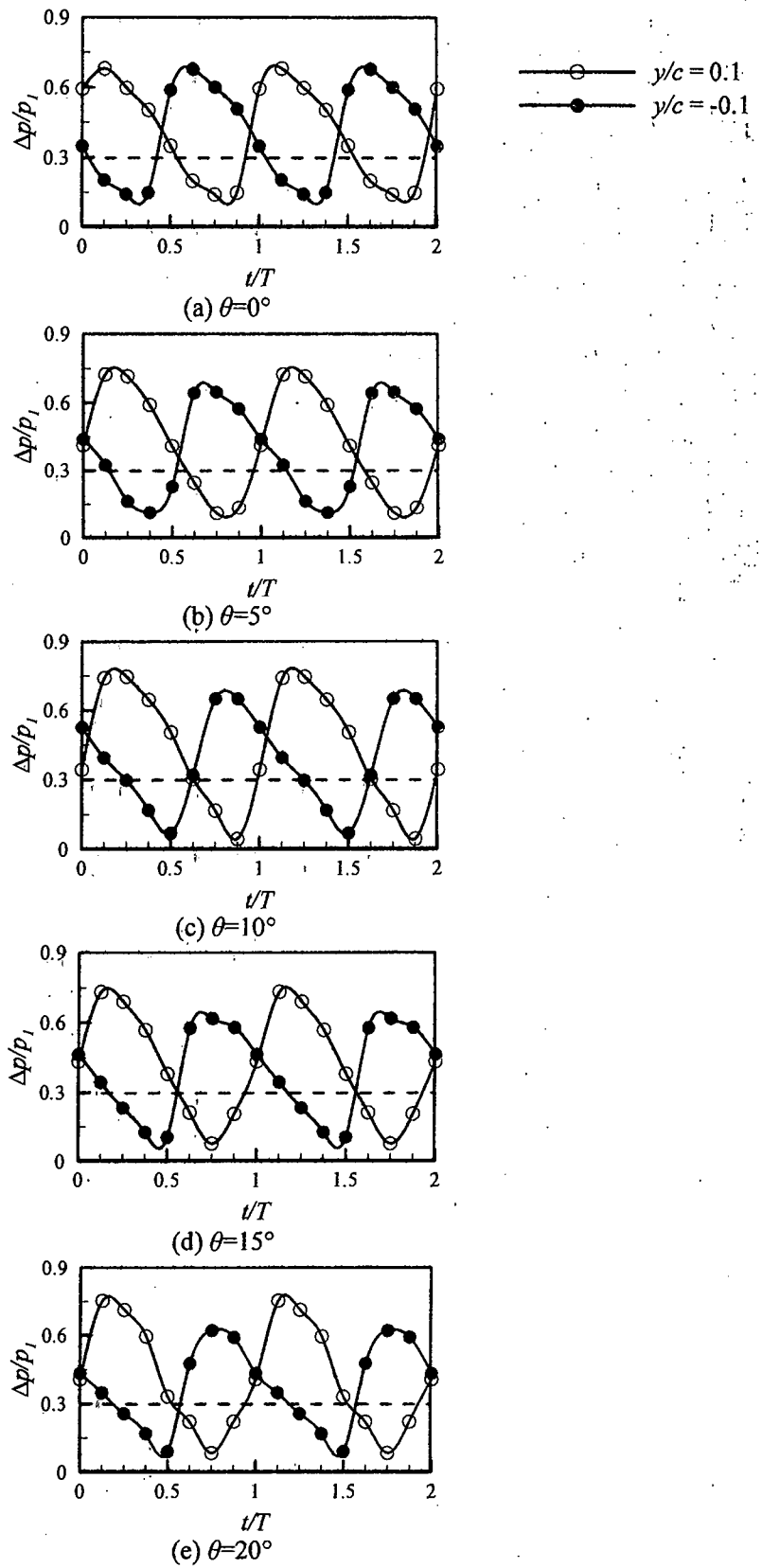


Figure. 4.15 Pressure rise across shock wave

4.6 UNSTEADY PRESSURE DISTRIBUTION

Shock wave oscillation and its interaction with the boundary layer causes unsteady pressure fluctuation on the airfoil surfaces named mid-airfoil upper surface, mid-airfoil lower surface, upper airfoil lower surface and lower airfoil upper surface. To observe the pressure distribution on the airfoil surfaces eighteen points on mid-airfoil upper surface, eighteen points on the mid-airfoil lower surface, ten points on the upper airfoil lower surface and another ten points on the lower airfoil upper surface are selected as shown in figure. 4.16. Also to see the pressure fluctuation on the wake another five points are selected. On the selected coordinate points unsteady pressure data was saved at time step size of $1\mu\text{s}$.

Figure. 4.17 to 4.19 represents the pressure distribution on the mid-airfoil upper and mid-airfoil lower surface at three locations $x/c=0.71, 0.75$ and 0.83 . These three points have been selected as in these locations pressure fluctuates with higher amplitude. The variation is observed for $\theta=0^\circ$ to 20° . Three cycle is chosen where pressure fluctuation is uniform unsteady. In figure. 4.17 (a) for $\theta=0^\circ$ and at $x/c=0.71$ it is observed that pressure fluctuation is maximum on both mid-airfoil upper and lower surface. But when the pressure on the mid-airfoil upper surface is at its maximum value then the pressure on the mid-airfoil lower surface is at around its minimum value. After that as the pressure on the mid-airfoil upper surface gradually decreases, on the mid-airfoil lower surface pressure gradually increases.

Then for different airfoil surfaces and wake points static pressure-time histories were plotted as shown in figure. 4.20 to 4.44 for stagger angle 0° to 20° respectively. In each of the cases it was observed that initially the oscillation had to undergo a developing phase and after that fluctuation got uniform unsteady behavior.

In figure. 4.20 static pressure vs. time curves are plotted for mid-airfoil upper surface ($\theta=0^\circ$), where it is observed that from leading edge (LE) $x/c=0$ to $x/c=0.42$ there is very small amount of pressure fluctuation. From $x/c=0.5$ to trailing edge (TE) $x/c=1$ there is significant amount of pressure fluctuation. At $x/c=0.5$ to $x/c=0.71$ pressure fluctuation gradually rises. At $x/c=0.71$ pressure fluctuation with maximum amplitude is noticed which results from unsteady shock movement and shock induced strong boundary layer separation. From $x/c=0.71$ to $x/c=1$ amplitude of pressure oscillation again decreases gradually. On the mid-airfoil lower surface pressure fluctuation is similar to upper surface and here pressure fluctuates with maximum amplitude also at $x/c=0.71$ (figure. 4.21). On the upper airfoil lower surface (figure. 4.22) and lower airfoil upper surface (figure. 4.23) maximum amplitude of pressure fluctuation is observed at $x/c=0.67$. Along the wake points (figure. 4.24) the amplitude is not significant as compared to the surface points but here frequency is higher.

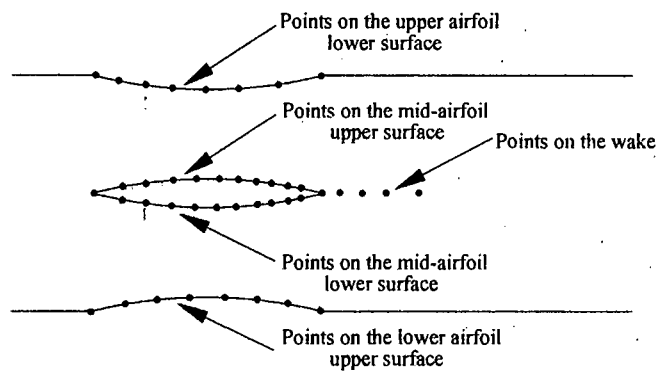


Figure. 4.16 Points on the airfoil cascade surfaces and wake

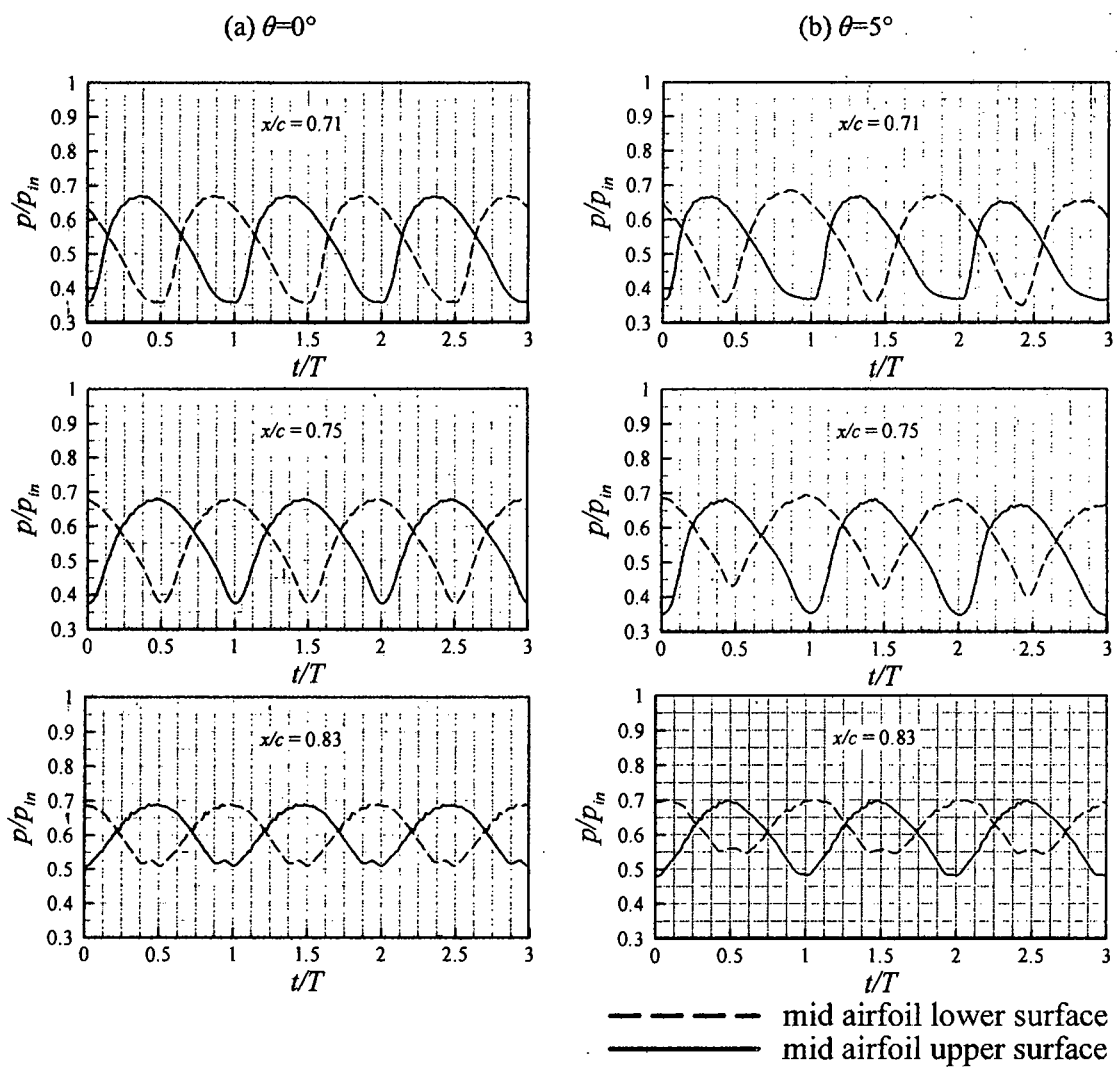


Figure. 4.17 Pressure distribution on mid-airfoil upper and mid-airfoil lower surface ($\theta=0^\circ, 5^\circ$)

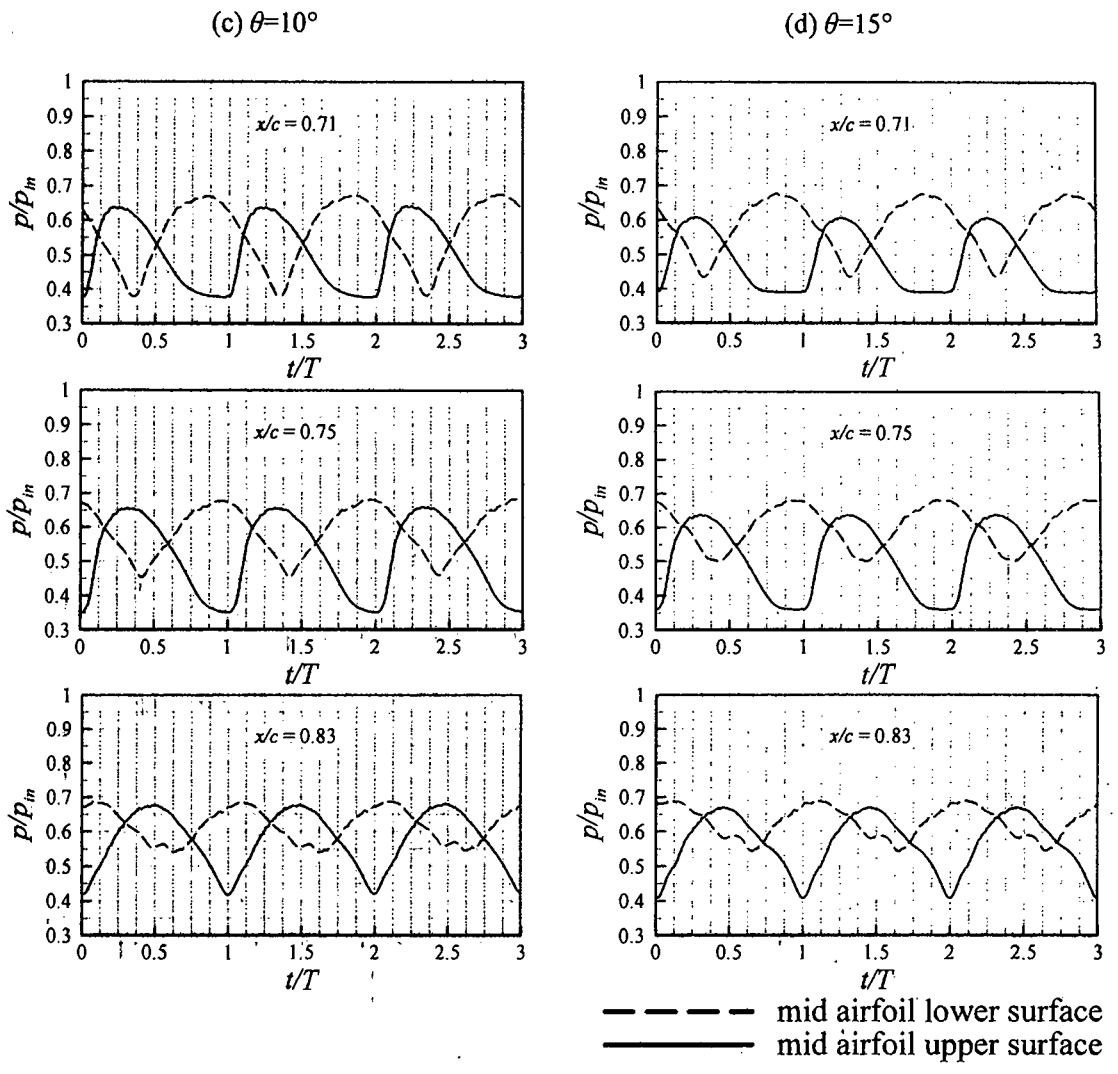


Figure. 4.18 Pressure distribution on mid-airfoil upper and mid-airfoil lower surface ($\theta=10^\circ, 15^\circ$)

(e) $\theta=20^\circ$

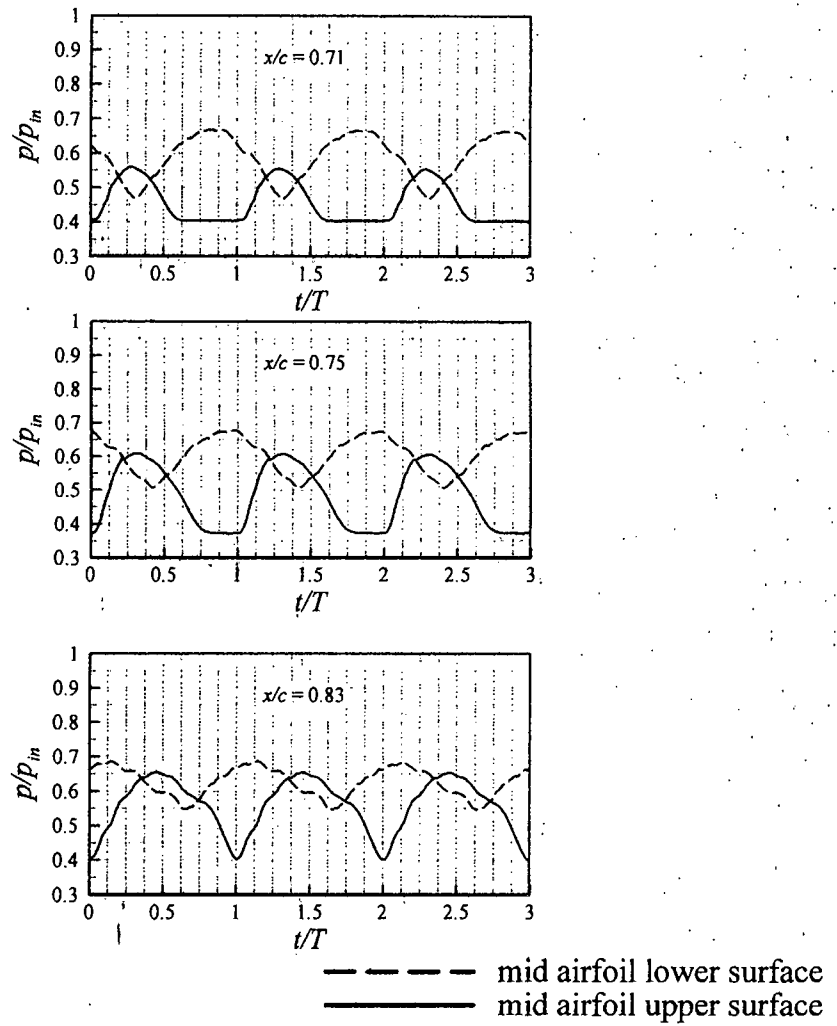


Figure. 4.19 Pressure distribution on mid-airfoil upper and mid-airfoil lower surface ($\theta=20^\circ$)

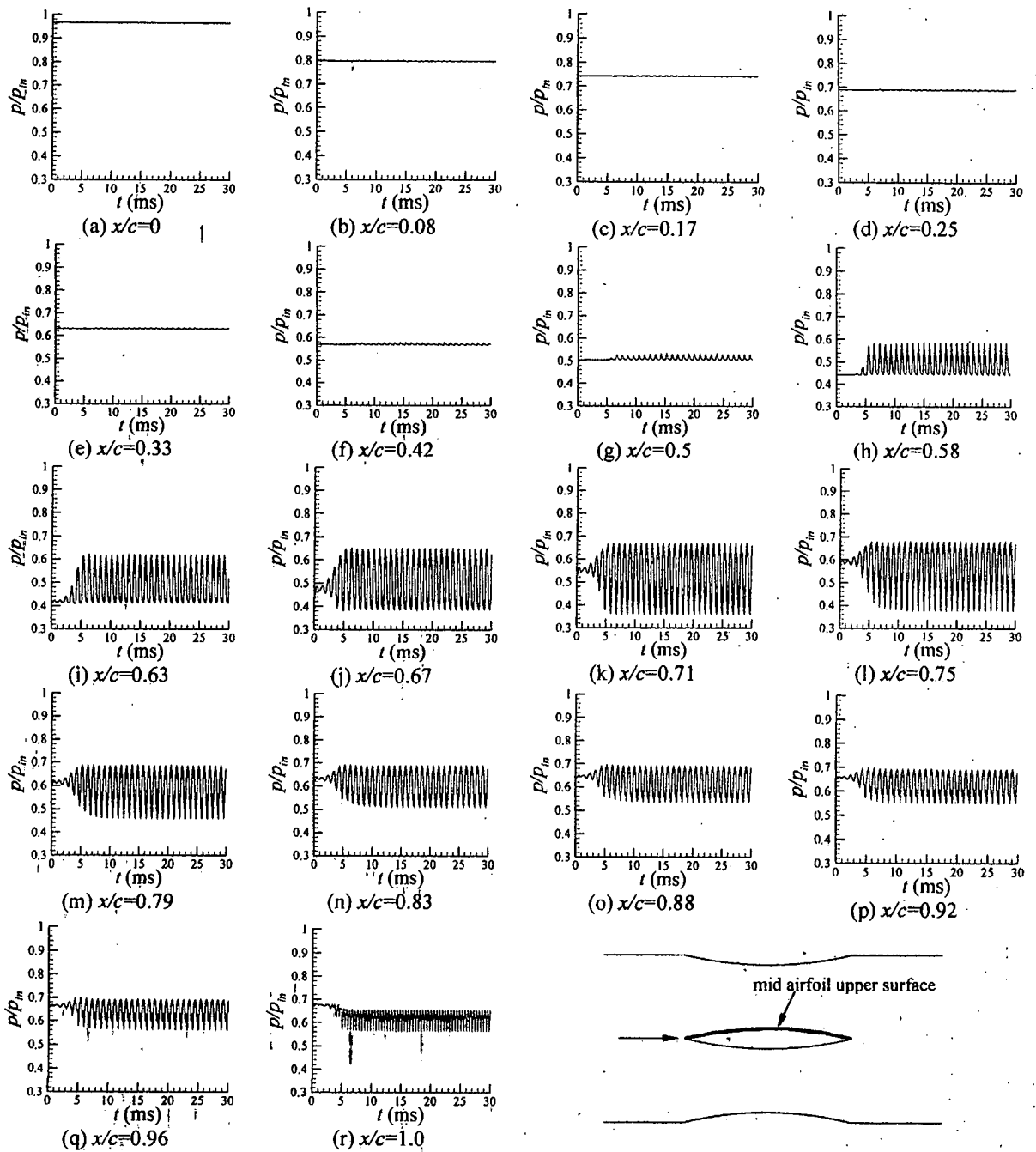


Figure. 4.20 Static pressure-time histories in the flow field around an airfoil at different points on the mid-airfoil upper surface for $PR=0.75$ (stagger angle, $\theta=0^\circ$)

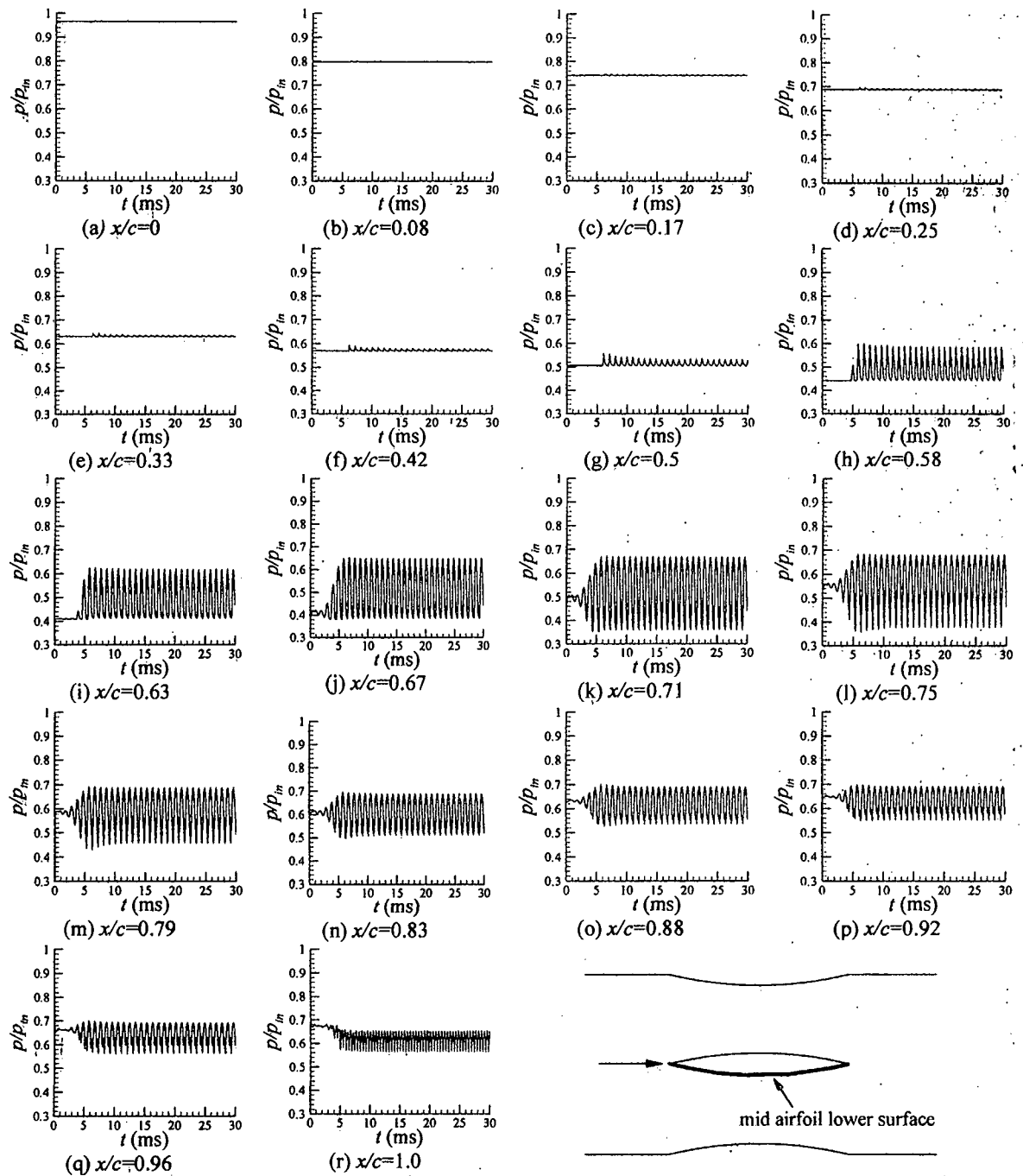


Figure. 4.21 Static pressure-time histories in the flow field around an airfoil at different points on the mid-airfoil lower surface for $PR=0.75$ (stagger angle, $\theta=0^\circ$)

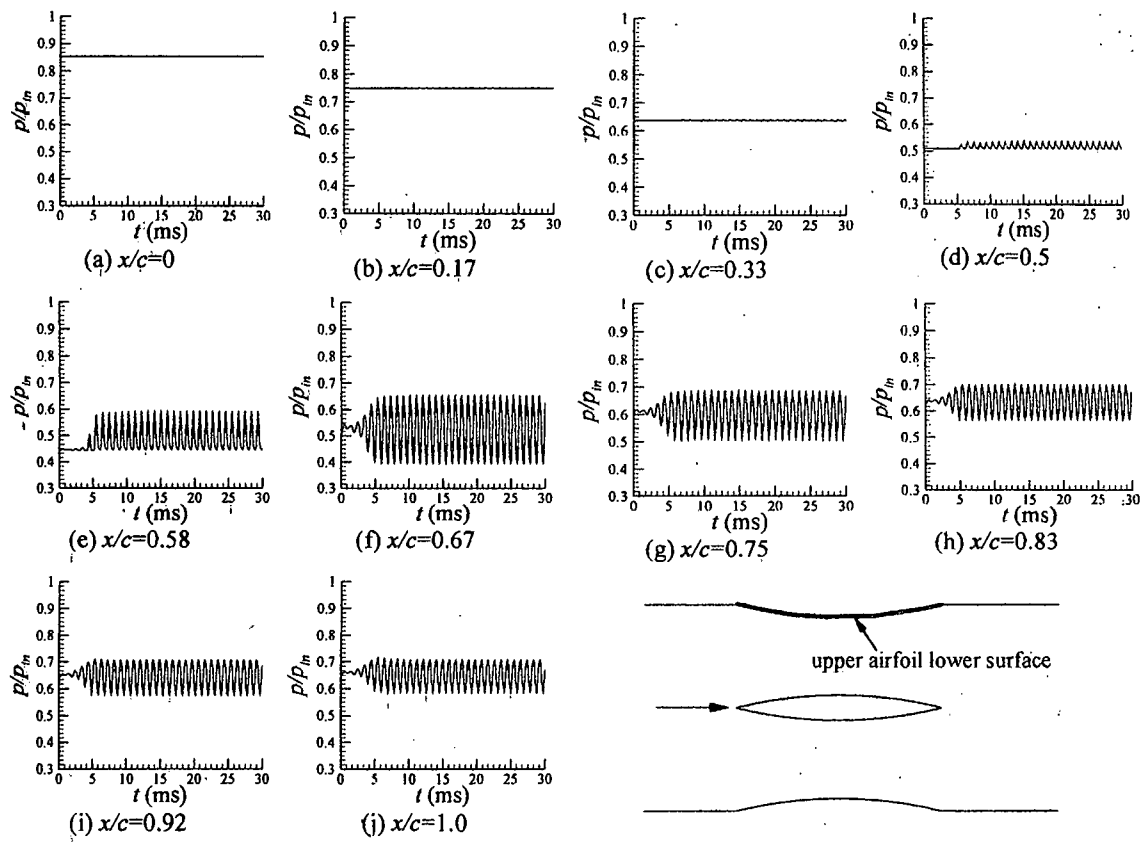


Figure 4.22 Static pressure-time histories in the flow field around an airfoil at different points on the upper airfoil lower surface for $PR=0.75$ (stagger angle, $\theta=0^\circ$)

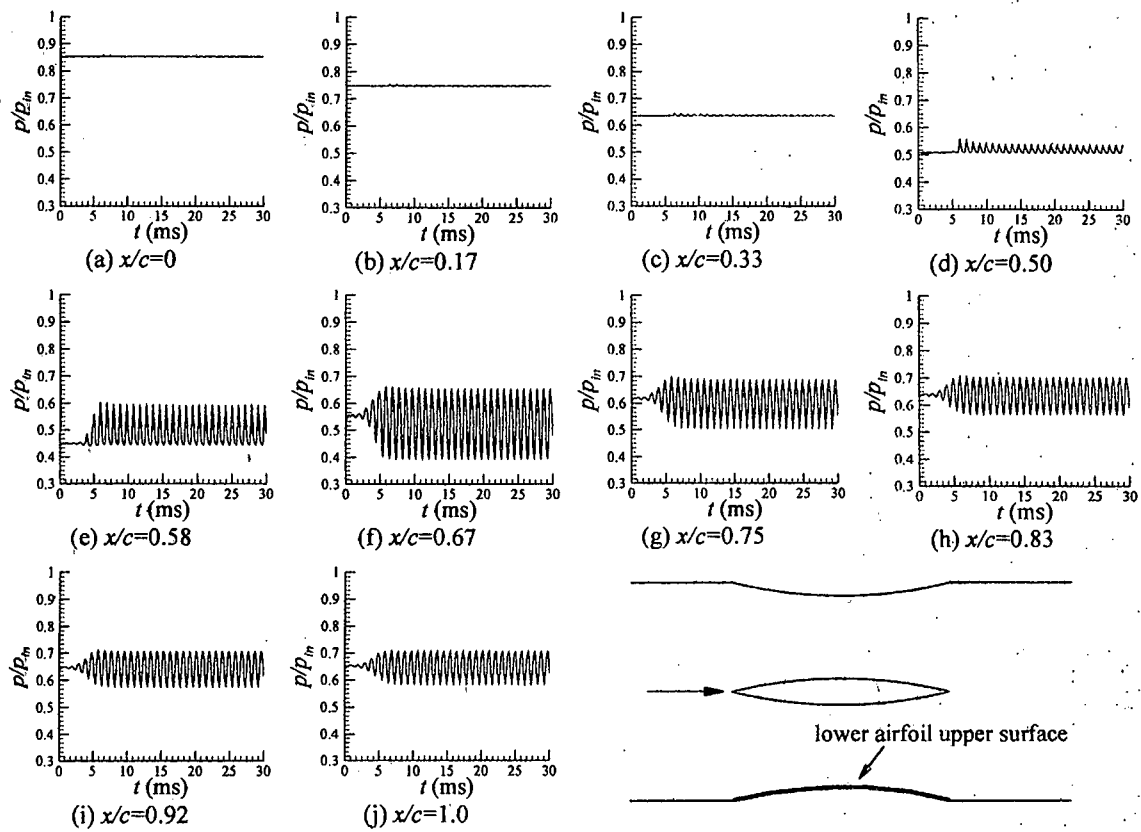


Figure 4.23 Static pressure-time histories in the flow field around an airfoil at different points on the lower airfoil upper surface for PR=0.75 (stagger angle, $\theta=0^\circ$)

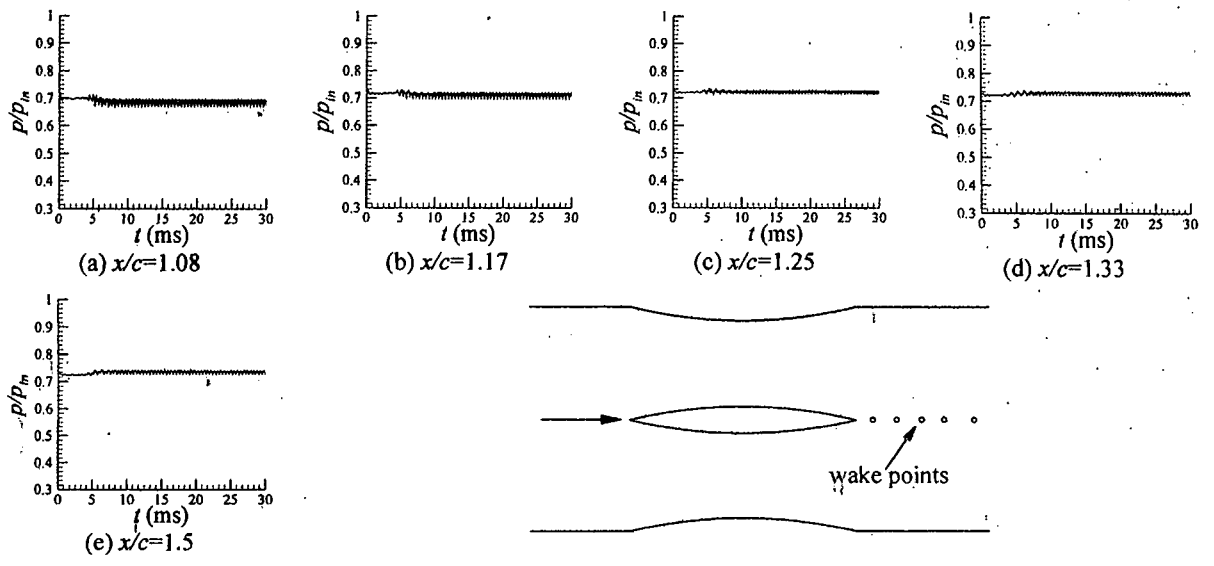


Figure. 4.24 Static pressure-time histories in the flow field at different points of the wake for PR=0.75 (stagger angle, $\theta=0^\circ$)

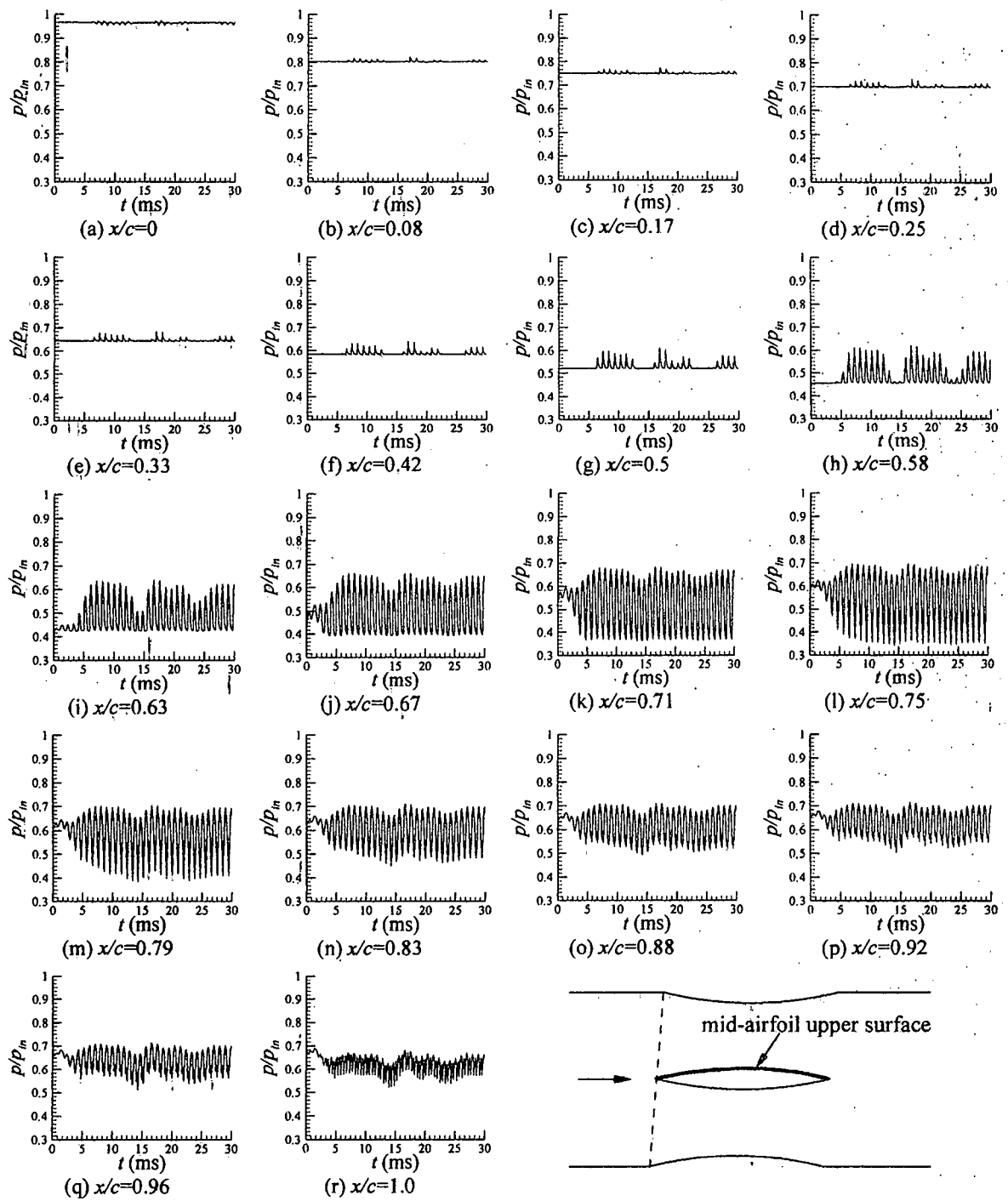


Figure. 4.25 Static pressure-time histories in the flow field around an airfoil at different points on the mid-airfoil upper surface for $PR=0.75$ (stagger angle, $\theta=5^\circ$)

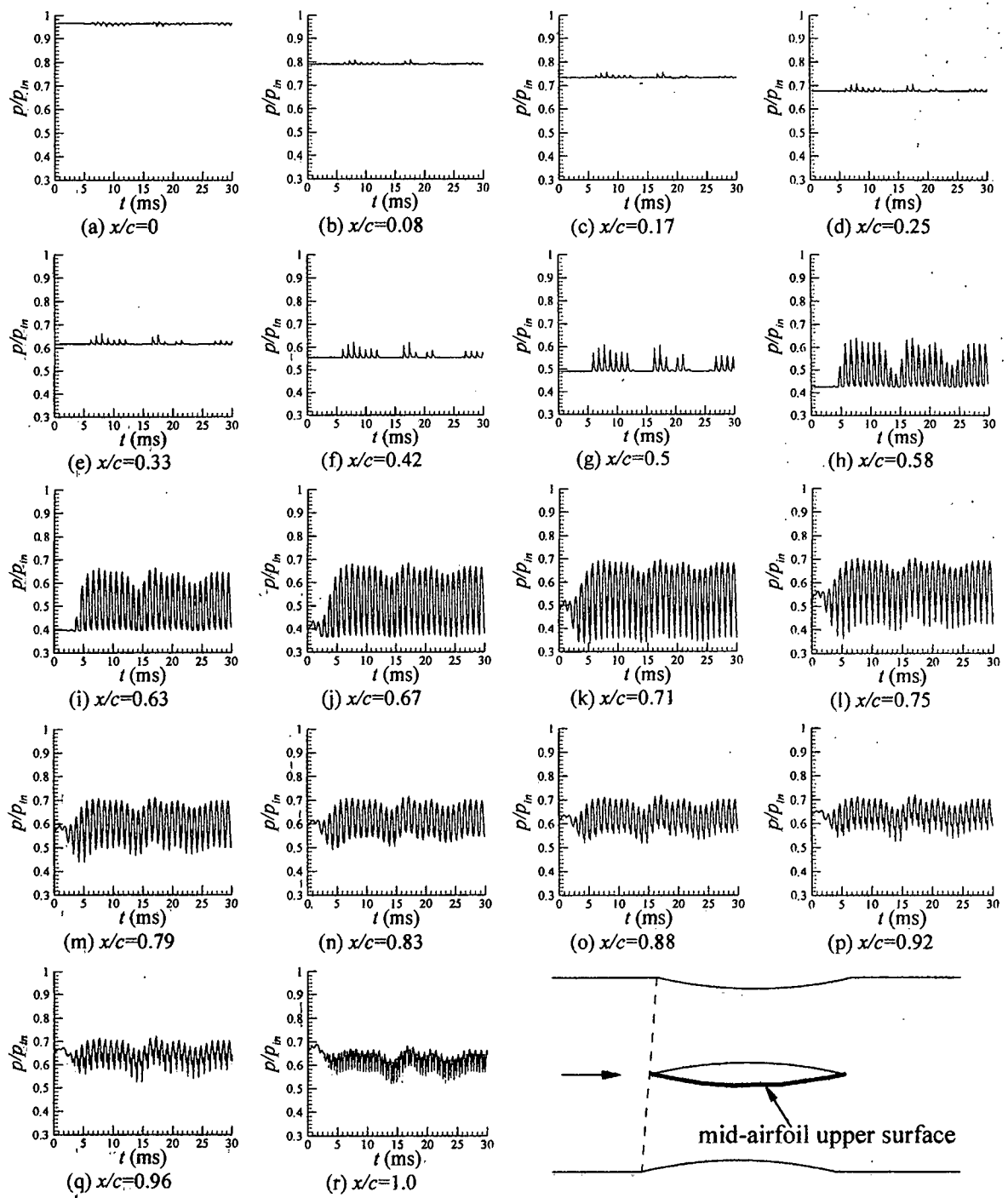


Figure. 4.26 Static pressure-time histories in the flow field around an airfoil at different points on the mid-airfoil lower surface for $PR=0.75$ (stagger angle, $\theta=5^\circ$)

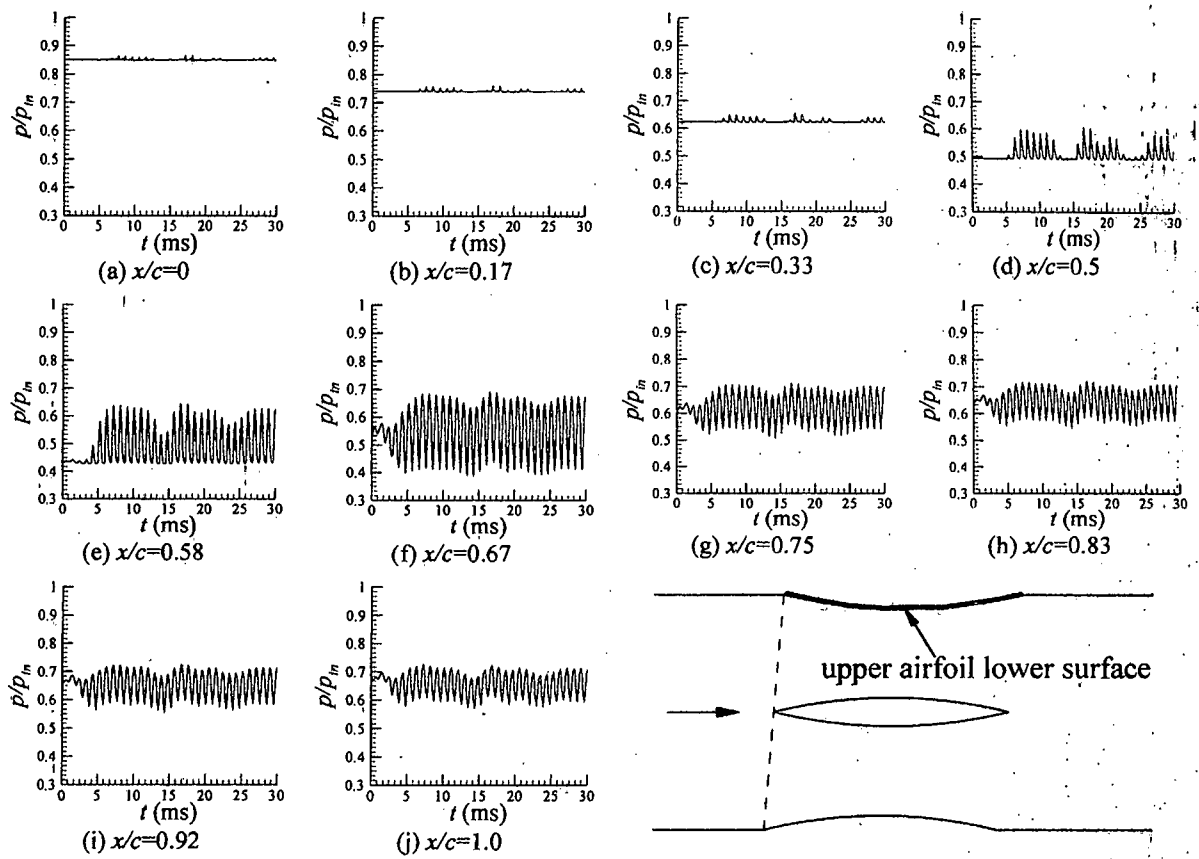


Figure 4.27 Static pressure-time histories in the flow field around an airfoil at different points on the upper airfoil lower surface for $PR=0.75$ (stagger angle, $\theta=5^\circ$)

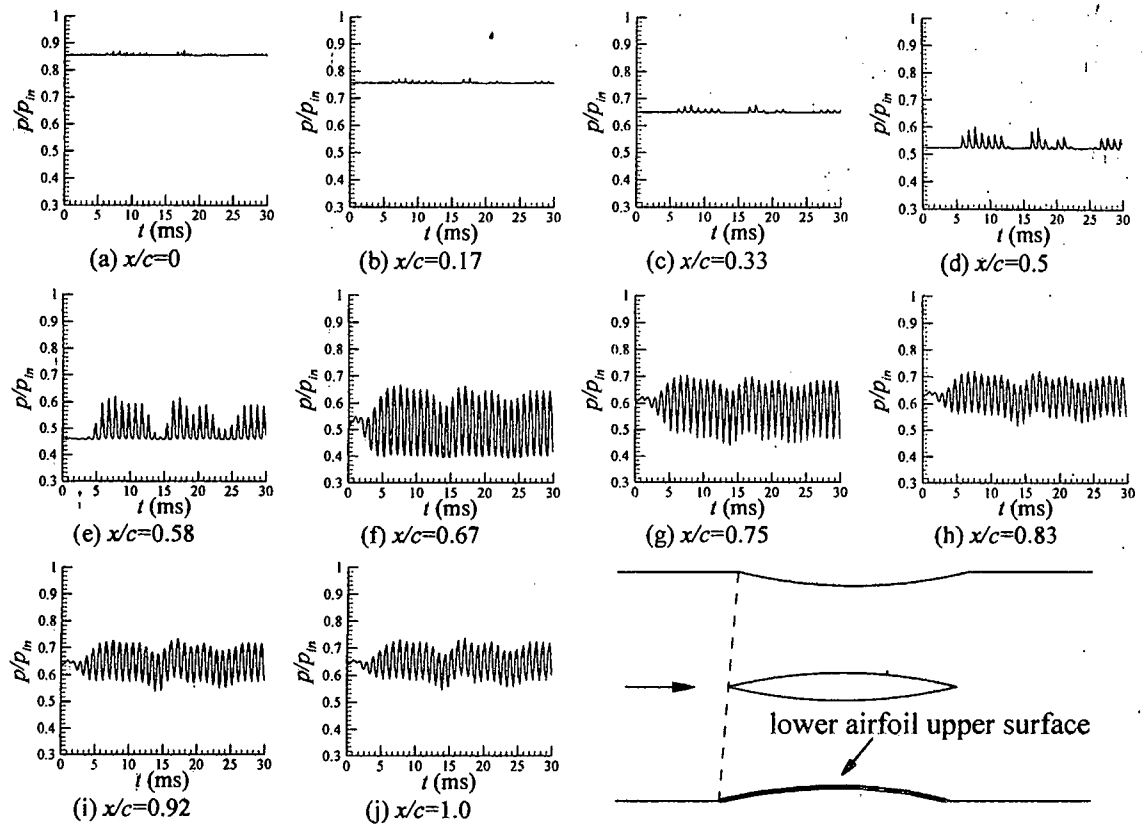


Figure. 4.28 Static pressure-time histories in the flow field around an airfoil at different points on the lower airfoil upper surface for $PR=0.75$ (stagger angle, $\theta=5^\circ$)

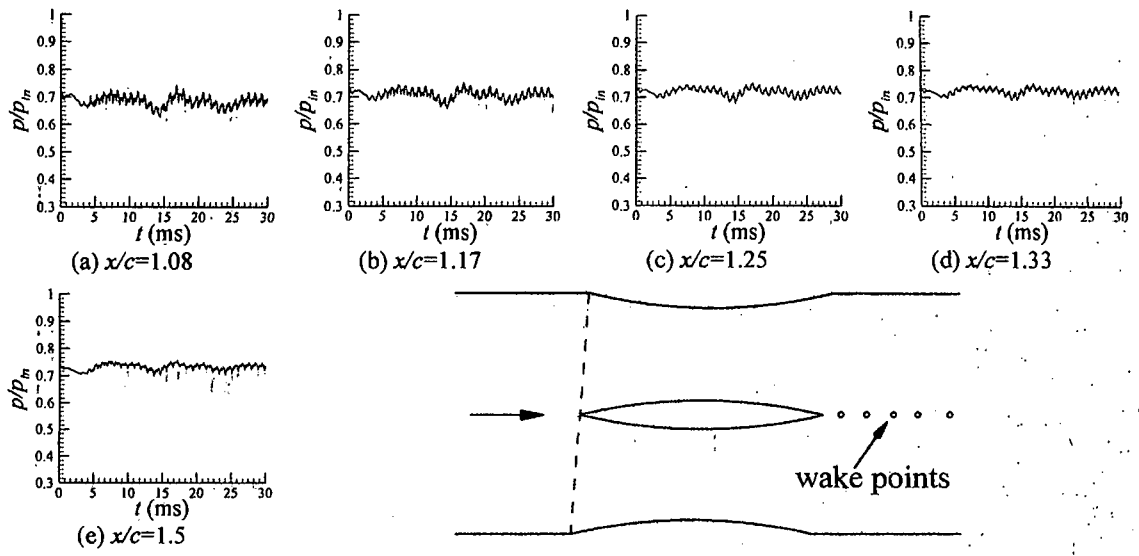


Figure. 4.29 Static pressure-time histories in the flow field around an airfoil at different points on the wake for $PR=0.75$ (stagger angle, $\theta=5^\circ$)

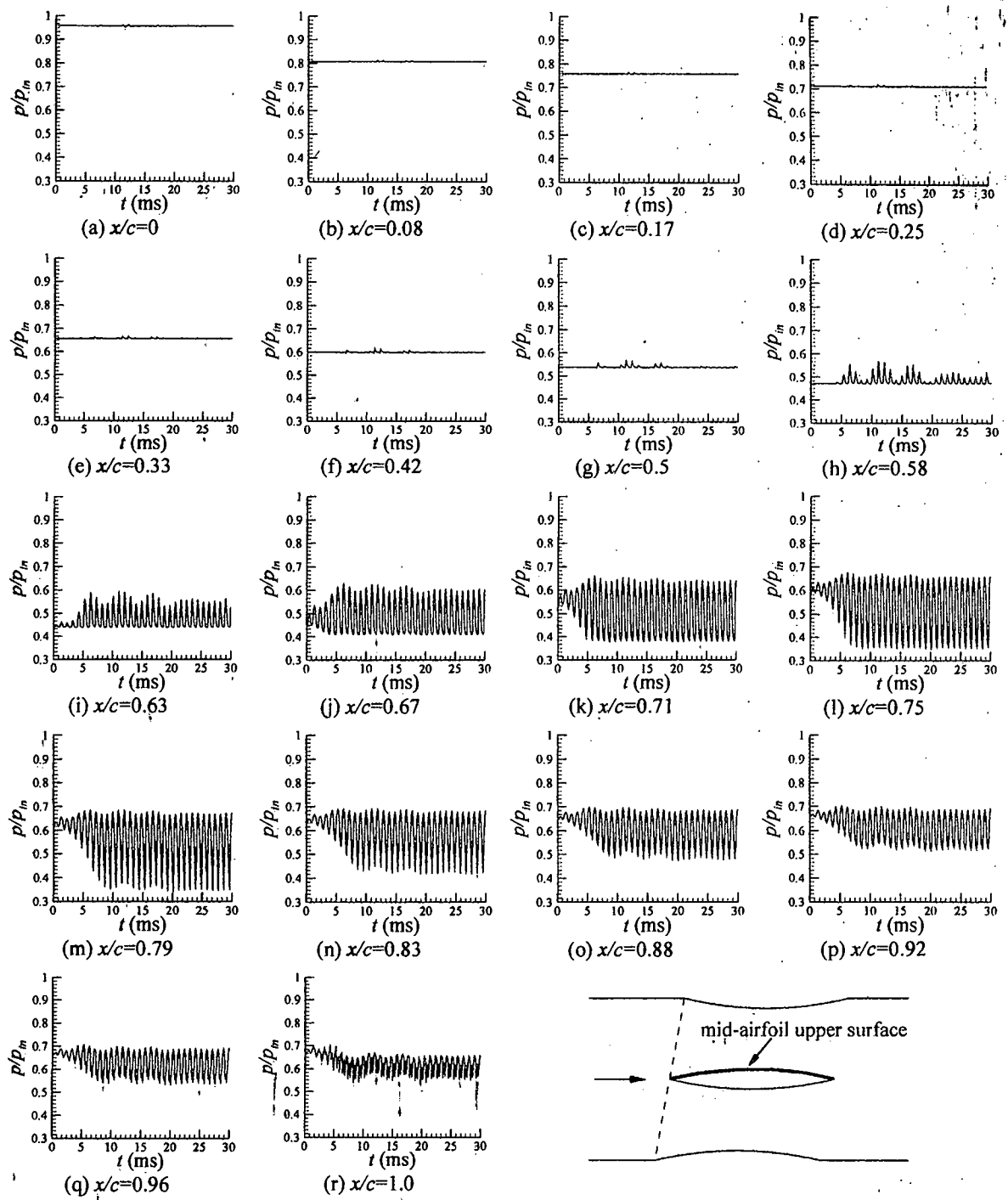


Figure 4.30 Static pressure-time histories in the flow field around an airfoil at different points on the mid-airfoil upper surface for $PR=0.75$ (stagger angle, $\theta=10^\circ$)

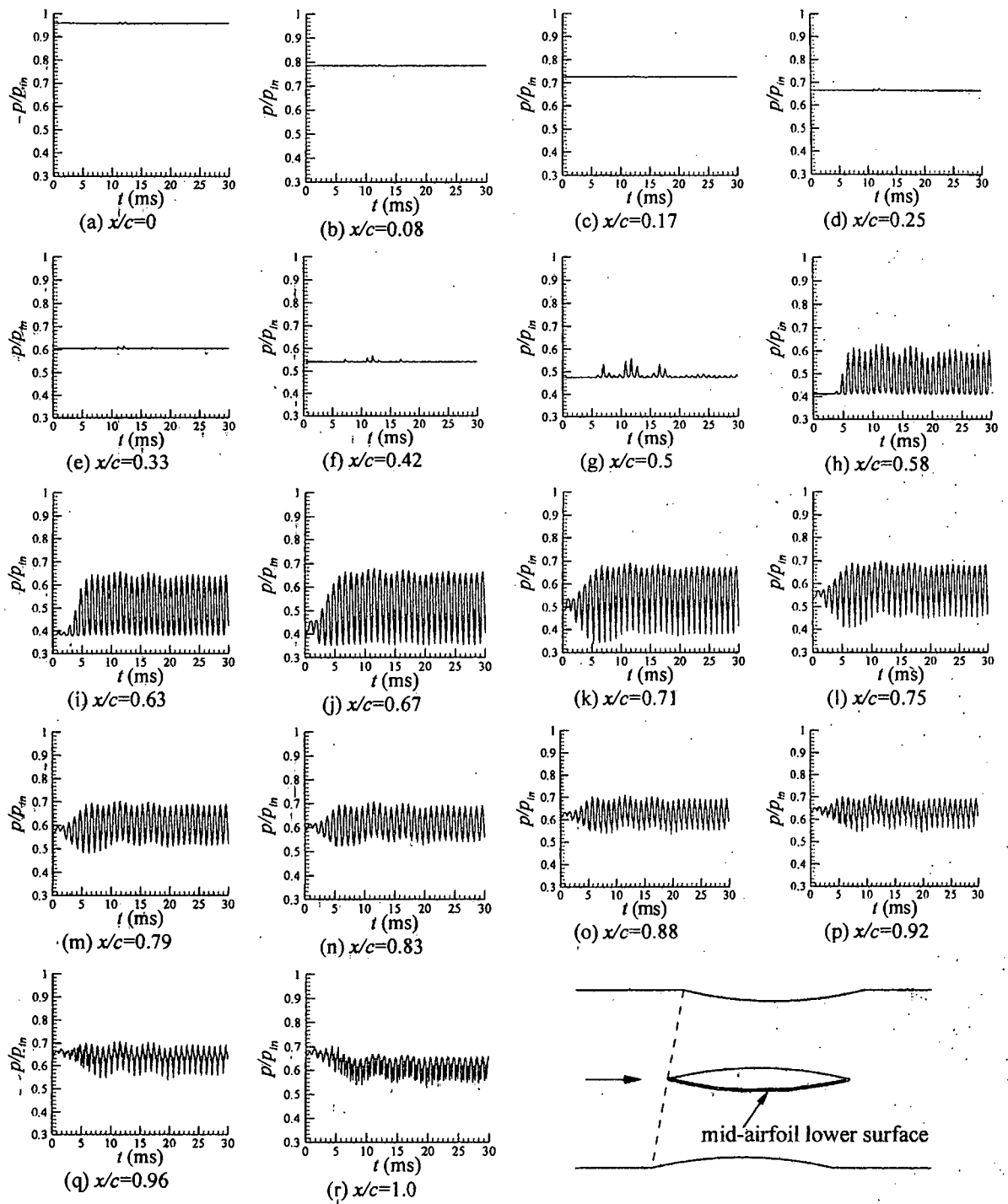


Figure. 4.31 Static pressure-time histories in the flow field around an airfoil at different points on the mid-airfoil lower surface for $PR=0.75$ (stagger angle, $\theta=10^\circ$).

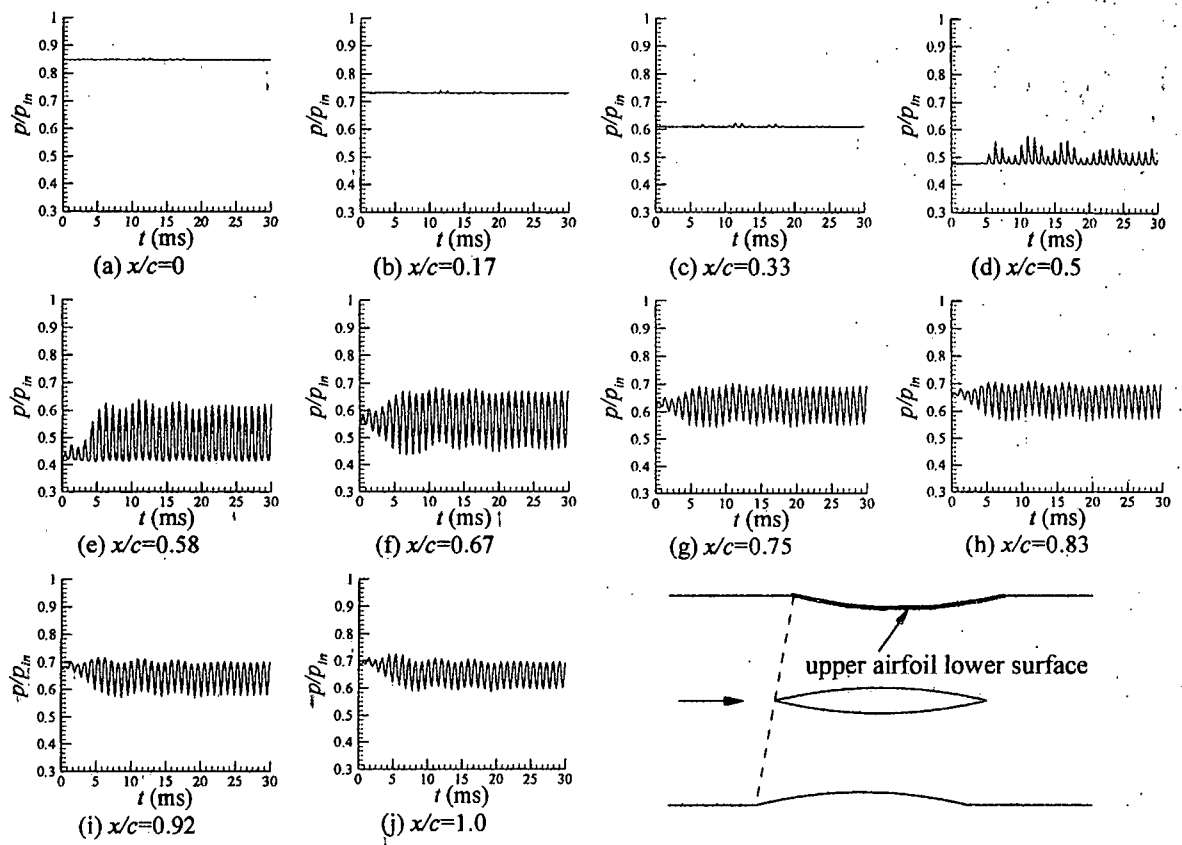


Figure. 4.32 Static pressure-time histories in the flow field around an airfoil at different points on the upper airfoil lower surface for $PR=0.75$ (stagger angle, $\theta=10^\circ$)

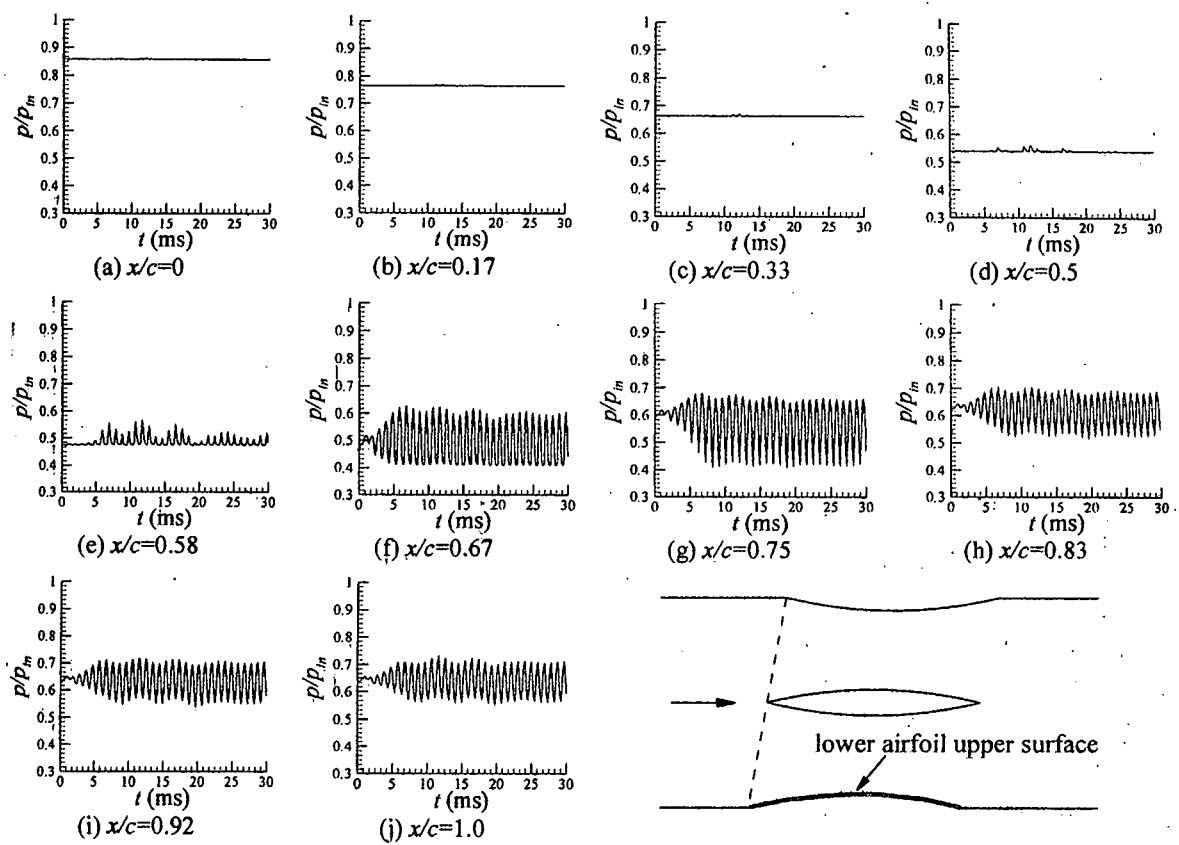


Figure. 4.33 Static pressure-time histories in the flow field around an airfoil at different points on the lower airfoil upper surface for $PR=0.75$ (stagger angle, $\theta=10^\circ$)

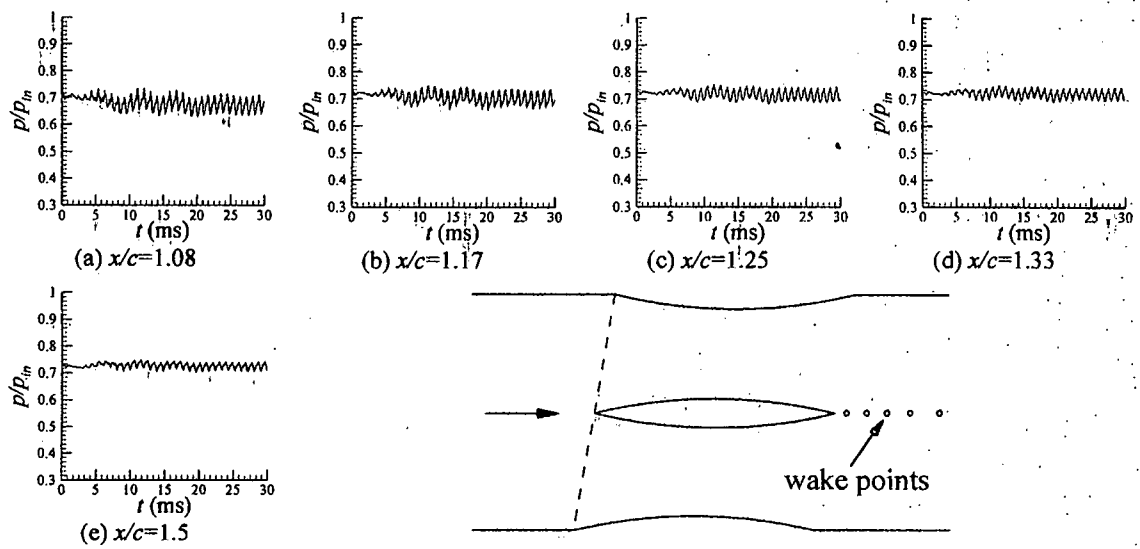


Figure 4.34 Static pressure-time histories in the flow field around an airfoil at different points on the wake for $PR=0.75$ (stagger angle, $\theta=10^\circ$)

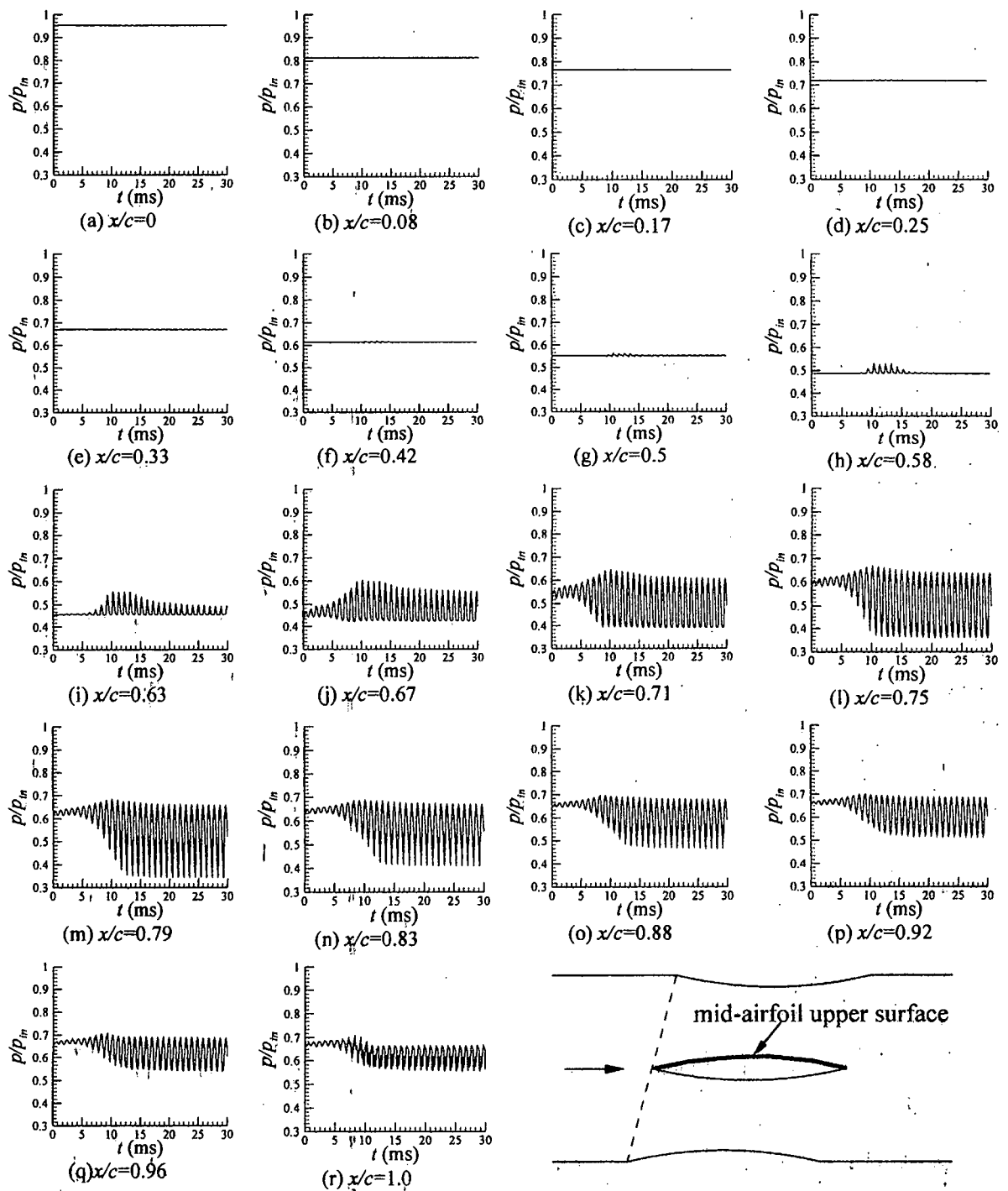


Figure 4.35 Static pressure-time histories in the flow field around an airfoil at different points on the mid-airfoil upper surface for $PR=0.75$ (stagger angle, $\theta=15^\circ$)

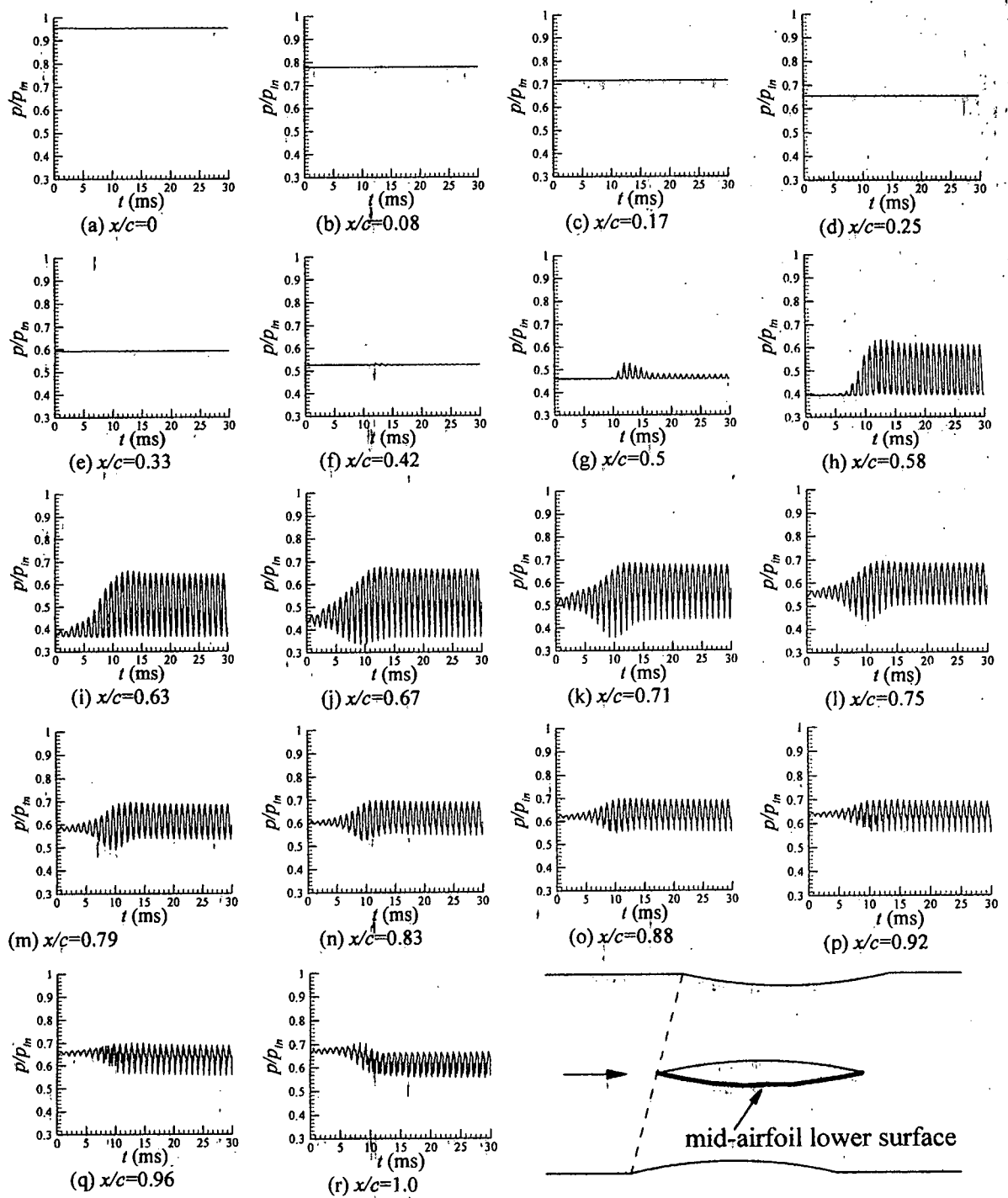


Figure. 4.36 Static pressure-time histories in the flow field around an airfoil at different points on the mid-airfoil lower surface for $PR=0.75$ (stagger angle, $\theta=15^\circ$)

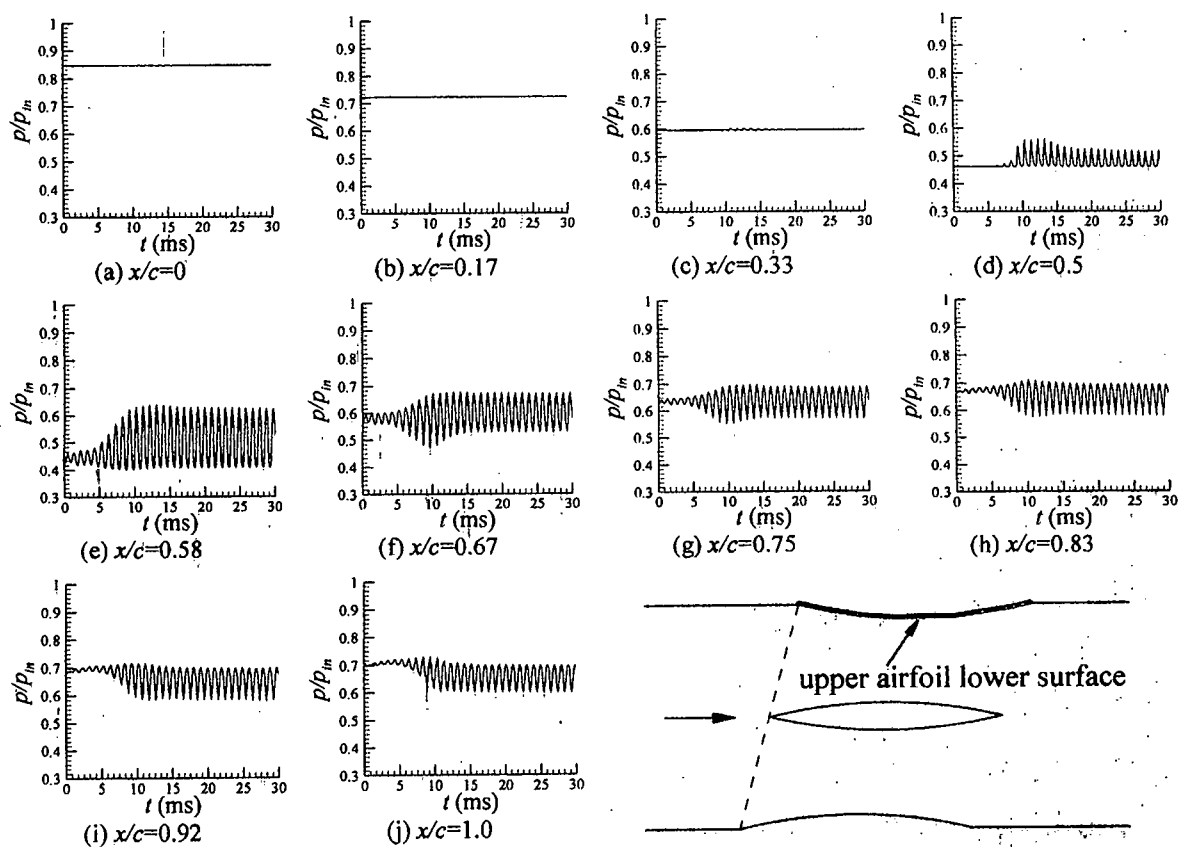


Figure 4.37 Static pressure-time histories in the flow field around an airfoil at different points on the upper airfoil lower surface for $PR=0.75$ (stagger angle, $\theta=15^\circ$)

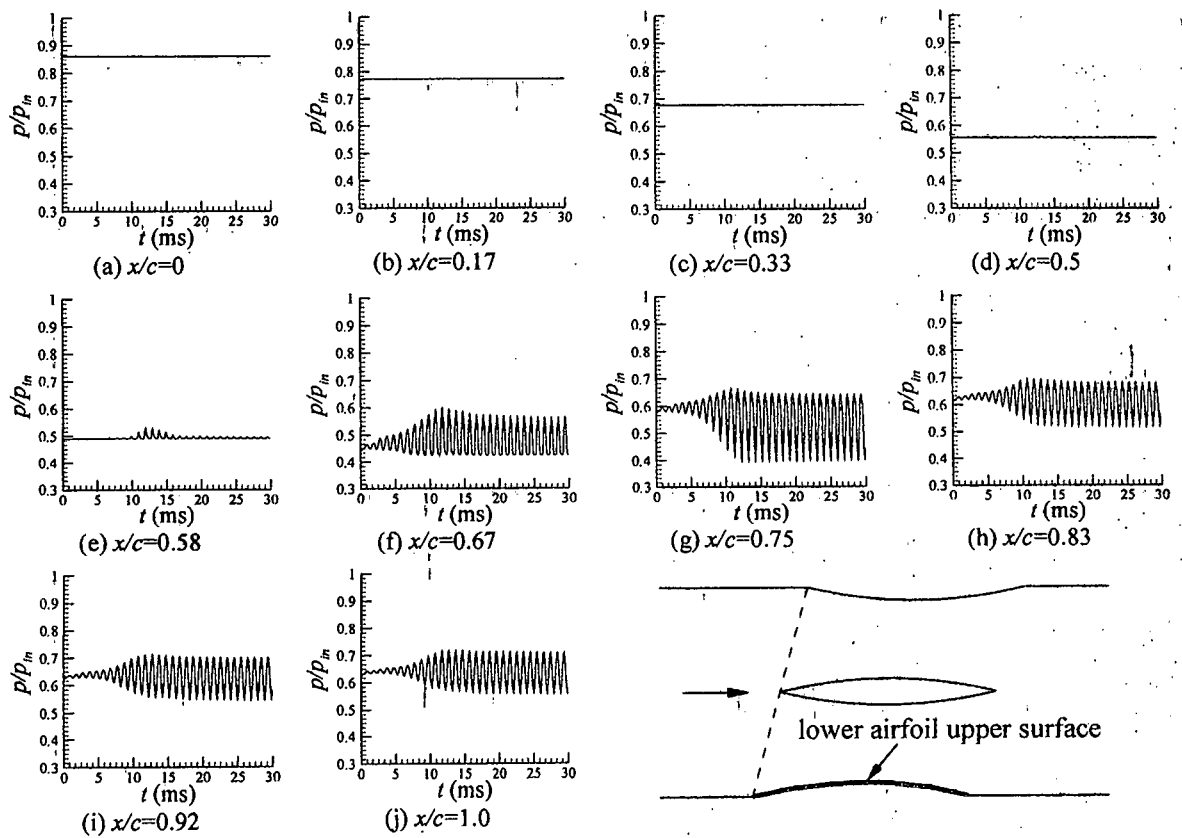


Figure 4.38 Static pressure-time histories in the flow field around an airfoil at different points on the lower airfoil upper surface for PR=0.75 (stagger angle, $\theta=15^\circ$)

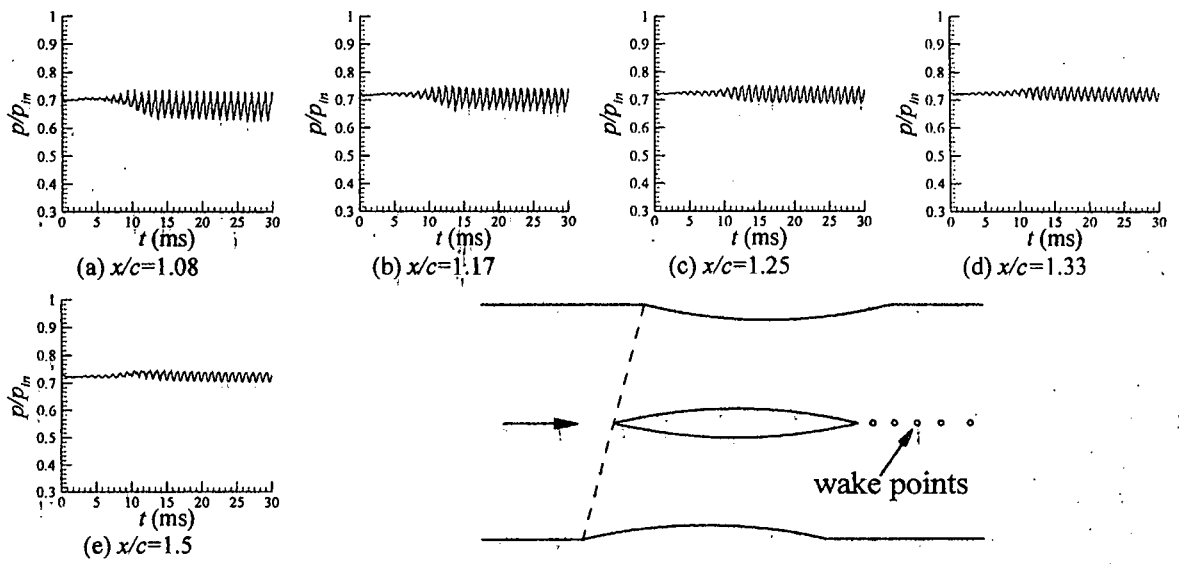


Figure. 4.39 Static pressure-time histories in the flow field around an airfoil at different points on the wake for $PR=0.75$ (stagger angle, $\theta=15^\circ$)

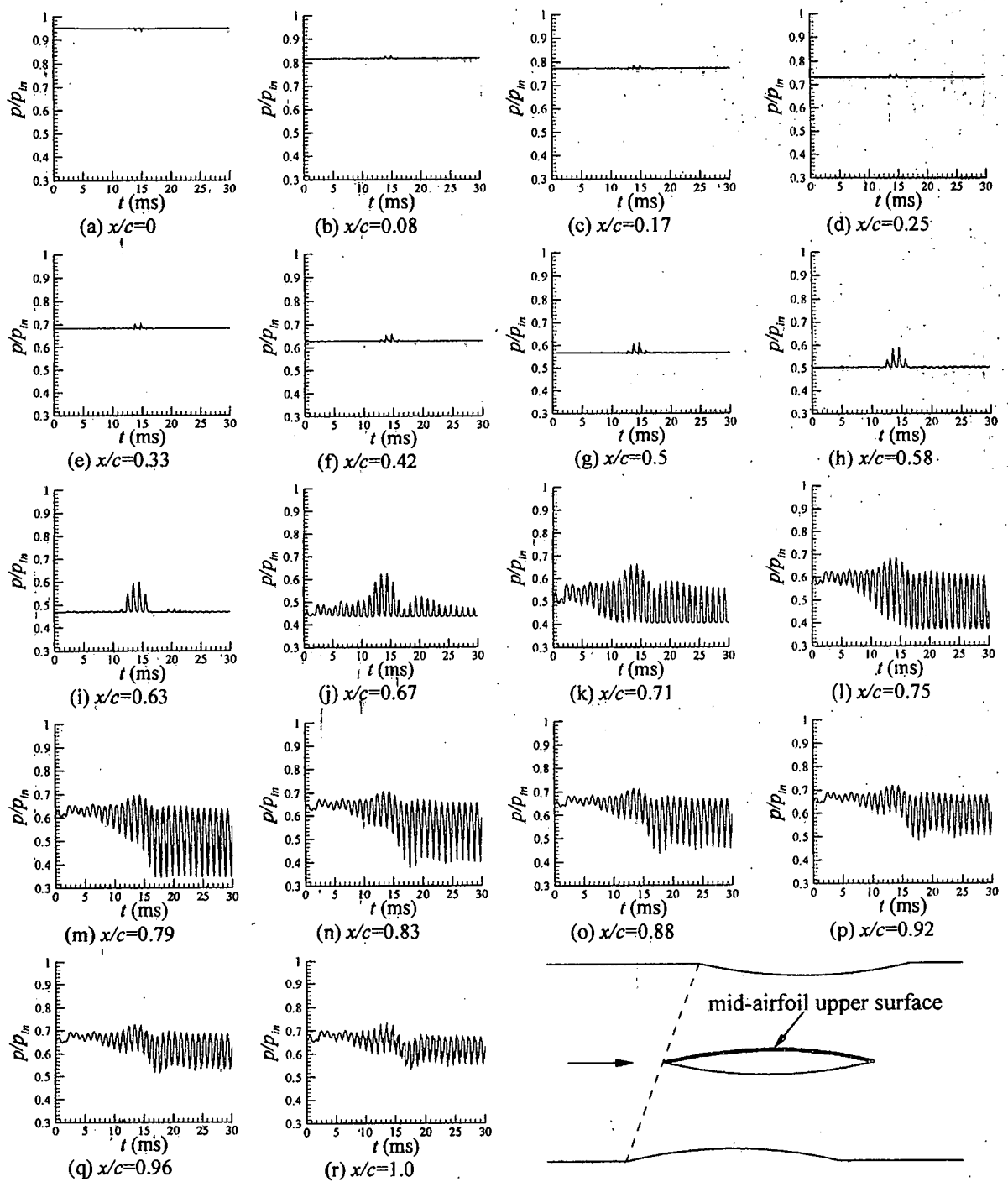


Figure. 4.40 Static pressure-time histories in the flow field around an airfoil at different points on the mid-airfoil upper surface for $PR=0.75$ (stagger angle, $\theta=20^\circ$)

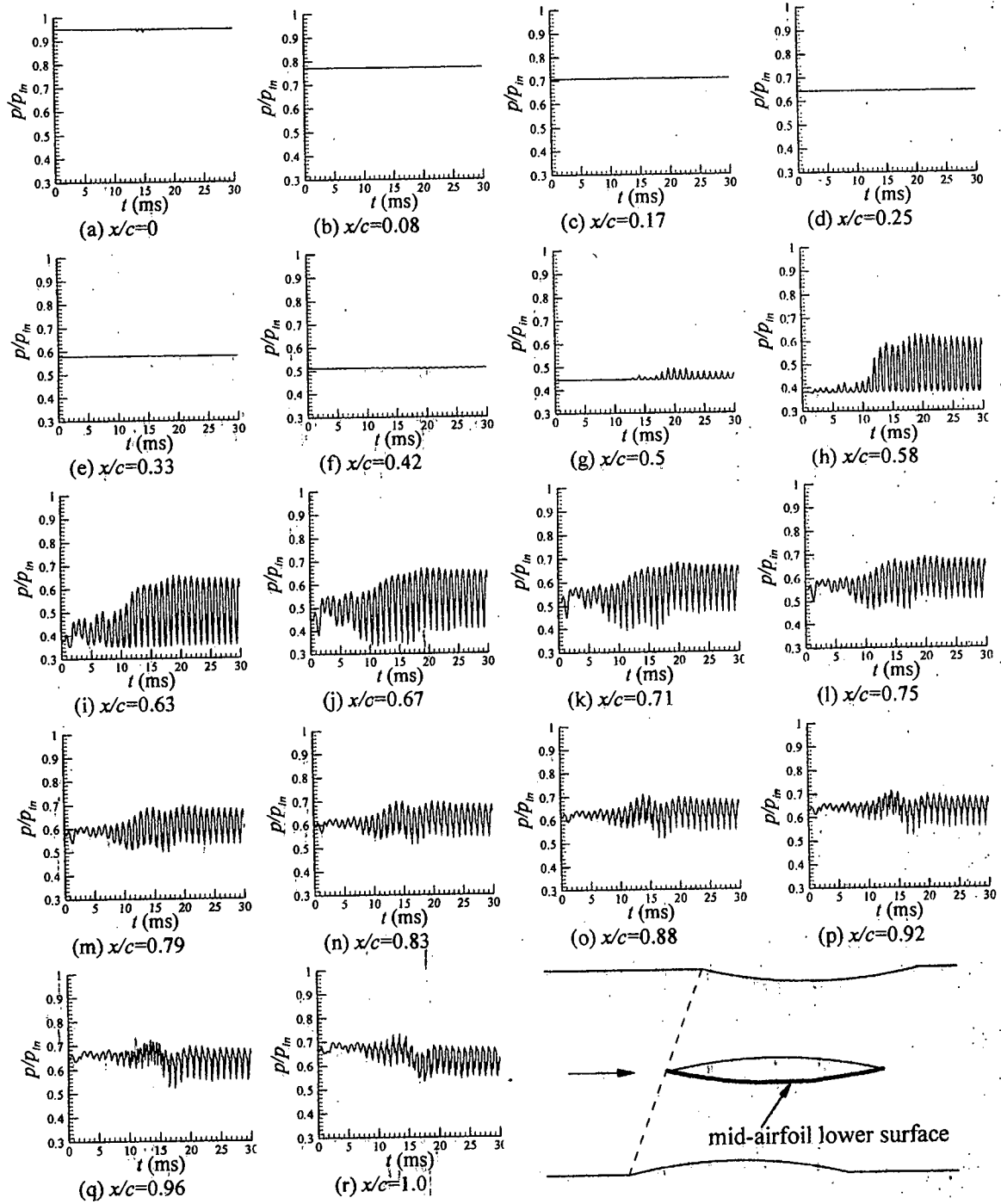


Figure. 4.41 Static pressure-time histories in the flow field around an airfoil at different points on the mid-airfoil lower surface for PR=0.75 (stagger angle, $\theta=20^\circ$)

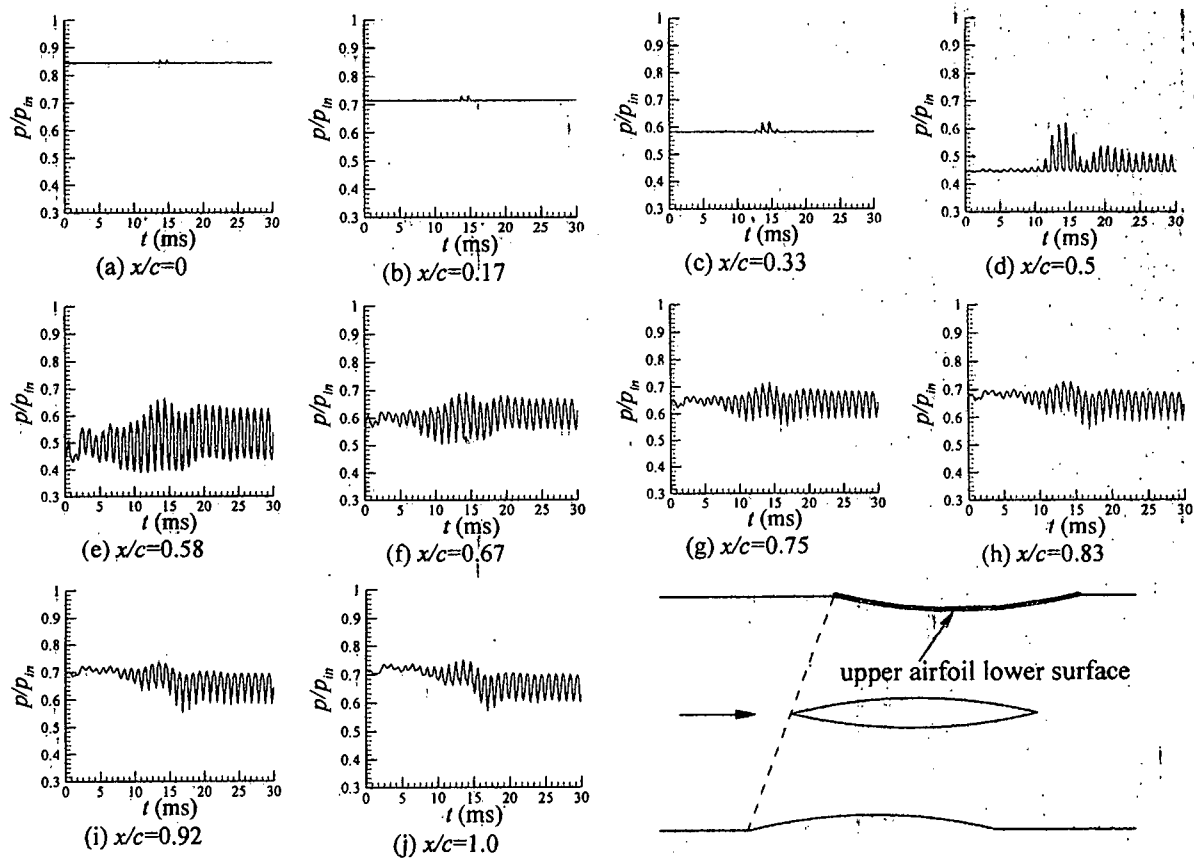


Figure. 4.42 Static pressure-time histories in the flow field around an airfoil at different points on the upper airfoil lower surface for $PR=0.75$ (stagger angle, $\theta=20^\circ$)

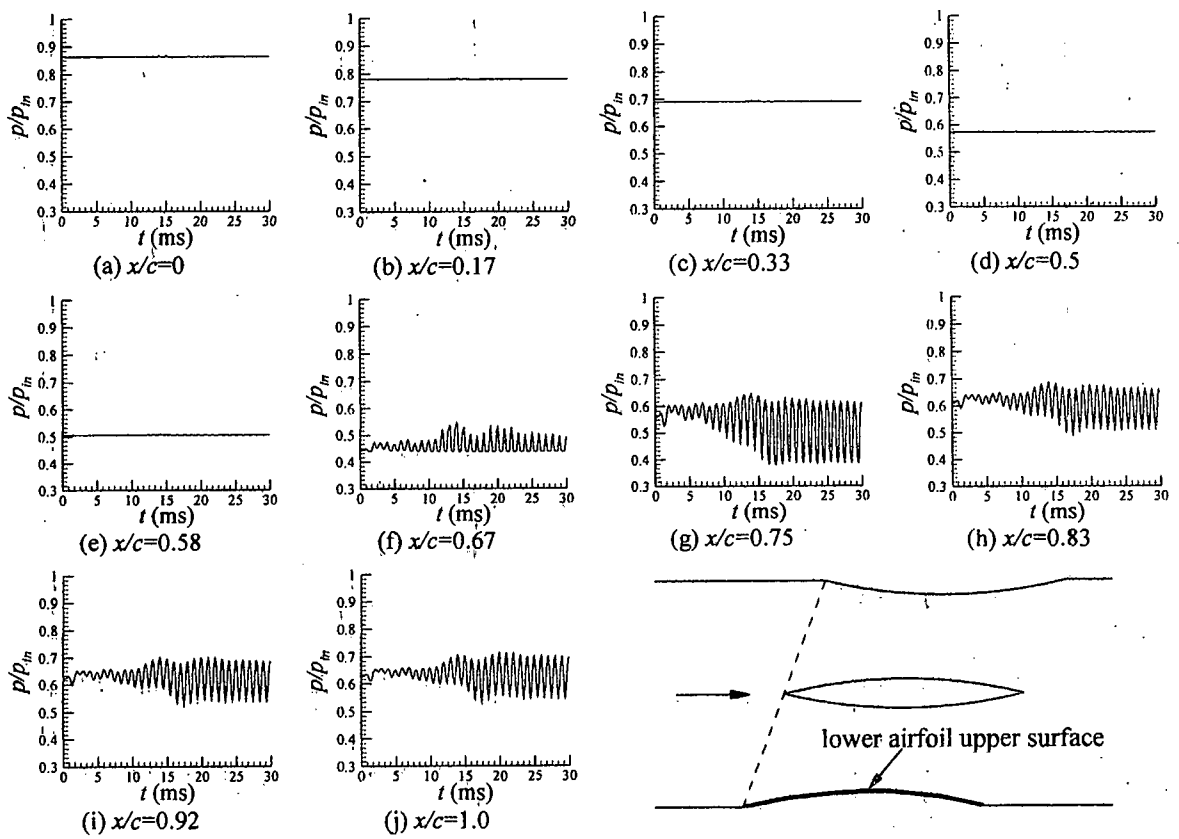


Figure 4.43 Static pressure-time histories in the flow field around an airfoil at different points on the lower airfoil upper surface for PR=0.75 (stagger angle, $\theta=20^\circ$)

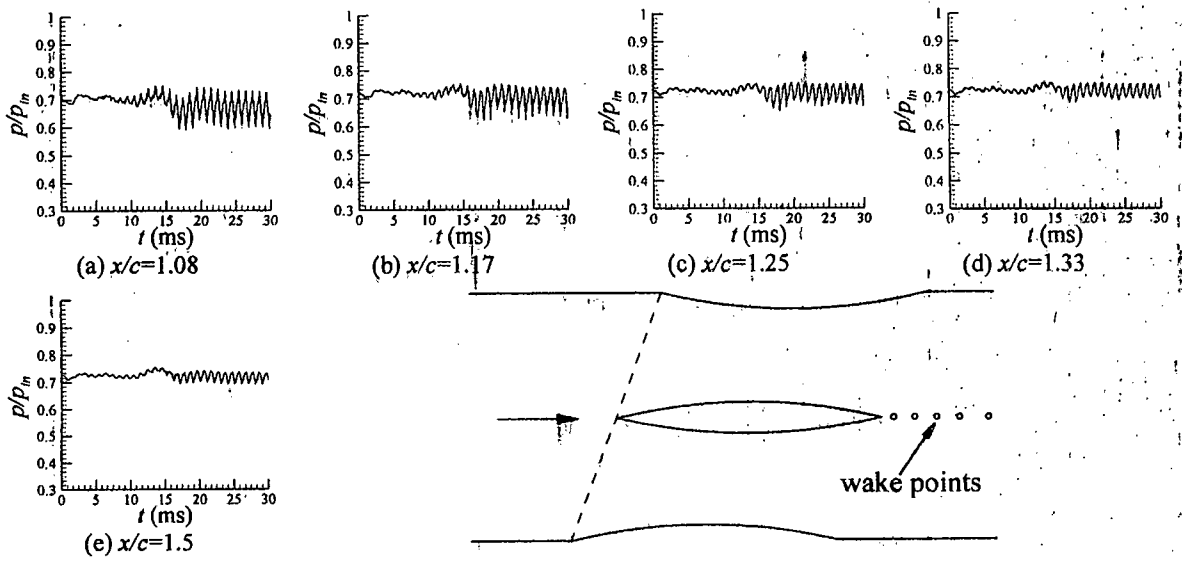


Figure. 4.44 Static pressure-time histories in the flow field around an airfoil at different points on the wake for $PR=0.75$ (stagger angle, $\theta=20^\circ$)

4.7 FFT

From unsteady pressure-time histories, it is not fully understandable whether these fluctuations are periodic with some definite frequency. Fast Fourier Transformation (FFT) is done with respective pressure data to find whether any dominating frequency exists and to find out what it is, FFT is an algorithm that computes the Discrete Fourier transform (DFT) of a sequence of data. The pressure data were in discrete form with a sampling frequency of 2×10^5 Hz, which is just the inverse of the time step size of the simulation. Power Spectral Density (PSD) was used to find the principal frequency of pressure fluctuation, which was found to be 976 Hz (figure. 4.45). Figures 4.45 to 4.54 show the existence of high frequency fluctuation. The frequency of these fluctuations is about 100 kHz. The position of the points corresponding to this higher frequency in the figures is after the re-attachment point.

Reduced frequency characterizes the variation of the flow with time. It is a dimensionless number used in general for the case of unsteady aerodynamics and aero-elasticity. It is one of the parameters that define the degree of unsteadiness of the problem. Reduced frequency characterizes the way a disturbance is felt at other points of the body. Since every point of an oscillating body disturbs the flow, one may say that the reduced frequency characterizes the mutual influence between the motions at various points of the body.

Reduced frequency is denoted by the letter " k " and is given by the expression,

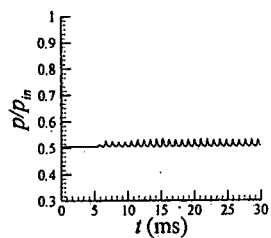
$$k = \frac{f c}{u_{\infty}} \quad (4.2)$$

f is the frequency of shock wave oscillation, c is the chord length and u_{∞} is the free stream velocity corresponding to different stagger angle.

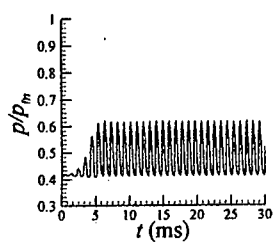
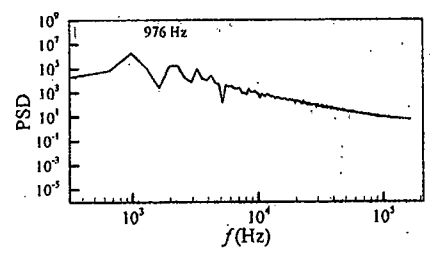
The frequency of shock oscillation is found to be 976 Hz, which gives the reduced frequency equal to 0.2670, 0.2672, 0.2678, 0.2688 and 0.2705 respectively for stagger angle 0° , 5° , 10° , 15° and 20° respectively as shown in the table. 4.1.

Table. 4.1 Reduced Frequency, (K) for different Stagger angle, (θ)

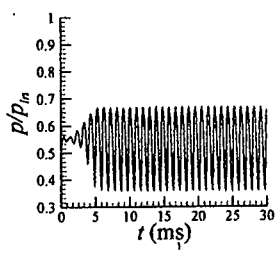
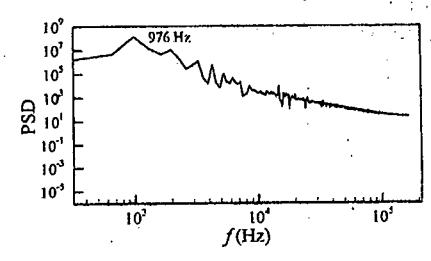
Stagger angle, (θ)	Reduced Frequency, (K)
0°	0.2670
5°	0.2672
10°	0.2678
15°	0.2688
20°	0.2705



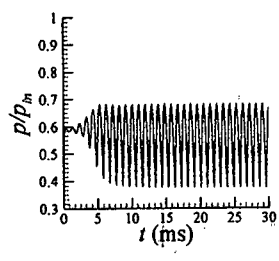
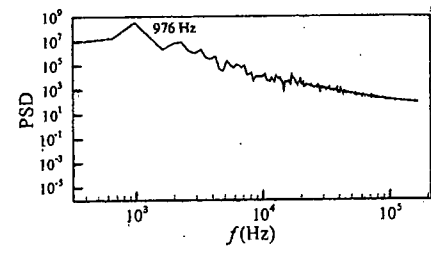
$x/c = 0.5$



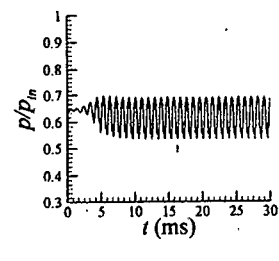
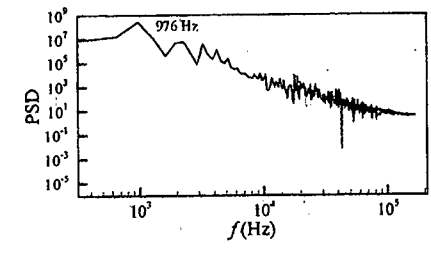
$x/c = 0.63$



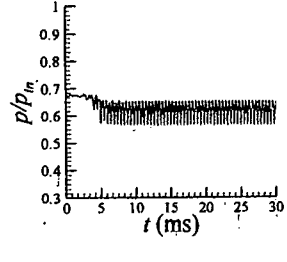
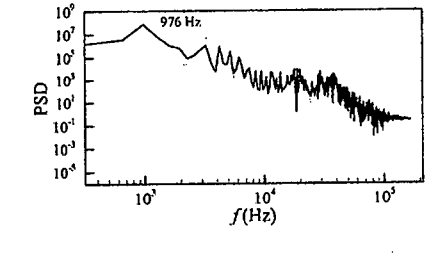
$x/c = 0.71$



$x/c = 0.75$



$x/c = 0.88$



$x/c = 1.0$

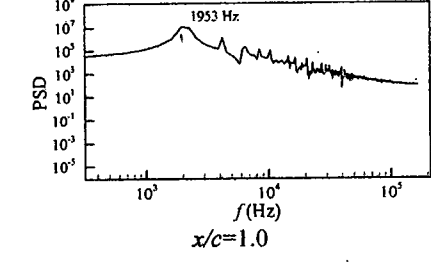


Figure. 4.45 Pressure-time histories and PSD vs. frequency curve for stagger angle $\theta=0^\circ$, PR=0.75 (mid-airfoil upper surface)

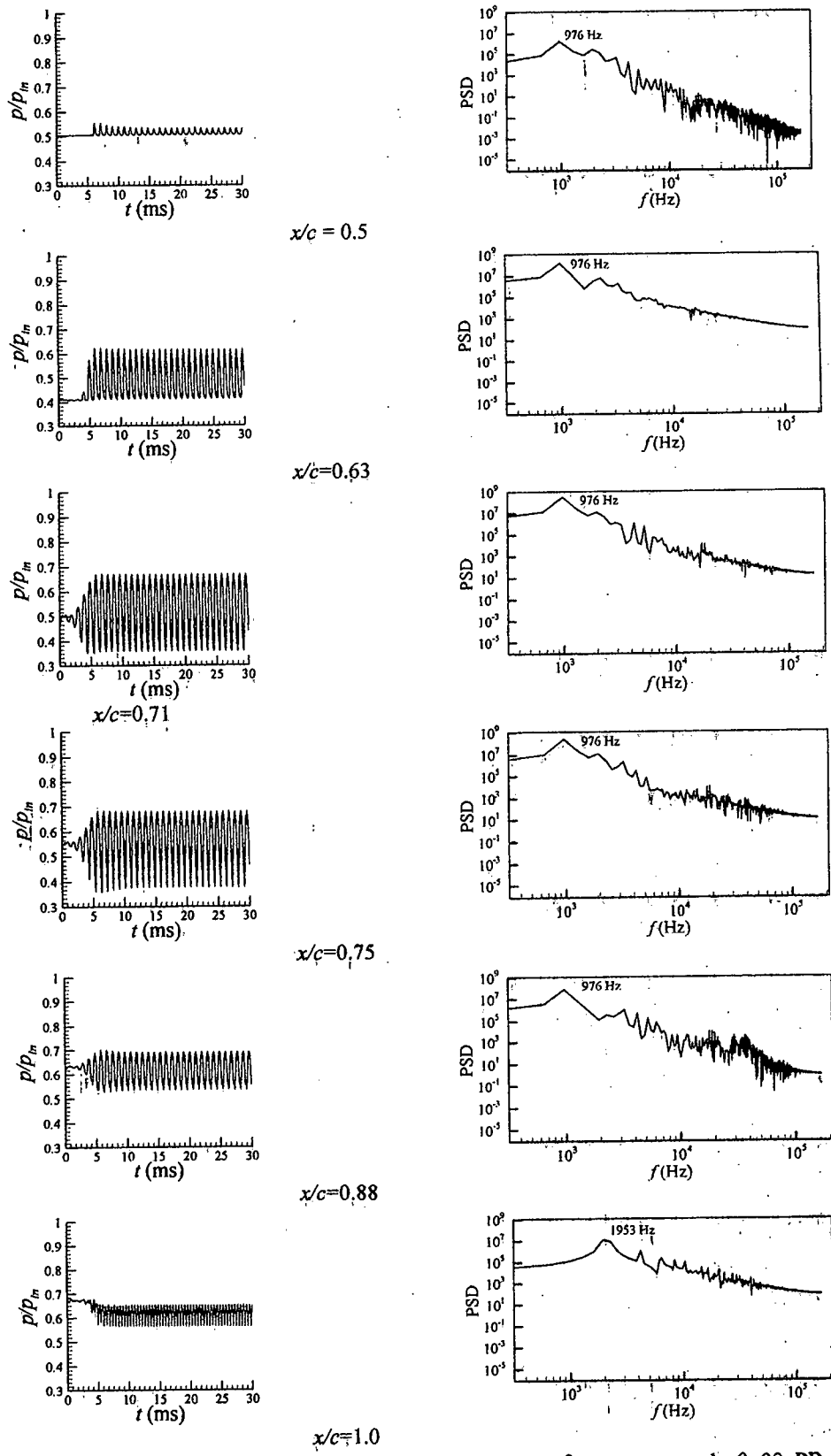
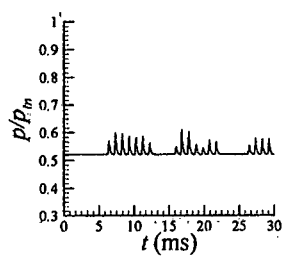
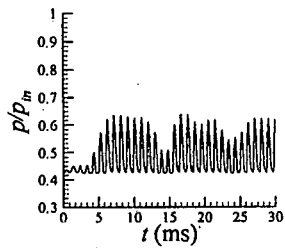
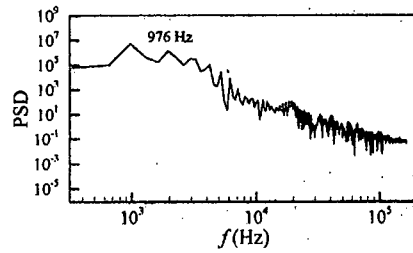


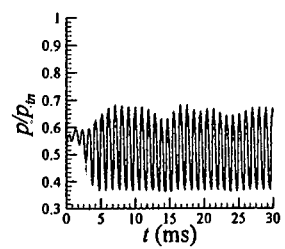
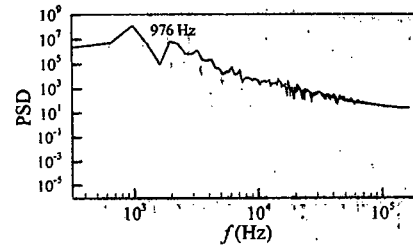
Figure. 4.46 Pressure-time histories and PSD vs. frequency for stagger angle $\theta=0^\circ$, PR=0.75 (mid-airfoil lower surface)



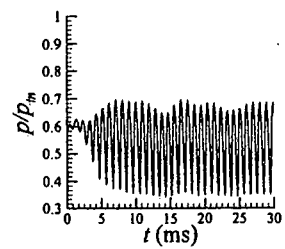
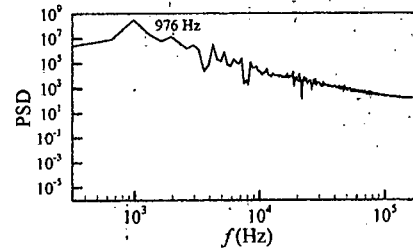
$x/c = 0.5$



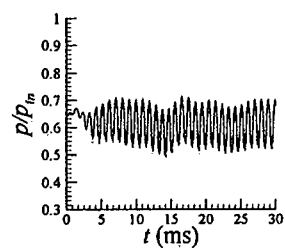
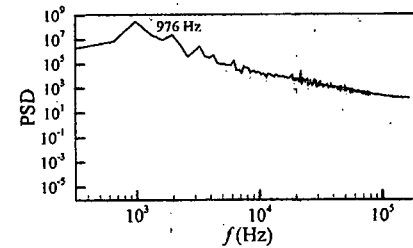
$x/c = 0.63$



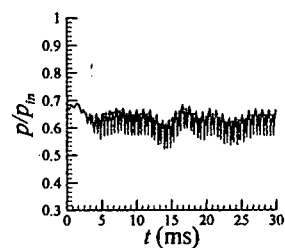
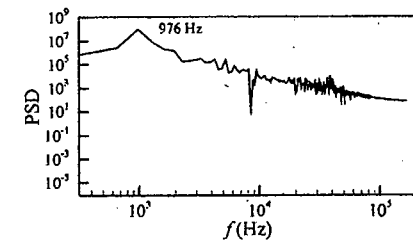
$x/c = 0.71$



$x/c = 0.75$



$x/c = 0.88$



$x/c = 1.0$

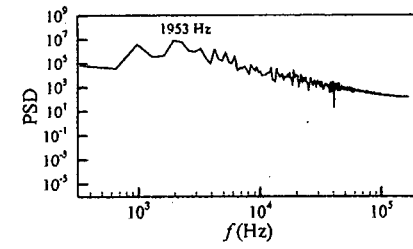
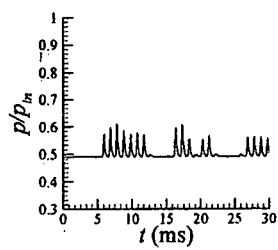
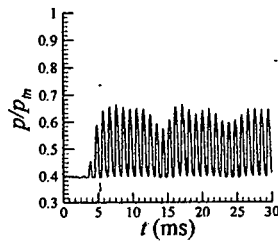
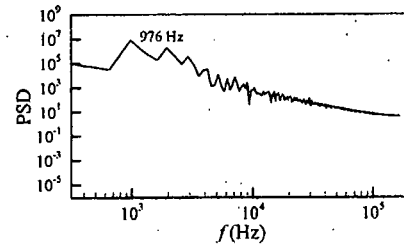


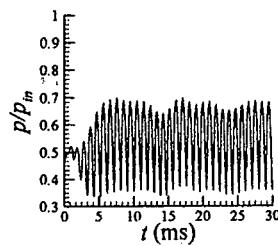
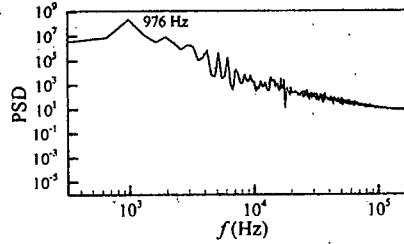
Figure. 4.47 Pressure-time histories and PSD vs. frequency curve for stagger angle $\theta=5^\circ$, $PR=0.75$ (mid-airfoil upper surface)



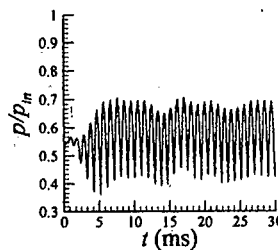
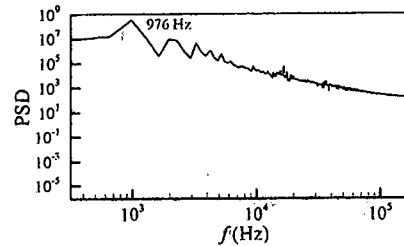
$x/c = 0.5$



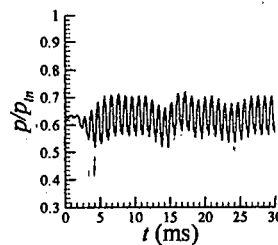
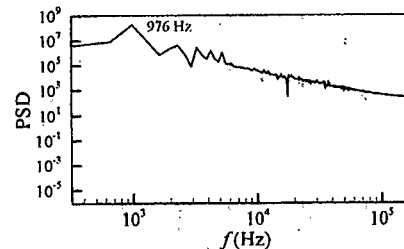
$x/c = 0.63$



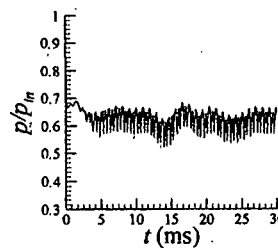
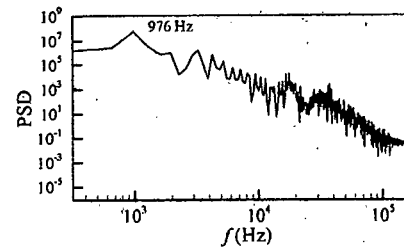
$x/c = 0.71$



$x/c = 0.75$



$x/c = 0.88$



$x/c = 1.0$

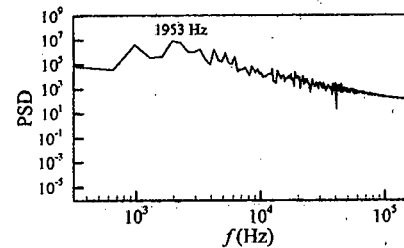
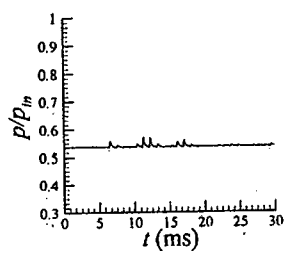
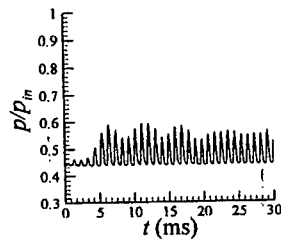
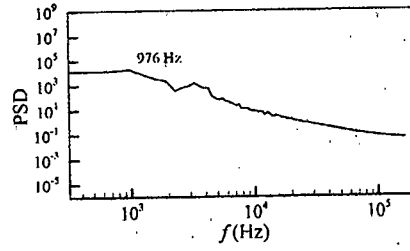


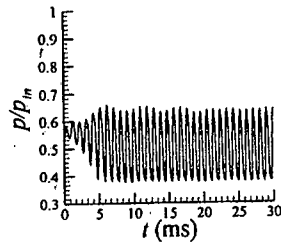
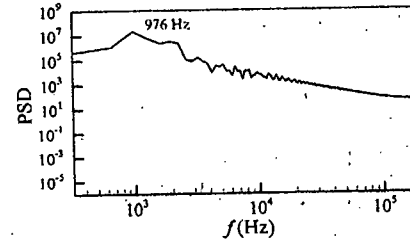
Figure. 4.48 Pressure-time histories and PSD vs. frequency curve for stagger angle $\theta=5^\circ$, PR=0.75 (mid-airfoil lower surface)



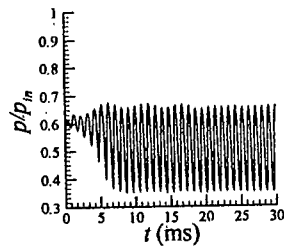
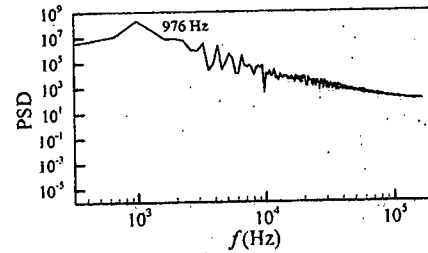
$x/c = 0.5$



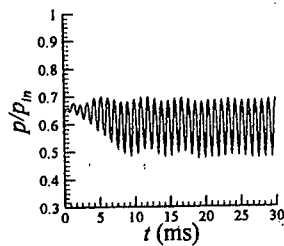
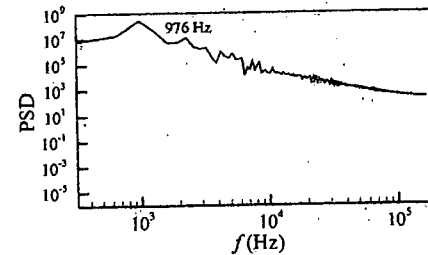
$x/c = 0.63$



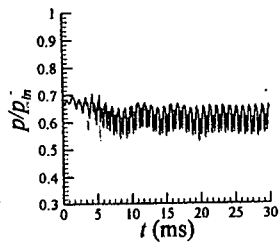
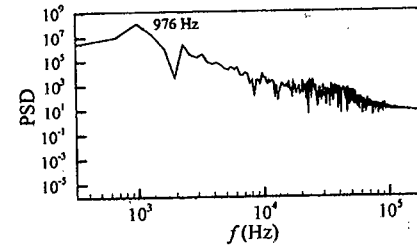
$x/c = 0.71$



$x/c = 0.75$



$x/c = 0.88$



$x/c = 1.0$

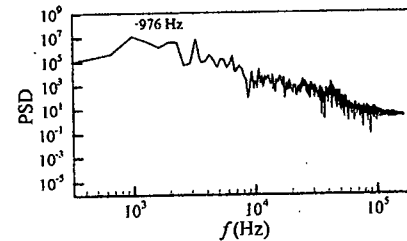
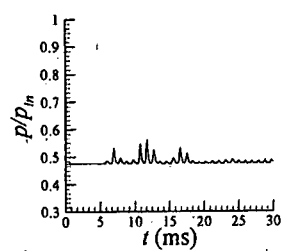
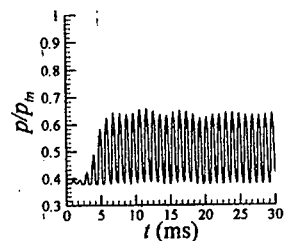
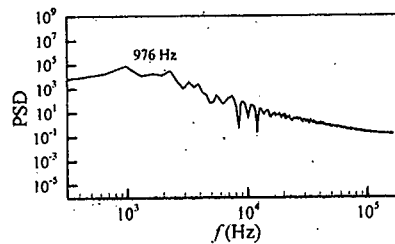


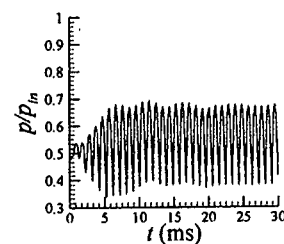
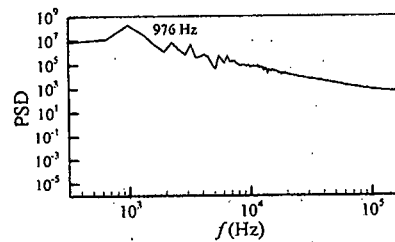
Figure. 4.49 Pressure-time histories and PSD vs. frequency curve for stagger angle $\theta=10^\circ$, PR=0.75 (mid-airfoil upper surface)



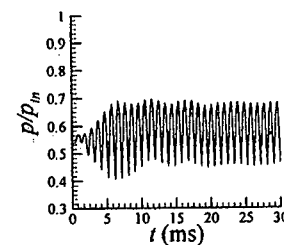
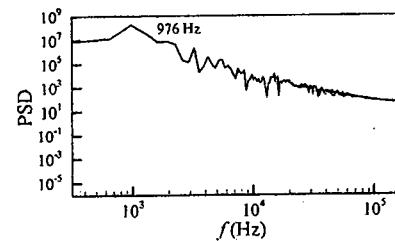
$x/c = 0.5$



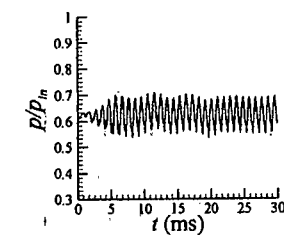
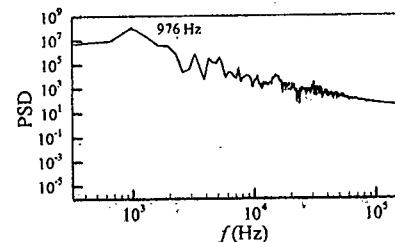
$x/c = 0.63$



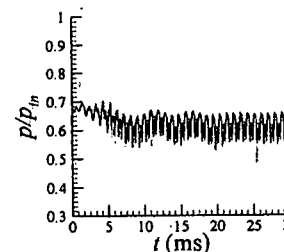
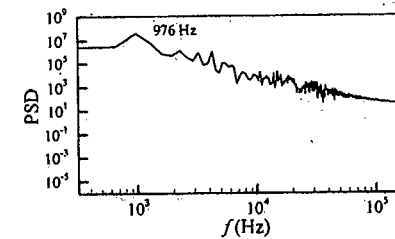
$x/c = 0.71$



$x/c = 0.75$



$x/c = 0.88$



$x/c = 1.0$

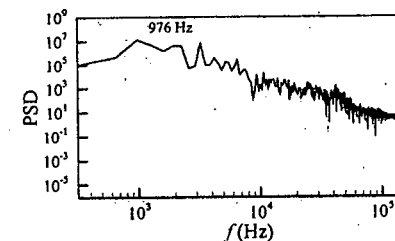
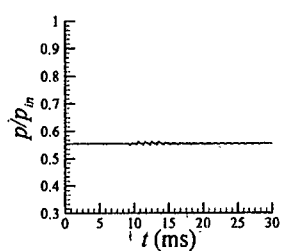
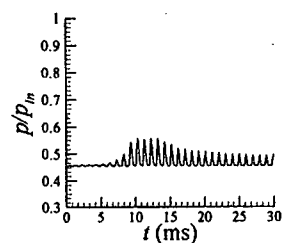
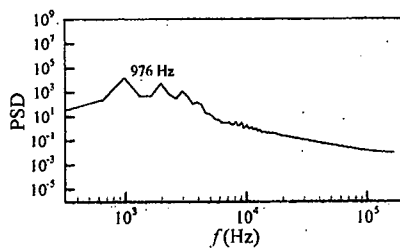


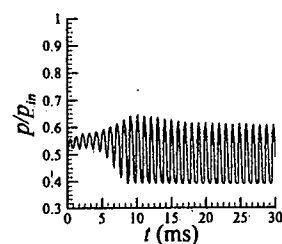
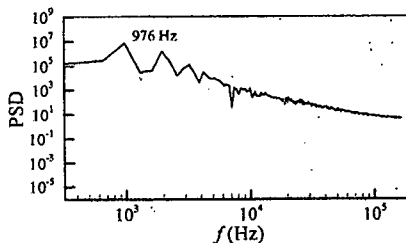
Figure 4.50 Pressure-time histories and PSD vs. frequency curve for stagger angle $\theta = 10^\circ$, $PR = 0.75$ (mid-airfoil lower surface)



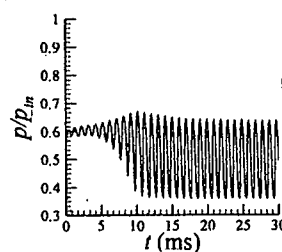
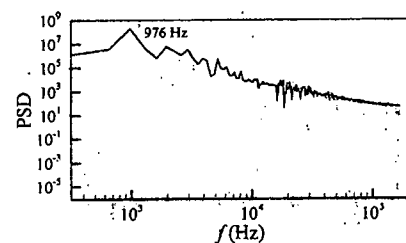
$x/c = 0.5$



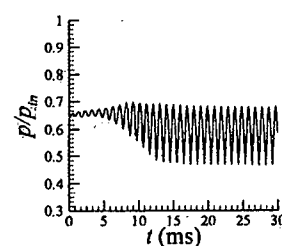
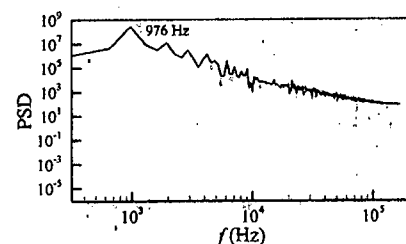
$x/c = 0.63$



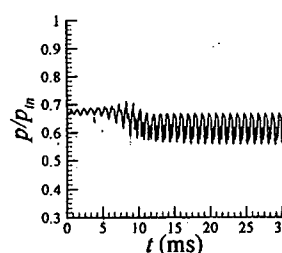
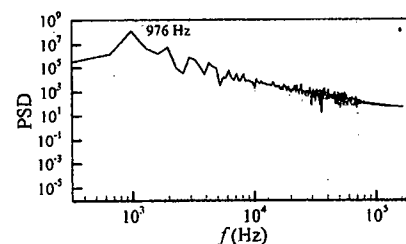
$x/c = 0.71$



$x/c = 0.75$



$x/c = 0.88$



$x/c = 1.0$

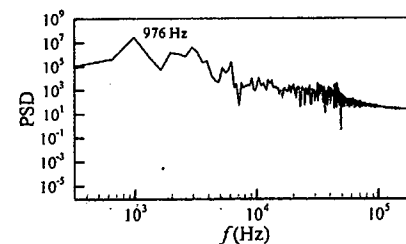
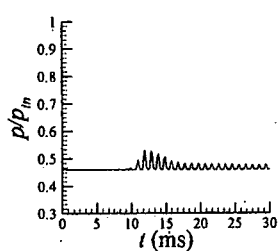
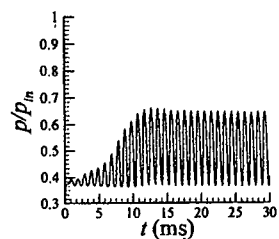
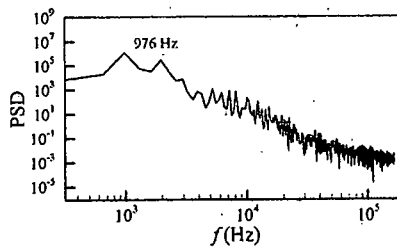


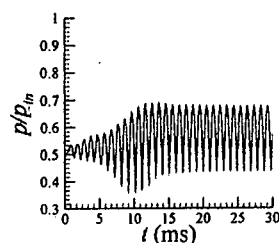
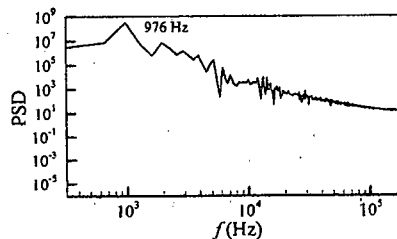
Figure. 4.51 Pressure-time histories and PSD vs. frequency curve for stagger angle $\theta=15^\circ$, PR=0.75 (mid-airfoil upper surface)



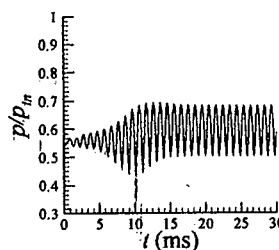
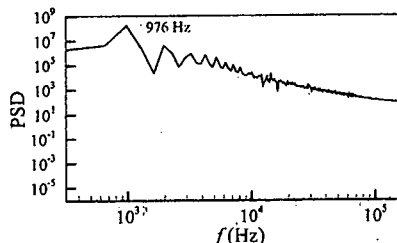
$x/c = 0.5$



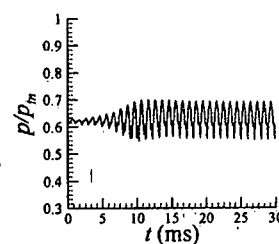
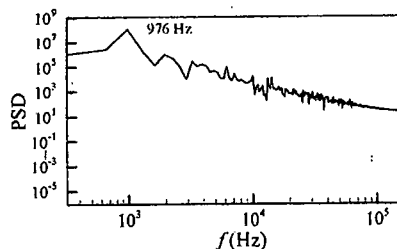
$x/c = 0.63$



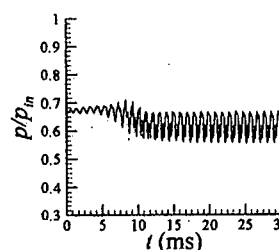
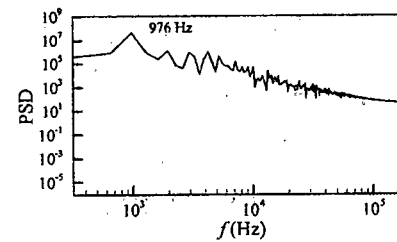
$x/c = 0.71$



$x/c = 0.75$



$x/c = 0.88$



$x/c = 1.0$

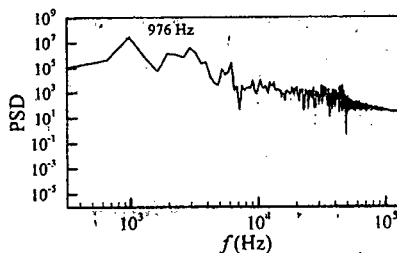
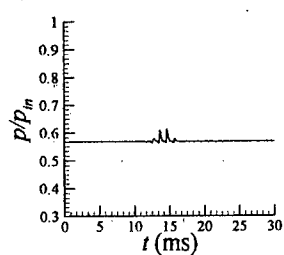
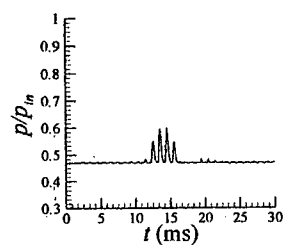
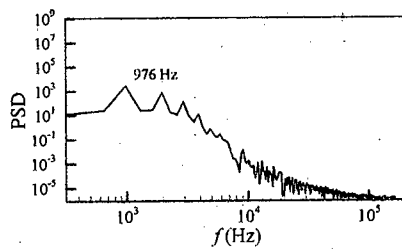


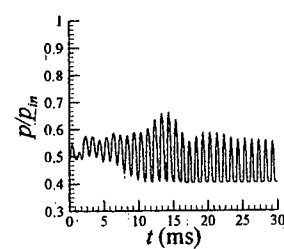
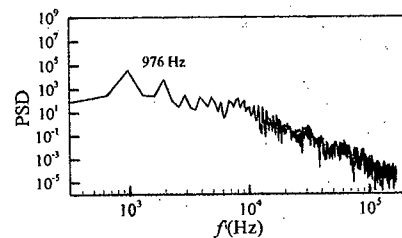
Figure 4.52 Pressure-time histories and PSD vs. frequency curve for stagger angle $\theta=15^\circ$, PR=0.75 (mid-airfoil lower surface)



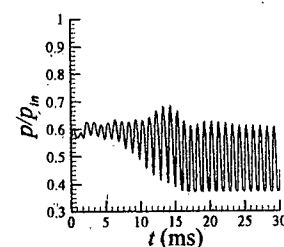
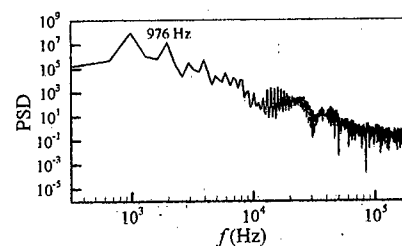
$x/c = 0.5$



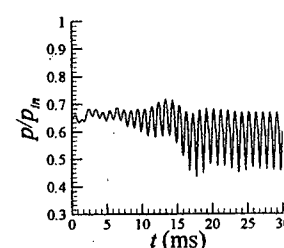
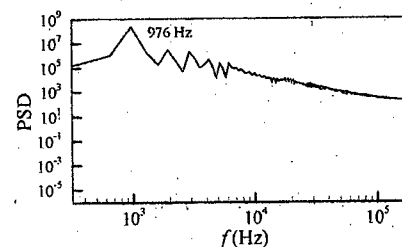
$x/c = 0.63$



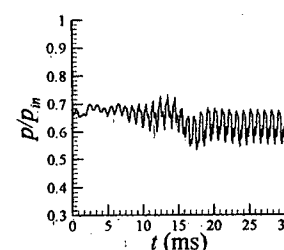
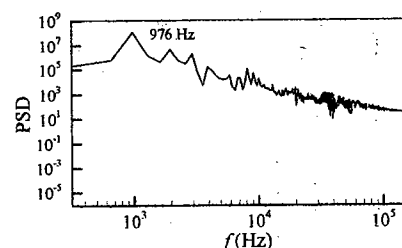
$x/c = 0.71$



$x/c = 0.75$



$x/c = 0.88$



$x/c = 1.0$

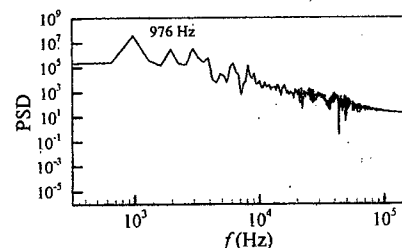
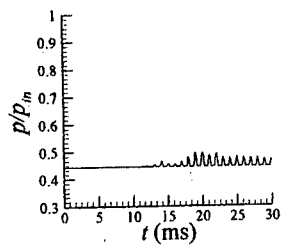
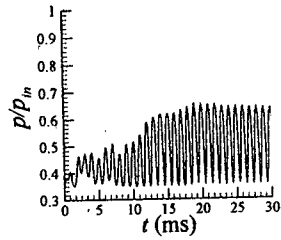
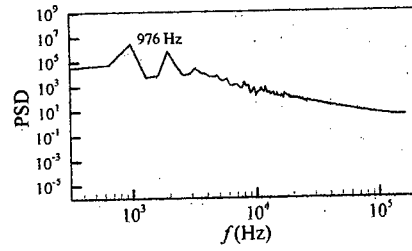


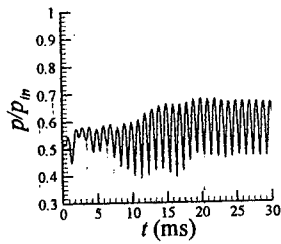
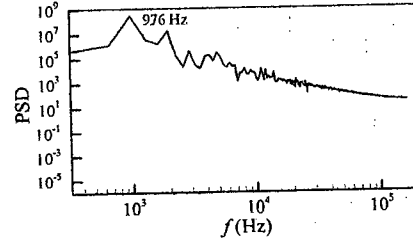
Figure. 4.53 Pressure-time histories and PSD vs. frequency curve for stagger angle $\theta=20^\circ$, PR=0.75 (mid-airfoil upper surface)



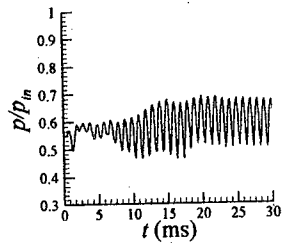
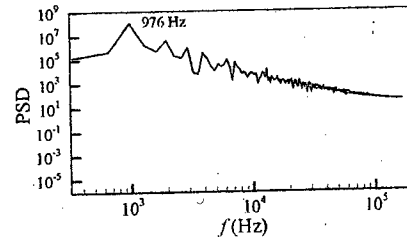
$x/c = 0.5$



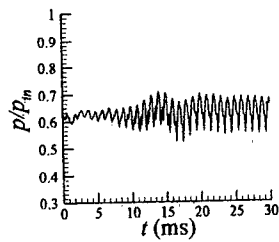
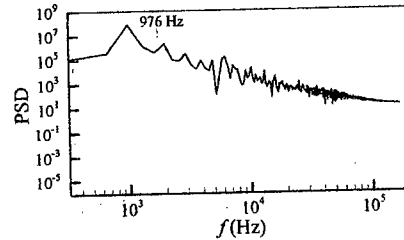
$x/c = 0.63$



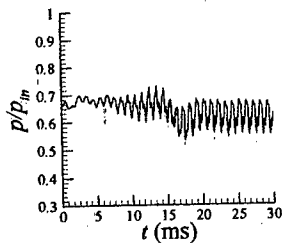
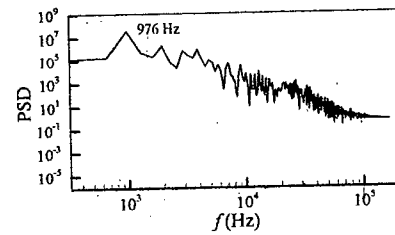
$x/c = 0.71$



$x/c = 0.75$



$x/c = 0.88$



$x/c = 1.0$

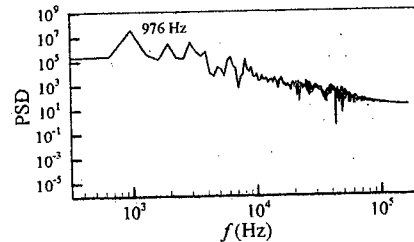


Figure. 4.54 Pressure-time histories and PSD vs. frequency curve for stagger angle $\theta = 20^\circ$, PR=0.75 (mid-airfoil lower surface)

4.8 P_{rms}/q_0

The flow field aerodynamic instability around the airfoil cascade can conveniently be expressed by the distribution of root means square (RMS) value of pressure oscillation induced by shock wave oscillation. The RMS of pressure oscillation, p_{rms} is calculated as

$$p_{rms} = \sqrt{\sum_{i=1}^n (p_i - \bar{p})^2 / n} \quad \text{Where, } \bar{p} = \sum_{i=1}^n p_i / n \quad (4.3)$$

In the above equation, p_i and \bar{p} are the instantaneous and mean static pressures respectively. The results are calculated from sampling points, $n=10^4$ and 10 cycles. Here, p_{rms} is RMS of pressure oscillation and q_0 is the dynamic pressure of the free stream of the airfoil cascade. Figure. 4.55 shows the distributions of RMS value of the pressure oscillation p_{rms}/q_0 on the mid-airfoil upper surface, mid-airfoil lower surface, upper airfoil lower surface and lower airfoil upper surface for five different stagger angle $\theta=0^\circ, 5^\circ, 10^\circ, 15^\circ$ and 20° . Here, p_{rms}/q_0 at wake region is shown for mid-airfoil upper and lower surface only. It is observed that for all the cases, the flow field remains undisturbed before $x/c=0.5$ from leading edge, as in that portion no shock wave is observed on the airfoil surfaces.

For stagger angle $\theta=0^\circ$, p_{rms}/q_0 starts to increase from $x/c=0.5$ and shows a peak value of 0.667 at $x/c=0.71$ on the mid-airfoil upper surface and a peak value of 0.68 at $x/c=0.71$ on the mid-airfoil lower surface. These peak values signify a large pressure fluctuation and intensity at this location. Further movement towards downstream shows a gradual drop of p_{rms}/q_0 . At the trailing edge, p_{rms}/q_0 slightly increases. After that, p_{rms}/q_0 again decreases along the wake region. For stagger angle 5° , the maximum value of p_{rms}/q_0 is 0.68 at $x/c=0.75$ on mid-airfoil upper surface and 0.687 at $x/c=0.67$ on mid-airfoil lower surface. For stagger angle $\theta=10^\circ, 15^\circ$ and 20° peak p_{rms}/q_0 is 0.69, 0.657, 0.586 respectively at $x/c=0.75$ on the mid-airfoil upper surface and 0.688, 0.682, 0.652 at $x/c=0.67, 0.625, 0.625$ respectively on the mid-airfoil lower surface. With the increase in stagger angle from 0 to 20 deg on the mid-airfoil upper surface p_{rms}/q_0 first increases from 0.667 to 0.69 and then decreases to 0.586 and the location is shifted from $x/c=0.71$ to 0.75 (towards downstream). In case of mid-airfoil lower surface, similarly, p_{rms}/q_0 first increases from 0.68 to 0.688 and then decreases to 0.652 and the location is shifted towards upstream (from $x/c=0.71$ to $x/c=0.625$).

Table. 4.2 Maximum values of p_{rms}/q_0 and the corresponding locaitons on mid-airfoil upper and mid-airfoil lower surface

Stagger angle, θ	Mid-airfoil upper surface		Mid-airfoil lower surface	
	Maximum p_{rms}/q_0	Location, x/c (for max p_{rms}/q_0)	Maximum p_{rms}/q_0	Location, x/c (for max p_{rms}/q_0)
0°	0.667	0.71	0.68	0.71
5°	0.68	0.75	0.687	0.67
10°	0.69	0.75	0.688	0.67
15°	0.657	0.75	0.682	0.625
20°	0.586	0.75	0.652	0.625

Table. 4.3 Maximum values of p_{rms}/q_0 and the corresponding locaitons on upper airfoil lower and lower airfoil upper surface

Stagger angle, θ	Upper airfoil lower surface		Lower airfoil upper surface	
	Maximum p_{rms}/q_0	Location, x/c (for max p_{rms}/q_0)	Maximum p_{rms}/q_0	Location, x/c (for max p_{rms}/q_0)
0°	0.558	0.667	0.564	0.667
5°	0.559	0.667	0.547	0.667
10°	0.475	0.583	0.499	0.75
15°	0.538	0.583	0.547	0.75
20°	0.471	0.583	0.493	0.75

For stagger angle 0° and 5°, from peak p_{rms}/q_0 position to trailing edge, the value of p_{rms}/q_0 gradually decreases but at 95% c this value increases a small amount upto trailing edge and again decreases gradually. At higher stagger angle ($\theta=10^\circ, 15^\circ$ and 20°) first the value of p_{rms}/q_0 gradually increases to peak value and after that it decreases and at 93% c this value increases slightly at the trailing edge and then decreases gradually. This phenomenon is observed due to vortex formation and interaction with the trailing edge. These peak RMS values and corresponding locations are shown in Table. 4.2. In table 4.3 maximum values of p_{rms}/q_0 and corresponding location on the upper airfoil lower surface and lower airfoil upper surface have been shown. With the increase in stagger angle, position of peak RMS of pressure oscillation is shifted upstream on the upper airfoil lower surface and downstream on the lower airfoil upper surface. On both surfaces small amount of decrease of the magnitude of peak RMS of pressure oscillation is observed at $\theta=10^\circ$ and 20° .

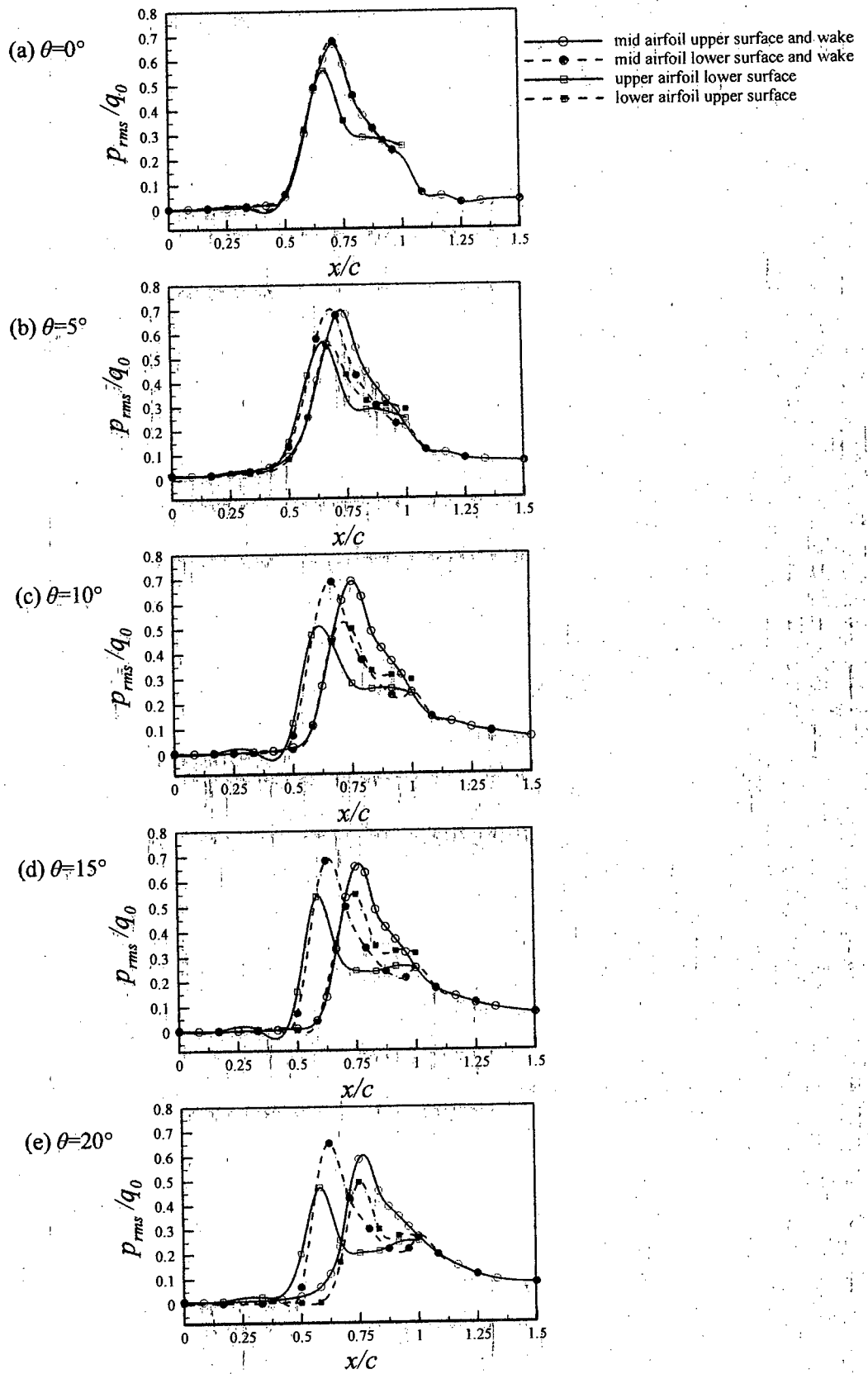


Figure. 4.55 RMS pressure fluctuation over cascade surfaces

4.9 BOUNDARY LAYER SEPARATION CHARACTERISTICS

Boundary layer separation is the detachment of a boundary layer from the surface. Boundary layer separation occurs when the portion of the boundary layer closest to the wall reverses in flow direction. When the entire flow is subsonic, if the low-pressure region is followed by a high pressure region then the boundary layer may separate. On the other hand, when the flow around the inlet is partly supersonic, the local supersonic region will usually end abruptly in a shock, and the shock-wall interaction may cause boundary layer separation. The separation point is defined as the point between the forward and backward flow, where the shear stress is zero. The point where the separated flow attaches to the wall again is called the reattachment point, at this point also the shear stress is found zero.

Separation length (L_{sep}) in x -direction is calculated along the horizontal distance from separation point to reattachment point up to which the x -shear stress has negative value. y_{sep} indicates the flow separation along y -direction as observed in corresponding velocity profile.

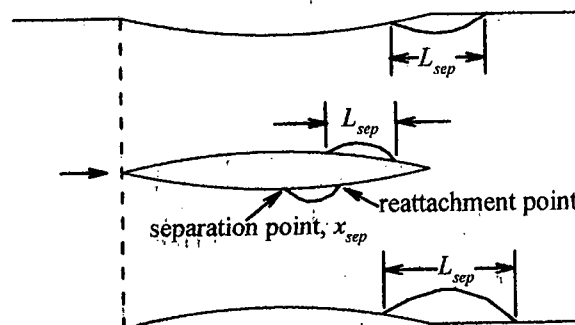


Figure. 4.56 Cascade with separation point and separation length

Figure. 4.57 shows the velocity profile at different locations on the mid-airfoil upper surface for $\theta=0^\circ$ and $t/T=0$. Here, x -velocity distributions have been shown with respect to y -direction at five different locations in the same figure. For each of the curves the local x -velocity is expressed as u and u_0 is the first maximum x -velocity along y -direction. u/u_0 varies from 0 to 1 (for brevity all the curves have been shown in the same figure and the corresponding value ranges from 0 to 5) if there is no flow separation. Negative values of u/u_0 express the presence of flow separation.

In figure 4.57 five curves have been drawn, among them first curve represent a location ($x/c=0.5$) where there is no flow separation, second ($x/c=0.85$) and third ($x/c=0.9$) curves represent a location where the flow is separated and fourth curve represents a location ($x/c=0.985$) where the flow is reattached and the fifth curve is at trailing edge ($x/c=1$) where flow is not separated. At $x/c=0.85$ and 0.9 flow separation exists along y -direction and the separation lengths are $y_{sep}=0.000252$ and 0.00117 respectively as shown in the enlarged figures (figure 4.58). At $x/c=0.985$ the shock reattaches and in this case no separation is observed.

Similarly, figure. 4.59 shows the velocity profile at different locations on the mid-airfoil lower surface for $\theta=0^\circ$ and $t/T=0$. In this case, at $x/c=0.5$ flow is not separated. At $x/c=0.85$ and 0.9 flow

separation occurred and at $x/c=0.985$ flow again reattaches. At the trailing edge ($x/c=1$) flow has been separate. At $x/c=0.85$ separation length along y-direction $y_{sep}=0.0071$ and at $x/c=0.9$ separated length y_{sep} is found to be 0.00976 (figure. 4.60).

Figure. 4.61 shows the separation start point (x_{sep}/c) and separation length (L_{sep}/c) in a cycle for stagger angle $\theta=0^\circ$ to 20° at mid-airfoil upper surface (solid line with white circle), mid-airfoil lower surface (dotted line with black circle), upper airfoil lower surface (solid line with white square) and lower airfoil upper surface (dotted line with black square). At $\theta=0^\circ$ and $t/T=0$ on mid-airfoil upper surface separation starts at $x_{sep}/c=0.76$ (figure 4.61(a)) and separation length is $L_{sep}/c=0.234$ (figure 4.61(b)). In the same instant shock wave was present at $x/c=0.73$. So, the separation occurred after the shock. At time $t/T=0.125$, separation point is $x_{sep}/c=0.72$ separation length is $L_{sep}/c=0.249$ and the shock is present at $0.69c$. At time $t/T=0.25$ separation starts at $x_{sep}/c=0.673$ and the length of separation is $L_{sep}/c=0.29$. In this case shock was present on the same surface at $0.651c$. So, it can be said that separation can occur with interaction of shock and wall or if low pressure region is followed by a high pressure region. In the next time step, at $t/T=0.375$ separation point is at $x_{sep}/c=0.624$, separation length is $0.346c$ and shock wave location is at $0.582c$. After that, at $t/T=0.5$ separation point shifted to $0.822c$, the separation length is $0.155c$ and shock is present at $0.56c$. At $t/T=0.625$, no shock wave is seen on the mid-airfoil upper surface and also there is no separation and the separation length is zero. At $t/T=0.75$ and 0.875 separation is noticed at $x_{sep}/c=0.95$ and 0.85 separation length is $0.05c$ and $0.14c$ respectively. In these two steps no shock is observed on the mid-airfoil upper surface. So separation is occurred may be due to interaction with trailing edge. In the next time step cycle starts again.

In case of mid-airfoil lower surface ($\theta=0^\circ$) separation starts at $t/T=0$ at $x_{sep}/c=0.825$ (shock wave is present at $X_s=0.56c$) and separation length is $0.153c$. In the next time step, there is no shock wave and so, no separation is noticed. From $t/T=0.25$ to 0.875 separation point gradually comes towards upstream from $x_{sep}/c=0.95$ to 0.62 and the separation length increases from $0.05c$ to $0.35c$ as the shock wave move upstream from $0.73c$ to $0.58c$.

On the upper airfoil lower surface for $\theta=0^\circ$ separation starts at $t/T=0$ at $x_{sep}/c=0.721$ with a separation length of 0.688 (figure. 4.61 (a),(b)). From time step $t/T=0.125$ to 0.375 separation starting point (x_{sep}/c) moves upstream from $0.697c$ to $0.624c$ and in this period separation length (L_{sep}/c) increases from $0.71c$ to $0.89c$. At $t/T=0.5$ separation occurs at $0.77c$ and separation length is $0.785c$. After that from $t/T=0.625$ to 0.875 separation point moves upstream from $0.776c$ to $0.751c$ the corresponding separation lengths are $0.633c$, $0.238c$ and $0.529c$.

In case of lower airfoil upper surface for $\theta=0^\circ$ separation starts at $t/T=0$ at $x_{sep}/c=0.775$ and separation point gradually moves upstream up to $x_{sep}/c=0.623$ ($t/T=0.875$). In this time duration the separation length first decreases from $0.779c$ to $0.239c$ and then increases to $0.931c$ and the cycle repeats.

Figure. 4.61 (c), (d) shows the separation start point and separation length respectively for stagger angle 5° . On the mid-airfoil upper surface, separation starts at $0.80c$ at $t/T=0$ and the separation length is $0.20c$. From $t/T=0.125$ to 0.50 separation start point gradually moves upstream (from $0.77c$ to $0.62c$) and separation length gradually increases from $0.229c$ to $0.36c$. At $t/T=0.625$, 0.75 no separation is observed. At $t/T=0.875$ separation is found at $0.996c$ with very minute separation length ($0.0037c$). On the mid-airfoil lower surface, from $t/T=0$ to 0.125 separation point moves downstream (from $0.59c$ to $0.82c$) and corresponding separation length gradually decreases from $0.40c$ to $0.15c$. In the next time step at $t/T=0.25$ no separation is observed. From $t/T=0.375$ to 1.0 separation point moves upstream from $0.90c$ to $0.59c$ and separation length increase here from $0.1c$ to $0.40c$. On the upper airfoil lower surface from $t/T=0$ to 0.50 separation point moves upstream (from $0.744c$ to $0.62c$) and then from $t/T=0.5$ to 0.625 it goes downstream and in the next time steps separation point gradually moves upstream. From $t/T=0$ to 0.5 separation length is also comparatively higher. On the lower airfoil upper surface, from $t/T=0$ to 0.125 separation point moves downstream (from $0.59c$ to $0.79c$) then it gradually moves upstream in the next time steps. Separation length also decreased initially after $t/T=0.25$ separation length gradually increases to $0.80c$.

The separation point and separation length for stagger angle $\theta=10^\circ$ have been represent by figure. 4.61(e), (f) respectively. On the mid-airfoil upper surface, at $t/T=0$ separation starts at $0.96c$ and the separation length is $0.036c$. From $t/T=0.125$ to 0.5 separation point moves upstream (from $x_{sep}/c=0.807$ to 0.66) and the separation length also gradually increases from $0.19c$ to $0.322c$. In the next time instant, at $t/T=0.625$ separation starts at $0.95c$ and the corresponding separation length is $0.01c$. At $t/T=0.75$ separation starts at $0.90c$ and the separation length $0.07c$. At $t/T=0.875$ no separation is observed in this surface. Similarly, on the mid-airfoil lower surface, at time step $t/T=0$, 0.125 separation starts at $0.6c$, $0.572c$ and separation length is $0.37c$, $0.397c$. At $t/T=0.25$ no separation is observed. At $t/T=0.375$ separation point is located at $0.815c$ and the separation length is $0.114c$. From $t/T=0.50$ to 1.0 separation point moves upstream (from $0.85c$ to $0.60c$) and the separation length gradually increases from $0.15c$ to $0.37c$. On the upper airfoil lower surface, from $t/T=0$ to 0.5 separation point moves upstream (from $x_{sep}/c=0.76$ to 0.66) with the increase in separation length from $0.67c$ to $1.11c$. From $t/T=0.625$ to 0.875 it is observed that separation point moves upstream from $0.82c$ to $0.80c$ and for all of these cases separation length is comparatively higher ($L_{sep}/c=1.06c$, $1.2c$, $1.08c$). On the lower airfoil upper surface, from $t/T=0$ to 0.125 separation point moves upstream from $0.6c$ to $0.566c$ and the separation length increase from $0.718c$ to $0.726c$. At $t/T=0.25$ separation starts at $0.75c$ with a separation length of $0.42c$. From $t/T=0.375$ to 1.0 as separation point moves upstream ($x_{sep}/c=0.73$ to 0.60) separation length gradually increases from $0.18c$ to $0.718c$.

Figure. 4.61 (g), (h) shows the separation point and separation length respectively for $\theta=15^\circ$. On the mid-airfoil upper surface, from $t/T=0$ to 0.375 separation point moves upstream and separation

length gradually increases. At $t/T=0.5$ separation starts at $0.90c$ and separation length is $0.09c$. At $t/T=0.625$ separation starts at $0.90c$ with very small separation length ($L_{sep}/c=0.06$). At $t/T=0.75$, 0.875 no separation is noticed. On the mid-airfoil lower surface, from $t/T=0$ to 0.25 separation point moves upstream and separation length gradually increases. At $t/T=0.375$ no separation is observed. Separation again starts at $0.845c$ at $t/T=0.5$ with separation length of $0.15c$ and at next time steps separation point again moves upstream with an increase in separation length. On the upper airfoil lower surface, separation point gradually move upstream from $0.756c$ to $0.68c$ ($t/T=0$ to 0.5) and separation length is comparatively higher. At $t/T=0.625$ separation starts at $0.844c$ and separation length is $1.23c$. After that separation point comes upstream. On the lower airfoil upper surface separation length initially decreases with time, again increases. On the upper airfoil lower surface the separation length is higher than the lower airfoil upper surface.

The separation point and separation length for stagger angle $\theta=20^\circ$ have been shown by figure 4.61(i), (j) respectively. On mid-airfoil upper surface separation starts at $t/T=0$ at $0.808c$ and separation length is $0.19c$. From $t/T=0.125$ to 0.375 separation point moves upstream and the corresponding separation length increases. At $t/T=0.5$ separation starts at $0.90c$ and the separation length is $0.09c$. At $t/T=0.625$ small separation is noticed at $0.917c$. In the next two time step no separation is observed. Similarly, on the mid-airfoil lower surface from $t/T=0$ to 0.125 separation point moves upstream. At $t/T=0.25$ there is no separation. From $t/T=0.375$ to 1 separation point moves upstream (from $0.81c$ to $0.55c$) with the separation length increases from $0.15c$ to $0.43c$. On the upper airfoil lower surface and lower airfoil upper surface similar behaviors are observed. But in case of upper airfoil lower surface separation length is comparatively larger.

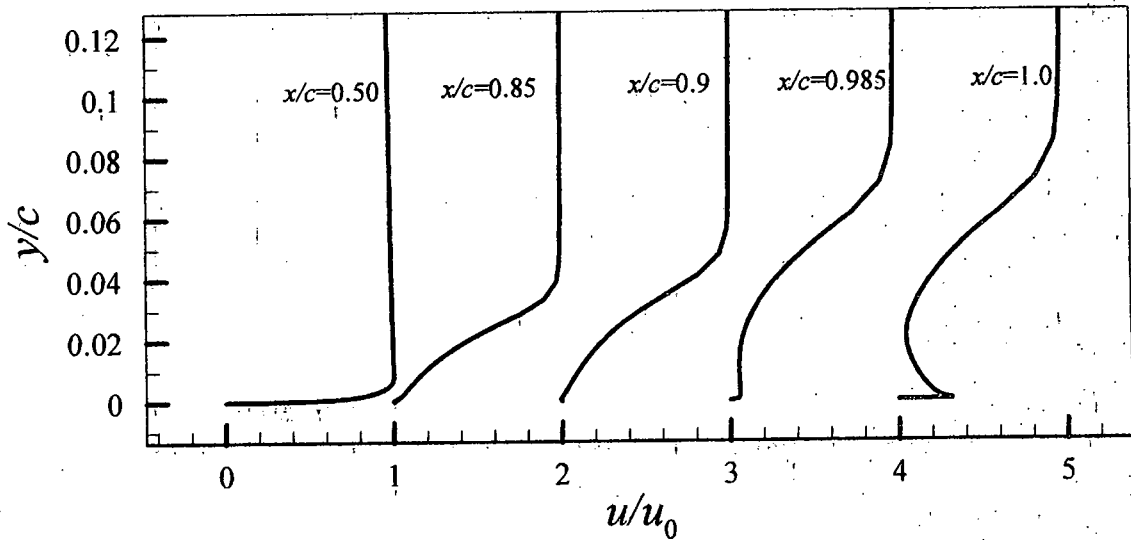


Figure 4.57 Velocity profile at different locations near the mid-airfoil upper surface ($\theta=0^\circ$, $t/T=0$)

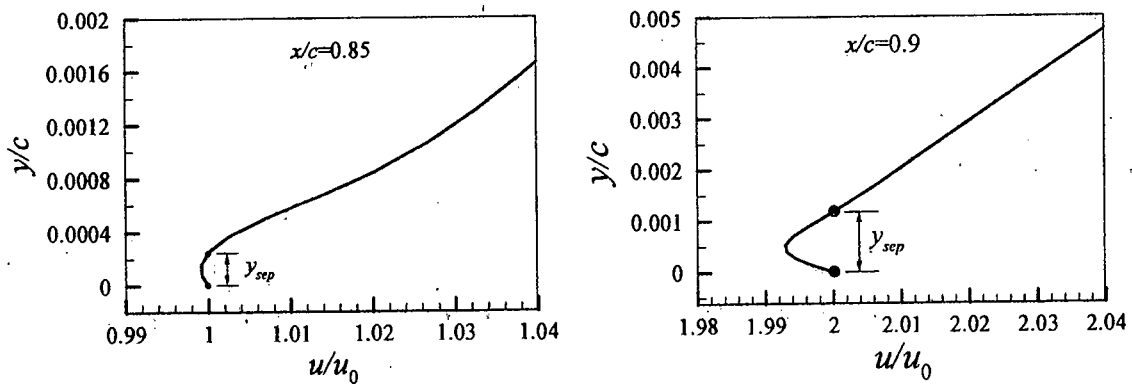


Figure 4.58 Enlarged view of the velocity profile near the mid-airfoil upper surface ($\theta=0^\circ$, $t/T=0$)

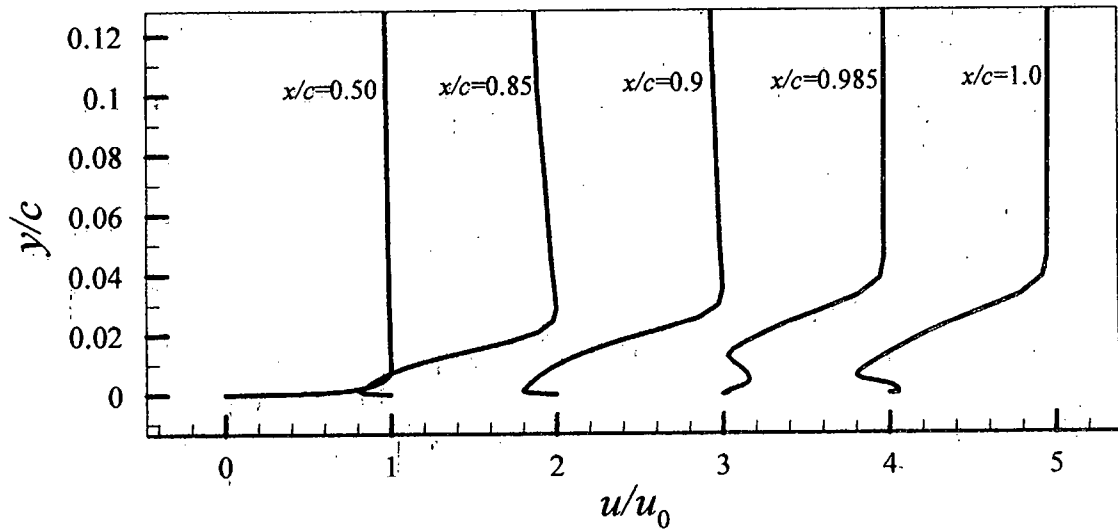


Figure 4.59 Velocity profile at different locations near the mid-airfoil lower wall ($\theta=0^\circ$, $t/T=0$)

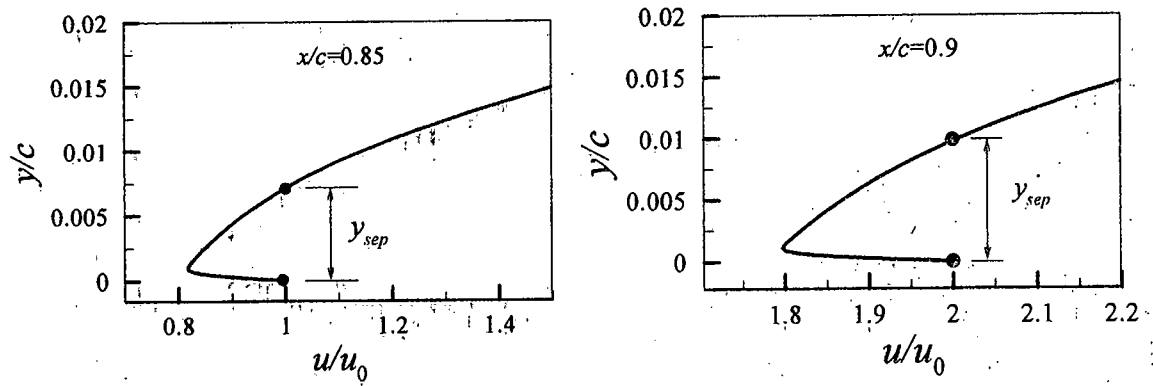


Figure 4.60 Enlarged view of the velocity profile near the mid-airfoil lower wall ($\theta=0^\circ$, $t/T=0$)

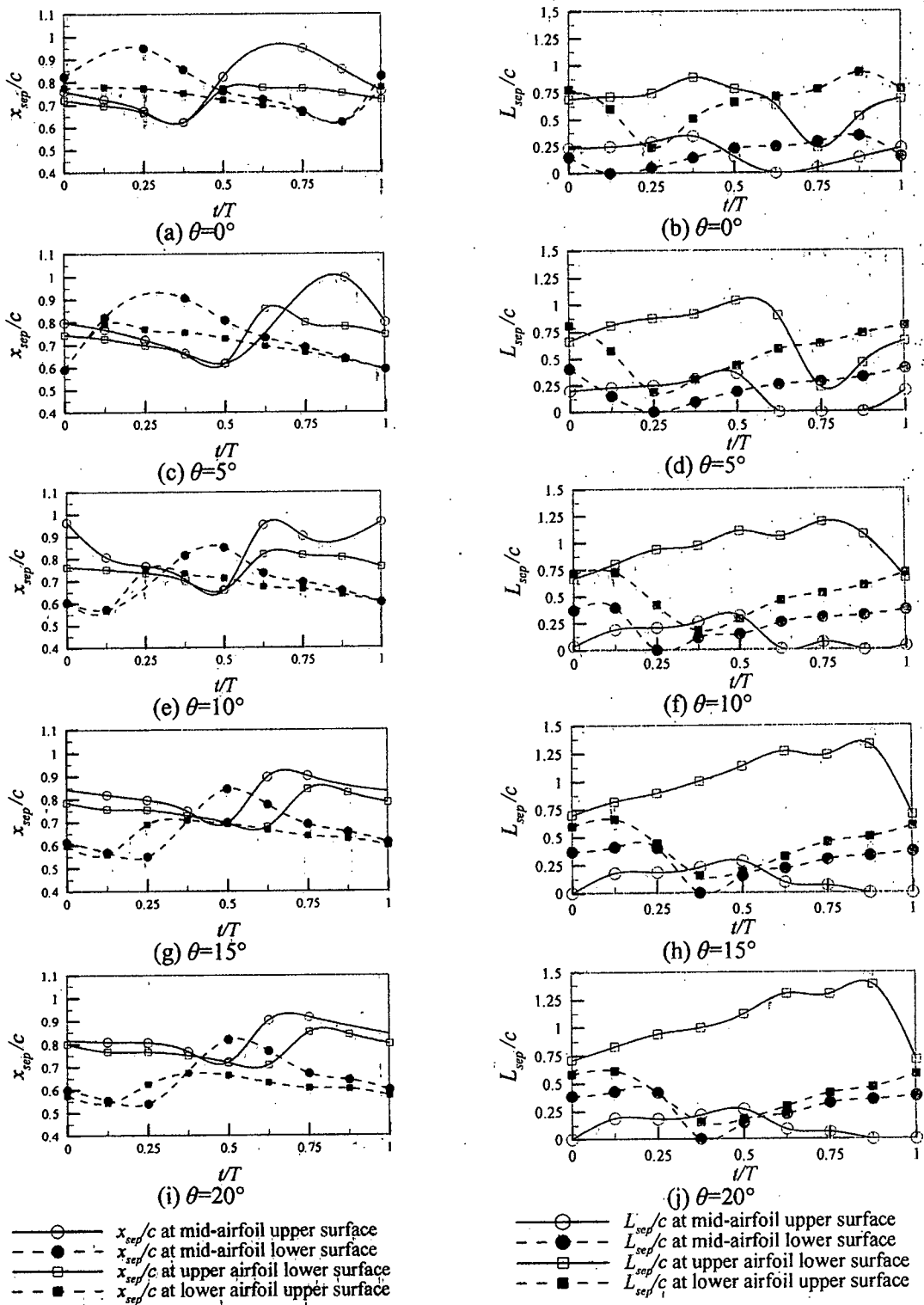


Figure. 4.61 Separation point and separation length for different stagger angle in a cycle

4.10 DRAG CHARACTERISTICS

A drag force is the resistance force caused by the motion of a body through a fluid, such as water or air. A drag force acts opposite to the direction of the oncoming flow velocity. This is the relative velocity between the body and the fluid. Drag characteristics are expressed in terms of drag coefficient c_d .

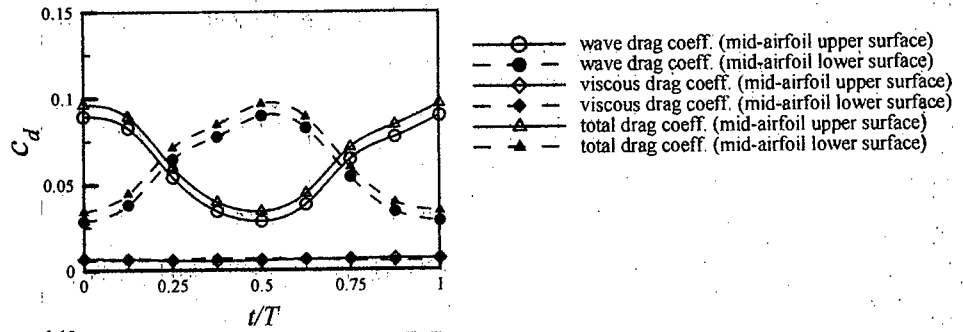
$$c_d = \frac{F_D}{\frac{1}{2} A \rho_\infty v_\infty^2} \quad (4.4)$$

Where, the drag force exerted on a body traveling through a fluid is given by F_D , ρ_∞ is the free stream density and v_∞ is the free stream velocity. A is the projected cross-sectional area of the body perpendicular to the flow direction.

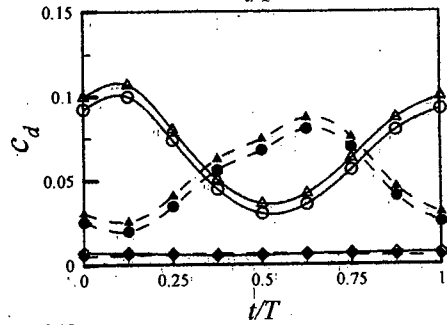
In transonic flow drag can increase via two mechanisms—the shock wave introduces a stagnation pressure drop that leads to wave drag, and the presence of separation causes additional viscous drag. The presence of shock waves on a transonic airfoil causes reductions of total pressure that are directly linked to the generation of drag. The contribution of the overall drag due to the shock is referred to generally as wave drag. Wave drag represents a substantial proportion of the total drag in high Mach number flows. The magnitude of wave drag can be estimated by integrating the stagnation pressure losses across the shock. These losses are not uniform along the shock because the upstream Mach number (and shock strength) reduces with distance from the surface. Typically, the greatest losses are observed close to the airfoil surface. A contribution to the wake-pressure profile of a transonic airfoil is from viscous drag due to the presence of flow separation. However, any stagnation pressure loss in an adiabatic flow is related to an entropy rise. Here, the entropy increase is achieved across the shock wave is by viscous actions on a microscopic scale.

Figure 4.62 shows the drag characteristics on mid-airfoil upper and lower surface for stagger angle, (θ) varying from 0° to 20° . In figure 4.62(a) solid line with white circle denotes the wave drag coefficient, solid line with white diamond is for viscous drag coefficient and solid line with white triangle stands for total drag coefficient on mid-airfoil upper surface. The plot shows the behavior in a cycle. We have already seen that on mid-airfoil upper surface strong shock wave is formed at $t/T=0$ and $x/c=0.73$. So, solid line with white circle has its peak value at $t/T=0$ which implies that at higher Mach number, wave drag plays the significant role than the viscous drag. Here, total drag is the sum of wave drag and viscous drag. After $t/T=0$ shock moves toward leading edge with lower strength and the curves shows a decreasing trend. At $t/T=0.5$, shock occurs at $x/c=0.56$ with lower strength and the total drag coefficient also shows a lower value here. On mid-airfoil lower surface pressure fluctuation is maximum at $x/c=0.73$ at $t/T=0.5$ and hence the total drag force is also maximum at this time step in which wave drag has the significant contribution. As the time goes on and we move to the next time steps we see a decrease in total drag force as the shock wave gradually gets weaker as it moves upstream in the corresponding time steps. With the increase in stagger angle from 5° to 20° it is observed that on mid-airfoil upper surface wave drag as well as the total drag increases and on the lower surface the corresponding value decreases.

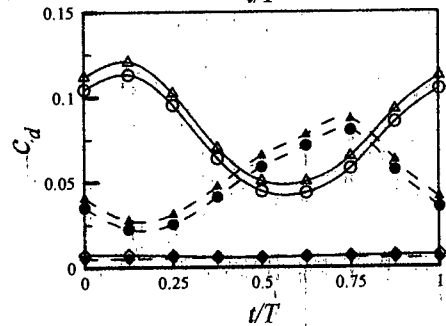
(a) $\theta=0^\circ$



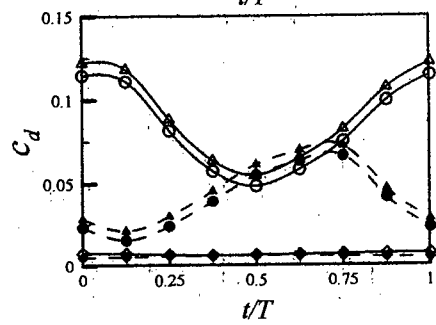
(b) $\theta=5^\circ$



(c) $\theta=10^\circ$



(d) $\theta=15^\circ$



(e) $\theta=20^\circ$

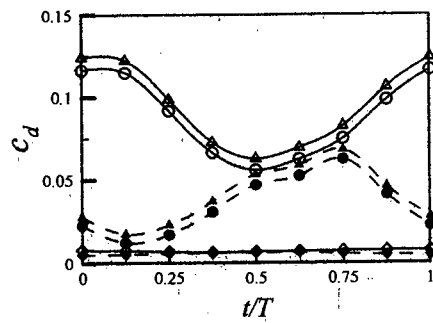


Figure 4.62 Drag characteristics on mid-airfoil upper and lower surface for stagger angle
(a) $\theta=0^\circ$ (b) $\theta=5^\circ$ (c) $\theta=10^\circ$ (d) $\theta=15^\circ$ (e) $\theta=20^\circ$

CHAPTER 5

EXPERIMENTAL STUDY

5.1 SUPERSONIC WIND TUNNEL FACILITY

Together with the numerical simulation, experiments were conducted using a supersonic open circuit wind tunnel. Maximum achievable Mach number of the wind tunnel is 1.8 with cross section 1 inch×4 inch. In the wind tunnel, air is drawn in from the laboratory environment, passes through the test section and is returned back to the lab through the tunnel exhaust. A high capacity blower has been used for this purpose. Self-excited shock oscillation around a biconvex circular arc airfoil cascade in transonic internal flow is conducted with this facility. Cascade consists of three circular arc airfoil which are placed in the test section of the wind tunnel. In the test section the airfoil cascade was placed at three different angle of attack, 0°, 5° and 10°. In all these three cases stagger angle was kept at 0°. In numerical case, investigation was carried out for 5 different stagger angles and in experimental case study was limited to 0° stagger angle and three different approach angles. Figure. 5.1(a), (b) shows the supersonic wind tunnel with Schlieren experimental setup.

(a)



test section

air inlet

rotary encoder

mirror

light source

Power supply

(b)



air exhaust

blower

Pressure taps

Figure. 5.1 Supersonic wind tunnel with Schlieren experimental setup

5.2 FLOWFIELD AROUND CASCADE

To investigate the behavior of the passage shock wave in a two-dimensional transonic cascade, experimental study has been performed for an unstaggered case with different approach angle. The fluctuating shock wave positions in the stream-wise direction in the blade passages are observed by the Schlieren apparatus. The occurrence of the phenomenon of the self-excited shock wave oscillation is confirmed clearly in the unstaggered case.

Flow fields around the cascade exhibiting the oscillation of shock waves are visualized by the Schlieren system and recorded by a Digital Single-lens reflex (SLR) camera with a continuous light. Figure. 5.2-5.4 shows the examples of the Schlieren photographs of transonic flow around the unstaggered cascades. The normal shock waves are clearly observed in the cascade passages. The normal shocks are interacting with the boundary layers and the flow separations are observed in these photographs. In the unstaggered case, the upper passage shock wave position is in different location from the lower one. The observations by the Digital Single-lens reflex (SLR) camera show that the shock fluctuation is occurred in a range of back pressures and the upper and lower passage shock waves move in almost anti-phase to each other. In the Schlieren image for each case more than one image were captured to observe the shock wave oscillation at different time instant.

With the decrease in pressure ratio (PR), the shock wave moves downstream. At different back pressure, shock waves are developed asymmetrically between upper and lower surfaces. These asymmetric shock waves indicate the alternate shock oscillation around airfoil surfaces. The shock behaviors of upper and lower passages are almost the same. The general trend is observed only for unstaggered case and staggered case was not experimented due to the unavailability of staggered cascade model. However, a slight difference between numerical shock structure and experimental one is observable, which is obviously created due to the complexities in real flows, the main flow non-uniformity and the sidewall boundary layers, which are never taken into account in usual 2D numerical simulations. Figure. 4.5 shows computer generated Mach contour images corresponding to figure 5.2 for approach angle 0° and stagger angle 0° . The flow structures are similar to the experimental results. Furthermore, shock wave movement extends towards downstream of trailing edge at lower pressure ratio.

For stagger angle 0° and approach angle 0° , normal shock wave is observed in the air foil cascade passage. From instantaneous Schlieren image with pressure ratio (PR) 0.80, the shock is observed in figure. 5.2(1) with maximum Mach number ahead of the shock is $M=1.22$. In the mid-airfoil upper surface shock is located at $0.79c$ and on the mid-airfoil lower surface shock is located at $0.83c$. As the pressure ratio decreases to 0.72, λ -shock is observed downstream of the trailing edge. Here, maximum Mach number ahead of the shock is 1.3. With the increase of approach angle from 0° to 5°

as shown in the figure. 5.3. At a pressure ratio of 0.8 the maximum Mach number ahead of the shock is 1.22.

It can be clearly observed that shock wave on the mid-airfoil upper surface and mid-airfoil lower surface occur at different locations. On the mid-airfoil upper surface normal shock wave occurs at $0.75c$ and on the mid-airfoil lower surface normal shock wave occurs at $0.82c$ i.e., on the mid-airfoil upper surface shock occurs nearer to leading edge than the shock on the mid-airfoil lower surface. As the pressure ratio is decreased to 0.72 then λ -shock is observed on the mid-airfoil upper surface and mid-airfoil lower surface and the shock is located at around the trailing edge.

At approach angle 10° with pressure ratio 0.69, shock waves both on mid-airfoil upper surface and mid-airfoil lower surface moves down stream as shown in figure. 5.4(1). Similar to approach angle 5° , in this case also shock on the mid-airfoil upper surface is nearer to leading edge than the shock on the mid-airfoil lower surface. The instantaneous shock waves are located at $0.88c$ on the mid-airfoil upper surface and $0.96c$ on mid-airfoil lower surface. It can be said that shock wave gets weaker and both shock waves on the mid-airfoil upper and mid-airfoil lower surfaces are λ -shock. Maximum Mach number ahead of the shock wave is 1.3. For approach angle 0° and pressure ratio 0.64 the shock wave moves downstream i.e., outside the trailing edge and becomes very weaker as shown in figure. 5.4(2).

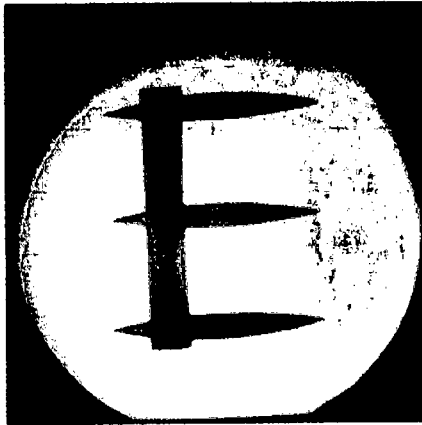
In case of approach angle 0° with pressure ratio 0.72, approach angle 5° with pressure ratio 0.72 and approach angle 10° with pressure ratio 0.69 the shock structure transforms from normal to λ -shock structure. As the λ -shock wave has a larger foot than that of normal shock wave its interaction with boundary layer is much weaker. So, finally it can be stated that with the increase of approach angle and decrease in pressure ratio shock wave becomes weaker.

5.3 SCHLIEREN IMAGE (EXPERIMENTAL)

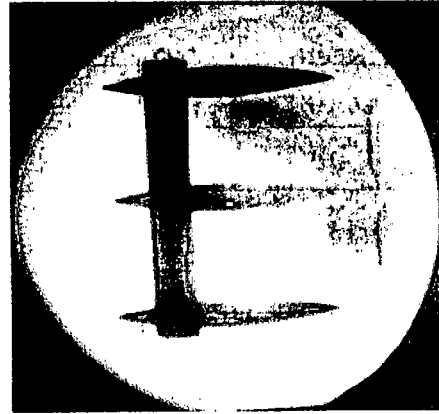
α = Approach angle

1) $\alpha = 0^\circ$ with pressure ratio=0.80 ($M=1.22$)

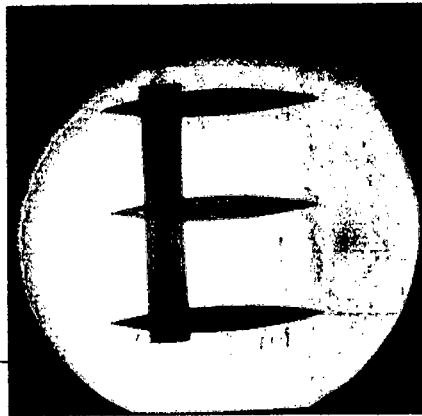
2) $\alpha = 0^\circ$ with pressure ratio=0.72 ($M=1.3$)



(a)



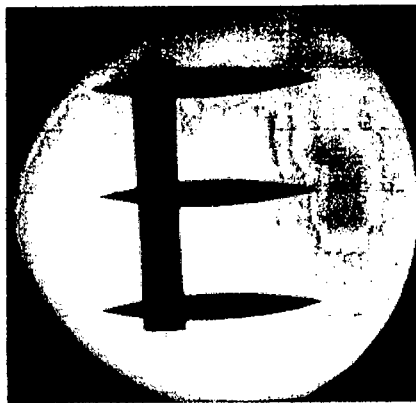
(a)



(b)



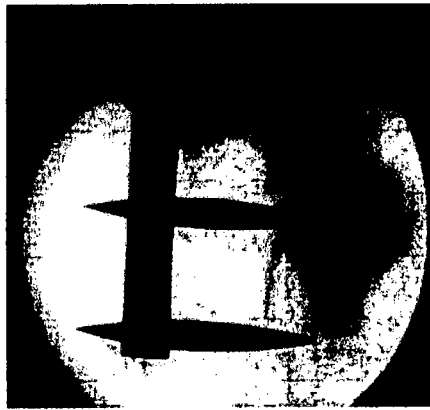
(b)



(c)

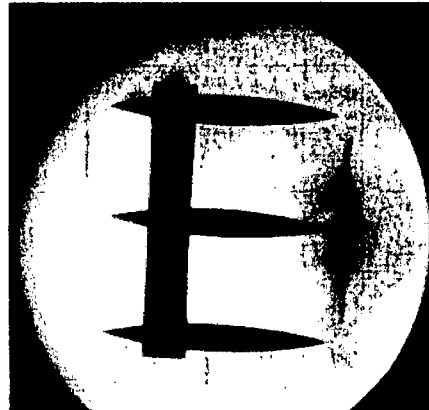
Figure. 5.2 Instantaneous Schlieren image of airfoil cascade with stagger angle 0° , approach angle 0° with pressure ratio 0.80 and 0.72 respectively

3) $\alpha = 5^\circ$ with pressure ratio=0.80 ($M=1.22$)

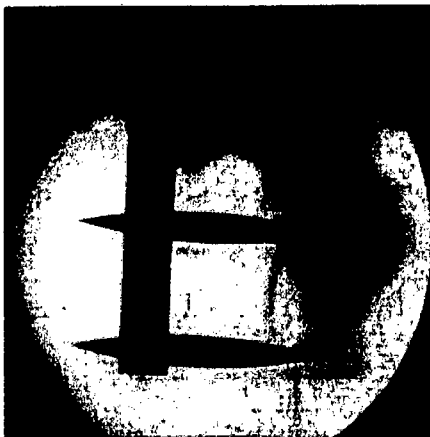


(a)

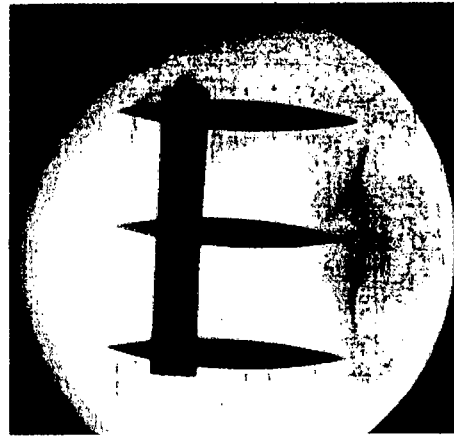
4) $\alpha = 5^\circ$ with pressure ratio=0.72 ($M=1.3$)



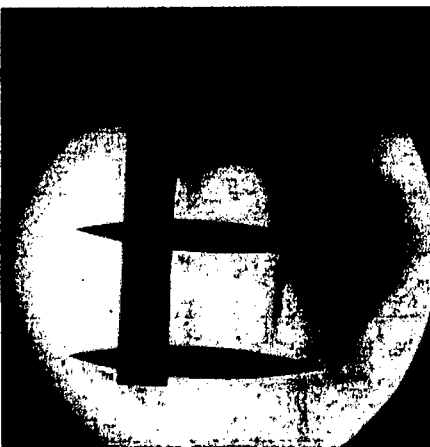
(a)



(b)



(b)



(c)

Figure. 5.3 Instantaneous Schlieren image of airfoil cascade with stagger angle 0° , approach angle 5° with pressure ratio 0.80 and 0.72 respectively

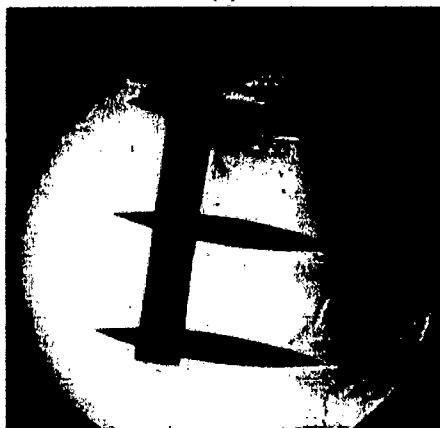
5) $\alpha = 10^\circ$ with pressure ratio=0.69 ($M=1.3$)



(a)

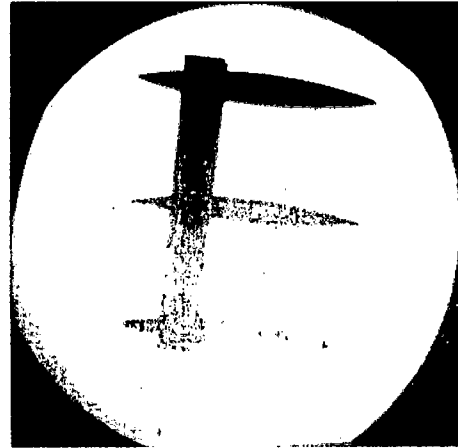


(b)

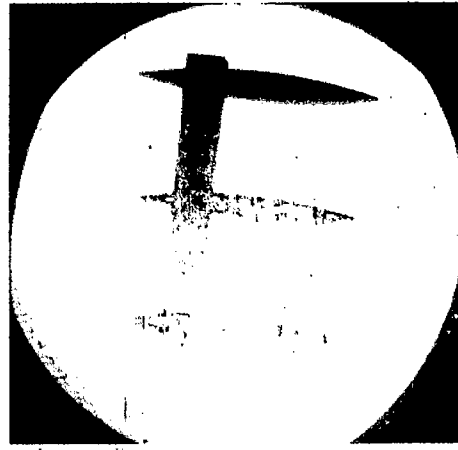


(c)

6) $\alpha = 10^\circ$ with pressure ratio=0.64 ($M=1.63$)



(a)



(b)

Figure. 5.4 Instantaneous Schlieren image of airfoil cascade with stagger angle 0° , approach angle 10° with pressure ratio 0.69 and 0.64 respectively

CHAPTER 6

SUMMARY AND RECOMMENDATION

6.1 SUMMARY OF THE STUDY

A computational study using Reynolds Averaged Navier-Stokes (RANS) equations has been performed to investigate the internal flow characteristics of a biconvex circular arc airfoil cascade. Angle of attack is kept at 0° . Stagger angle is varied from 0° to 20° . The findings of the present study can be summarized as follows:

- i. Simulation of the flow reveals unsteadiness in the flow field. Fluctuating pressure histories are recorded at different locations in the flow field. Self-excited shock wave oscillation is observed for all cases ($\theta=0^\circ$ to 20°).
- ii. The flow field clearly reveals the presence of normal shock wave over the airfoil surfaces and their oscillation with time. The shock oscillation is Type-B (interrupted shock wave motion).
- iii. Positions of the shock waves follow the periodic behavior corresponding to unsteady shock oscillation. With the increase in stagger angle, on the mid-airfoil upper surface shock wave start and end points move down stream and on the mid-airfoil lower surface shock wave start and end points move upstream.
- iv. PSD from FFT calculation of the data is used to find the principal frequency of the unsteady behaviour. A frequency of 976 Hz is found to be the dominating frequency at different positions.
- v. On the mid-airfoil upper surface upto 5° stagger angle shock oscillation region increases then with further increase in stagger angle shock oscillation region decreases. On the mid-airfoil lower surface upto 10° stagger angle shock oscillation region increases then with the increase in stagger angle shock oscillation region decreases.
- vi. It is observed that for all the cases, the flow field remains undisturbed from leading edge to $x/c=0.50$, as in that portion no shock wave is observed on the airfoil surfaces. At 0° stagger angle peak RMS of pressure oscillation (p_{rms}/q_0) is at the same location on the mid-airfoil upper and mid-airfoil lower surface. With the increase in stagger angle from 0° to 20° , on the mid-airfoil upper surface p_{rms}/q_0 first increases from 0.667 to 0.69 and then decreases to 0.586 and the location is shifted from $x/c=0.71$ to 0.75 (towards downstream). Similarly, on the mid-airfoil lower surface p_{rms}/q_0 first increases from 0.68 to 0.688 and then decreases to 0.652 and the location is shifted towards upstream (from $x/c=0.71$ to $=0.625$).

- vii. Flow separation occurs at a distance after the shock wave. Separation is observed in both x and y -direction. At $\theta=0^\circ$, maximum separation length in x -direction is same $0.35c$ on the mid-airfoil upper and mid-airfoil lower surface. With the increase in stagger angle from 0° to 20° , on the mid-airfoil upper surface maximum separation length in x -direction decrease from $0.35c$ to $0.268c$, on the mid-airfoil lower surface the corresponding value increases from $0.35c$ to $0.43c$.
- viii. Wave drags contribution is much higher than viscous drag at high speed compressible flow. In each case wave drag is higher than viscous drag. At stagger angle 0° wave drag is same in both mid-airfoil upper and mid-airfoil lower surface. With the increase in stagger angle it is observed that on mid-airfoil upper surface wave drag as well as the total drag increases and on the mid-airfoil lower surface the corresponding values decreases.
- ix. From experimental observation it can be stated that shock wave occurs both on the mid-airfoil upper and mid-airfoil lower surface. With the increase in approach angle from 0 to 10 and decrease in pressure ratio from 0.8 to 0.64 shock wave becomes weaker as the normal shock transforms into λ -shock.

6.2 RECOMMENDATION

The following recommendations can be made for future work:

- i. In our study a cascade with three biconvex circular arc airfoil have been used. Also, for simplicity upper airfoil upper surface and lower airfoil lower surface are omitted. Study could be carried out with more number of blades and for 3D case.
- ii. In this study stagger angle is varied from 0° to 20° . It can be studied what changes occur in flow field if stagger angle is increased further. Combined effect of stagger angle, blade spacing and angle of attack can also be studied.
- iii. The study could involve calculations of displacement thickness, shape factor, momentum thickness, energy loss thickness, total pressure loss coefficient.
- iv. Different methods for passive control can be studied to find their effect on Shock Wave Turbulent Boundary Layer Interaction (SWTBLI).
- v. In experimental case, shock wave is observed from instantaneous Schlieren images and shock locations were measured manually. A line scanning camera and data acquisition system can be used to exactly locate shock positions and to observe its variations throughout the cycle. Also, shock wave oscillation frequency can be measured to compare the experimental case with numerical results.

REFERENCES

- [1] McDevitt, J.B., Levy, L.L., and Deiwert, G. S., "Transonic Flow about a Thick Circular-arc Airfoil", *AIAA Journal*, 14(5), 603-613, 1976.
- [2] Tijdeman, H., "Investigations of the Transonic Flow Around Oscillating Airfoils", *National Aerospace Laboratory*, 1977.
- [3] Levy, L. L., "Experimental and Computational Steady and Unsteady Transonic Flows about a Thick Airfoil", *AIAA Journal*, 16(6), 564-572, 1978.
- [4] Tijdeman, H., Seebass, R., "Transonic Flow Past Oscillating Airfoils", *Annual Review of Fluid Mechanics Journal*, 12(1), 181-222, 1980.
- [5] Gronland, T.A., Eliasson. P., Nordstrom, J., "Accuracy of Unsteady Transonic Flow Computations", *International Council of the Aeronautical Sciences*, 21st congress, ICAS-98-4.2, 1998.
- [6] McDevitt, J.B., "Supercritical Flow about a Thick Circular-arc Airfoil", *National Aeronautics and Space Administration Technical Memorandum*, 6-88, January, 1979.
- [7] Li, Y.C., Wang, J.J., Hua, J., "Experimental Investigations on the Effects of the Divergent Trailing Edge and Gurney Flaps on a Supercritical Airfoil", *Aerospace Science and Technology* 11, 91-99, 2007.
- [8] Alfano, D., Michel, B., Corre, C., Lerat, A., "Numerical Simulation of Shock / Boundary - layer Self-sustained Oscillations for External and Internal Flows", *AIAA Paper, 24th Applied Aerodynamics Conference*, 2006-2840, 2006.
- [9] Raghunathan, S., Early, J.M., Tulita, C., Bernard, E., Quest, J., "Periodic Transonic Flow and Control", *The Aeronautical Journal*, January, 2008.
- [10] Chen, Li-Wei., Xu, Chang-Yue., Lu, Xi-Yun., "Numerical Investigation of the Compressible Flow Past an Airfoil", *J. Fluid Mech.*, 643, 97-126, 2010.
- [11] Catalano, P., Tognaccini, R., "RANS Analysis of the Low-Reynolds Number Flow around the SD7003 Airfoil", *Aerospace Science and Technology*, 15(8), 615-626, December, 2011.
- [12] Hasan, A.B.M. Toufique., Matsau, S., Setoguchi, T., Islam, A.K.M. Sadrul, "Effects of Condensing Moist Air on Shock Induced Oscillation around an Airfoil in Transonic Internal Flows", *International Journal of Mechanical Sciences*, 1-11, 2011.
- [13] Xiong, J., Nezhad, S.T., Liu, F., "Computation of Self-excited Unsteady Transonic Flow of an airfoil in a channel using URANS and DES", *AIAA paper*, 2010-5109, 2010.
- [14] Bendiksen, O.O., "Review of Unsteady Transonic Aerodynamics: Theory and Application", *Progress in Aerospace Sciences*, 47, 135-167, 2011.
- [15] Yagiz, B., Kandil, O., Pehlivanoglu Y. V., "Drag minimization using active and passive flow control techniques", *Aerospace Science and Technology*, 17(1), 21-31, 2012.

- [16] Eleni, D. C., Athanasios, T. I., Dionissios, M.P., "Evaluation of the Turbulence Models for the Simulation of the Flow over a National Advisory Committee for Aeronautics (NACA) 0012 Airfoil", *Journal of Mechanical Engineering Research*, 4(3), 100-111, March, 2012.
- [17] Lee, B.H.K., "Self-sustained shock oscillations on airfoils at transonic speeds", *Progress in Aerospace Sciences*, 37(1), 147-196, 2001.
- [18] Alshabu, A., Olivier, H., "Unsteady wave phenomena on a supercritical airfoil", *AIAA Journal*, 46, 2066-2073, 2008.
- [19] Zhao, Z., Ren, X., Gao, C., Xiong, J., Liu, F., Luo, S., "Experimental Study of Shock Wave Oscillation on SC(2)-0714 Airfoil", in *51st AIAA Aerospace Sciences Meeting*, Texas, AIAA 2013-0537, 2013.
- [20] Sartor, F., Mettor, C., Sipp, D., "Stability, Receptivity, and Sensitivity Analyses of Buffeting Transonic Flow over a Profile", *AIAA Journal*, 53, 1980-1993, 2015.
- [21] Qin, N., Zhu, Y., Shaw, S.T., "Numerical study of active shock control for transonic aerodynamics", *International Journal of Numerical Methods for Heat and Fluid Flow*, 14(4), 444-466, 2004.
- [22] Stanewsky, E., "Adaptive Wing and Flow control Technology", *Progress in Aerospace Sciences*, 37(7), 583-667. 2001.
Li, J., Lee, C. H., Jia, L., Li, X., "Numerical Study on Flow Control by Micro-Blowing", *47th AIAA Aerospace Sciences Meeting*, Orlando, Florida, AIAA 2009-779, 2009.
- [23] Hasan, A. B. M. T., Matsuo, S., Setoguchi, T., Kim, H.D., Yu, S., "Control of transonic flow with non-equilibrium condensation around a circular arc blade using bump", *International Journal of Turbo and Jet Engines*, 26(1), 3-49, 2009.
- [24] Raghunathan, S., Early, J.M., Tulita, C., Benard, E., Quest, J., "Periodic transonic flow and control", *Aeronautical Journal*, 112, 1-16, 2008.
- [25] Ashill, P.R., Fulker, J.L., Shires, A., "A novel technique for controlling shock strength of laminar-flow aerofoil sections", *First European Forum on Laminar Flow Technology*, Hamburg, Germany, 1992.
- [26] Patzold, M., Lutz, Th., Kramer, E., Wagner, S., "Numerical optimization of finite shock control bumps", *44th Aerospace Science Meeting and Exhibit*, Reno, Nevada, AIAA Paper-1054, 2006.
- [27] Tian, Y., Liu, P., Feng, P., "Shock control bump parametric research on supercritical airfoil", *Science China Technological Sciences*, 54(11), 2935-2944, 2011.
- [28] Mazaheri, K., Kiani, K.C., Nejati, A., Zeinalpour, M., Taheri, R., "Optimization and analysis of shock wave/boundary layer interaction for drag reduction by Shock Control Bump", *Aerospace Science and Technology*, 42, 196-208, 2015.
- [29]

- [30] Hasan, A.B.M.T., Alam, M., "A numerical study on the control of self-excited shock induced oscillation in transonic flow around a supercritical airfoil", *International Journal of Fluid Mechanics Research*, 41(5), 440-459, 2014.
- [31] McComick, D.C., "Shock/Boundary-Layer Interaction control with Vortex Generators and Passive Cavity", *ALAA Journal*, 31(1), 91-96, 1993.
- [32] Smith, A.N., Babinsky, H., Dhanasekaran, P.C., Mark, S., Bill, D., "Computational Investigation of Groove Controlled Shock Wave / Boundary Layer Interaction", *41st Aerospace Sciences Meeting and Exhibit*, Reno, Nevada, 0446, 2003.
- [33] Rowley, D.C., Williams, "Dynamics and control of high-Reynolds-number flow over open Cavities", *Annual Review of Fluid Mechanics*, 38, 251-276, 2006.
- [34] Olsman, W.F.J., Colonius, T., "Numerical simulation of flow over an airfoil with a cavity", *AIAA Journal*, vol. 49(1), 143-149, 2011.
- [35] Rahman, M.M., Hasan, A.B.M.T., Islam, A.K.M.S., Matsuo, S., Setoguchi, T., "Computation of transonic internal flow around a biconvex airfoil with cavity", *Journal of Mechanical Science and Technology*, 29(6), 2415-2421, 2015.
- [36] Yu, T., Wang, J.J., Zhang, P.F., "Numerical Simulation of Garney Flap on RAE-2822 Supercritical Airfoil", *Journal of Aircraft*, 48(5), 1565-1575, 2011.
- [37] Hartmann, A., Klass, M., Schroder, W., "On the interaction of shock waves and sound waves in transonic buffet flow", *Physics of Fluids*, 25, 026101, 2013.
- [38] Bahi, L., Ross, J.M., Nagamatsu, H.T., "Passive shock wave/boundary layer control for transonic airfoil drag reduction", *AIAA Paper*, 83-0137, 1983.
- [39] Nagamatsu, H.T., Orozco, R.D., Ling, D.C., "Porosity effect on supercritical airfoil drag reduction by shock wave/boundary layer control", *AIAA Paper*, 84-1682, 1984.
- [40] Raghunathan, S., "Passive control of shock-boundary layer interaction", *Progress in Aerospace Sciences*, 25, 271-296, 1989.
- [41] Doerffer, P., Szulc, O., "Passive control of shock wave applied to helicopter rotor high-speed impulsive noise reduction", *Polish Academy of Science, Fizyca* 14, 80-952, 2010.
- [42] Yamamoto, K., Tanida, Y., "Self excited oscillation of transonic flow around an airfoil in two dimensional channels", *ASME Journal of Turbomachinery*, 112, 723-731, 1990.
- [43] Xiong, J., Nezhad, S.T., Liu, F., "Computation of Self-excited Unsteady Transonic Flow of an airfoil in a channel using URANS and DES", *AIAA Paper*, 2010-5109, 2010.
- [44] Hamid, M.A., Hasan, A.B.M.T., Alimuzzaman, S.M., Matsuo, S., Setoguchi, T., "Compressible flow characteristics around a biconvex arc airfoil in a channel", *Propulsion and Power Research*, 3(1), 29-40, 2014.
- [45] Schreiber, H.A., Starken, H., "An investigation of a strong shock-wave turbulent boundary layer interaction in a supersonic compressor cascade". *ASME paper*, 1-11, 1991.

- [46] Kusters, B., Schreiber, H.A., "Compressor Cascade Flow With Strong Shock-Wave/Boundary-Layer Interaction". *AIAA Journal*, 36(11), 2072-2078, 1998.
- [47] Shiratori, T., Matsuhita, M., Noguchi, Y., "Periodic fluctuation of shock waves in Transonic cascade flows". *Unsteady Aerodynamics and Aeroelasticity of Turbomachines*, 693-704, 1998.
- [48] Menter, F.R., "Two-equation eddy-viscosity models for engineering applications". *AIAA Journal*, 32(8), 1598-1605, 1994.

